Wageningen University

MSc Thesis Report

Applicability of the Maximum Power Limit for Estimating Land-Atmosphere Interactions on the Diurnal Time Scales

Author: **Aljoša Slameršak**
WUR number: **900829766200**
Study Program: **MSc Climate Studies**

Supervisors: **Prof. Dr. Laurens Ganzeveld**
Dr. Axel Kleidon

Chair Group: **Earth System Science**
Wageningen University

Jena, 27th of April 2015

Abstract

Surface turbulent heat fluxes are the driving force of the land-atmosphere exchange in the system that is in a state of a sustained thermodynamic disequilibrium. We propose an alternative modelling approach by assuming that the atmosphere performs as a thermodynamic heat engine which is operating at its theoretical maximum power generation limit with respect to the convective transport in the system. This assumption provides us with an additional physical constraint that makes it possible to model the surface turbulent heat fluxes and convective transport without making use of to the empirical parameterizations of the systemic parameters.

The maximum power generation hypothesis is analyzed on the diurnal time frame with an implementation of a simple modelling framework, consisting of the three vertically coupled reservoirs. First of all is the surface reservoir which apart from absorbing and releasing heat also regulates the surface evapotranspiration. The near surface layer of the atmosphere is represented with an energetic boundary layer reservoir, the heart of the atmospheric heat engine that facilitates the convective motions. The remaining top of the atmosphere reservoir is fundamental for the longwave radiation exchange in the system.

By performing a comparative data analysis of the model outputs with the observations from a high latitude field station in Hyytiälä, we prove that the maximum power generation limit provides reasonable first order estimates on the diurnal time scales, thus indicating that the system indeed operates near this thermodynamic limit. This indication implies an existence of a self-regulating mechanism in the system that optimizes the convective exchange between the surface and atmosphere accordingly with the state of maximum power generation. We propose a qualitative reasoning for such a functioning of the system. Furthermore, we demonstrate the added value of our simple approach in the modelling of the land-atmosphere interactions, as it requires only a limited number of generally accessible input variables such as solar radiation, surface temperature and water availability. Finally, we identify the limitations of the proposed framework and outline some improvements for the future research. We conclude by presenting the applicability of the maximum power generation limit in the more complex models, stressing its potentials for an improved general understanding of the land-atmosphere interactions.

Contents

List of Figures

Acknowledgments

I express my sincere gratitude to a number of people who have contributed to this research. First and foremost I would like to thank my supervisor Prof. Dr. Laurens Ganzeveld, who has introduced me to the topic of thermodynamic limits in the Earth System. The discussions we have had, his wholehearted assistance and moral support have helped me enormously to maintain the self-confidence, perseverance and eagerness for research.

I extend my deepest thanks to my co-supervisor Dr. Axel Kleidon, whose ability to convey the abstract thermodynamic concepts and to pose creative challenges decisively marked the invaluable learning experience of working at the Max Planck Institute for Biogeochemistry, Jena. I am grateful to the other colleagues from Biospheric Theory and Modelling Group: Dr. Maik Renner, Dr. Chiraq Dhara and Dr. Lee Miller, with whom I have been actively engaged in the conceptual design of my research. They have all provided me with constructive feedback and research suggestions which helped me to develop the modelling framework as well as to avoid the pitfalls on the way. I thank them as well for kindly hosting me at their research facilities in Jena. My appreciation also goes to Prof. Dr. Jordi Vila-Guerau de Arellano, for his helpful advice on the turbulent heat fluxes parameterizations.

This research would not be possible without the observation data. Observation data from the field station was a courtesy of AVAA, an open data publishing platform, initialized by the Finnish Ministry of Education and Culture. Radiosonde measurements were a courtesy of HUMPPA/COPEC field campaign, provided by the WUR Earth System Science Chair Group.

Lastly, I would like to thank the Slovene human resources development and scholarship fund for their financial support during the two year of my studies at the WUR.

Table of Abbreviations and Acronyms

Acronym/Abbreviation	Meaning
MEP	Maximum entropy production principle
MPP	Maximum power generation principle
GCMs	General circulation models
NEE	Net entropy exchange
EBL	Energetic boundary layer
TOA	Top of the atmosphere
LAI	Leaf area index
IPCC	Intergovernmental Panel on Climate Change
EC	Eddy-covariance method
RF	Radiative forcing
CBL	Convective boundary layer
ITCZ	Inter Tropical Convergence Zone

Table 0.1: Acronyms and Abbreviations in the order of reference.

Chapter 1

Introduction

The Earth system is in a thermodynamic state that is far from the equilibrium (Kleidon, 2010). Maintenance of thermodynamic disequilibrium can be attributed to several factors. First and foremost is the Earth's atmosphere, which traps longwave radiation, and concurrently acts as the fluid medium in global circulation. Together with spatially and temporarily varying insolation, the atmospheric characteristics enable a perpetual maintenance of the horizontal and vertical temperature gradients within the system, a clear indicator of disequilibrium. The atmosphere is by itself not unique to our planet, as it is found in all the "gaseous" planets of the Solar system as well as on Titan and Mars (Lorenz et al., 2001). Some other drivers of thermodynamic disequilibrium such as primary production and atmospheric chemical reactions can be partially or exclusively attributed to Earth's unique property, which is that it is a living planet (Lovelock et al., 1975). Its thermodynamic disequilibrium is further enhanced by physical and chemical interactions between the biosphere and geosphere (Kleidon, 2012). All the aforementioned processes contribute to the fact that Earth cannot be treated as a simple isolated thermodynamic system. In the presented study we will limit the analysis to the role of radiation and turbulence in the thermodynamic disequilibrium. Thermodynamic disequilibrium maintains a permanent temperature gradient between the surface and the atmosphere, which is driving the vertical heat transport. Then, a part of the heat in converted to potential energy, which is the source of the power for the atmospheric and oceanic motions (Ozawa et al., 2003). The process is quantified with two physical laws, namely, the first and the second laws of thermodynamics better known as the energy conservation law and the entropy law. The change in entropy of a system is defined as a summation of the supplied heat divided by the temperature of the system (Eq. 1.1), (Ozawa et al., 2003).

$$d\dot{S}_{system} = \frac{d\dot{Q}}{T} \tag{1.1}$$

Entropy production in the Earth System can be attributed to the radiative heating of the surface and the atmosphere and to the mixing of heat due to the vertical transport. Besides the entropy production within the system, the entropy is also perpetually exchanged

across the system's boundaries. The degree of heat exchange and entropy production is crucial for the determination of the strength of the circulation in the thermodynamic system. Paltridge (1979) suggested that the mean state of the present climate can be explained with maximum rate of entropy production due to horizontal heat transport in the atmosphere and oceans (Ozawa et al., 2003). The maximum entropy production principle (MEP) refers to the upper theoretical limit in the thermodynamic system. The application of the principle implicitly postulates that the system seeks to maximize its entropy. Since then, numerous researchers have been exploring the validity of the MEP hypothesis. Amongst the most promising fields of application is the turbulent heat transport (Kleidon et al., 2006) and the large scale horizontal transport (Grassl, 1981). Application of the thermodynamic limits represents a different physical approach in Earth systems modeling, when compared with the conventional climate and weather prediction models. When solving for local and global energy balance closure, conventional models apply the law of energy conservation, whereas the entropy in the system is not explicitly used, either as a state variable or as a physical constraint (IFS Model cycle - Cy40r1, 2013). In that way, disregarding the entropy in the conventional model frameworks increases the degree of underdetermination in the system. These models resolve the issue with an introduction of prescribed empirical parameters, which relate the exchange quantities, e.g. heat or momentum, to the gradients of the driving variables. In the systems where the MEP hypothesis was found to be true, application of the limit eliminates the need for prescribing the parameters. The thermodynamic limits therefore offer an opportunity to improve the physical consistency and quality of the turbulent transport projections in the models.

The main topic of the thesis is the modelling of turbulent heat transport in a small-scale surface-atmosphere column within the diurnal scales. The working hypothesis of the framework is that the turbulent transport at any given time of the day adheres to the maximum power generation principle (MPP), which is a particular example of the MEP principle. We provide a brief summary the selected research on the MEP hypothesis. We then introduce the proposed MPP framework with three model illustrations, each consecutive model adding an additional degree of complexity to the system. In the first model illustration we briefly introduce the notion of the Earth system as a thermodynamic machinery consisting of the atmospheric and surface heat reservoirs. Using the first and second laws of thermodynamics, we explain how the disequilibrium state is maintained and prove that as a consequence the Earth System can be treated as a heat engine. In the second model, where the atmosphere and surface are assumed to be in a thermodynamic steady state, we extend the framework with an atmospheric engine performing at the MPP limit, which is driven by vertical heat transport. In the following subsection we outline the final model framework with the energetic boundary layer extension, thus laying the foundations for the radiative and convective heat engine model, a conceptual alternative to the conventional climate models. Finally, we present the particular objectives of the thesis research.

1.1 Applications of the Thermodynamic Limits in Research

A wide spectrum of conducted research has shown that certain thermodynamic processes of the Earth system can be adequately modeled by employing the MEP or MPP principle. Only a handful of articles shall be mentioned to provide a brief overview of the research on the topic.

Most of the studies tested the adequacy of the thermodynamic limits for large scale systems. With a simple zonally averaged energy balance climate model, Grassl (1981) tested the hypothesis that large-scale meridional motions act in accordance with the maximum entropy production. The MEP principle was used as a constraint to solve the system of the four unknowns - meridional fluxes, surface heat fluxes, cloud cover and temperature. The hypothesis showed satisfactory agreement between the model outputs and observations with respect to the temperature, meridional heat fluxes and cloud cover. Thermodynamic limits were also tested in more complex models. Kleidon et al. (2003) conducted sensitivity simulations of an atmospheric general circulation model subjected to the MEP constraint, by adjusting model resolution and friction to represent turbulence in the boundary layer. The authors emphasize the importance of using sufficiently high model resolution and relevant boundary layer drag parametrizations to adequately simulate the equator-poleward heat transport. The MEP limit also suggested that the general circulation models (GCMs) tend to underestimate the atmospheric heat transport and therefore overestimate the equator-pole temperature gradient (Kleidon et al., 2003). It is remarkable how the application of the MEP principle enables even relatively simple zonally averaged energy balance models to reproduce certain properties of much more complex GCMs.

Application of the MEP principle in the zonally averaged energy-balance models was also proven as a helpful approach on other planetary objects in the Solar system. It was demonstrated by Lorenz et al. (2001) that meridional heat diffusion on Mars and Titan is far better constrained by the use of the MEP, in comparison to a more complex but commonly used parametrization in Earth system models, which is a function of surface pressure, heat capacity and angular rotation. Furthermore, the MEP based approach also results in a fairly good prediction of the annually averaged temperatures for the tropics and polar regions of the planets. In Kleidon, Renner and Porada (2014), the applicability of the MPP concept to study the Earth's surface energy balance and hydrological cycle was demonstrated, arriving at reasonable first-order estimates of the annually averaged surface heat fluxes for a large number of observation sites, only using the solar radiation and water availability measurements. Further on, the modeled evaporation fluxes and runoff across major river basins matched reasonably well with the observations. The research indicates the MPP principle can also be applied within smaller-scale systems (e.g., catchments/river basin scale), if all the major energy flows and the annual hydrological cycle within the boundaries of such systems can be inferred. Application of the MPP principle makes

it possible to model first-order estimates of the surface fluxes, using only a handful of necessary measured variables at the site, namely the net solar radiation at the surface and precipitation. This observation puts the MPP in a perspective, where it could become a promising prognostic tool for the turbulent heat flux projections, especially in the regions where observation data are scarce, since average solar radiation and even precipitation can be determined by a use of remote sensing instruments or be even stochastically modelled from climatological means.

The presented scope of research suggest that certain processes in the Earth systems operate near their thermodynamic limits. In the systems where adherence to one of the thermodynamic limits is clearly identified, this provides a valuable constraint to the physical dynamics of the thermodynamic processes.

1.2 Thermodynamic Limits in Earth Systems Science

1.2.1 Thermodynamic Disequilibrium of the Earth System

Maintenance of thermodynamic disequilibrium can be illustrated with a simple two reservoir model illustration, adapted from Kleidon (2010). The model consists of two heat reservoirs, representing the surface and the atmosphere each at its respective temperature and heat capacity (Fig. 1.1). There is heat exchange with outer space, originating from solar radiation $J_{in,s}$ & $J_{in,a}$ and emission of longwave radiation, either through the atmospheric window $J_{out,s}$ (surface reservoir) or atmospheric longwave emission $J_{out,a}$ (atmospheric reservoir). Space can also be thought of as a boundary condition reservoir at the constant temperature T_{sun} that is supplying energy to the Earth. Heat J_{heat} is exchanged across the Earth's reservoirs, from the warmer surface into the atmosphere. In the absence of any work done by the system, the first law of thermodynamics yields an expression for the change in the surface (Eq. 1.2) and atmospheric (Eq. 1.3) reservoir temperatures T_s & T_a:

$$c \cdot \frac{dT_s}{dt} = J_{in,s} - J_{out,s} - J_{heat} \tag{1.2}$$

$$c \cdot \frac{dT_a}{dt} = J_{in,a} - J_{out,a} + J_{heat} \tag{1.3}$$

The entropy production budget of the total system $\frac{dS_{tot}}{dt}$ consisting of both surface $\frac{dS_s}{dt}$ and atmospheric reservoirs $\frac{dS_a}{dt}$ is a product of three processes: entropy mixing with space $\sigma_{mix,s}$ & $\sigma_{mix,a}$, entropy mixing associated with heat transport between the surface and atmosphere σ_{heat} and entropy exchange across the system's boundaries NEE (Eq. 1.4). The entropy production components that are indicated as sigmas all share the same functional formulation e.g. Eq. 1.7. The formulation represents a heat transfer from one reservoir to another one, thus effectively energetically mixing the reservoirs.

$$\frac{dS_{tot}}{dt} = \frac{dS_s}{dt} + \frac{dS_a}{dt} = \sigma_{mix,s} + \sigma_{mix,a} + \sigma_{heat} - NEE \tag{1.4}$$

Entropy mixing with space, i.e. with the sun, is calculated by as heat transfer $J_{in,s}$ & $J_{in,a}$ between the respective reservoirs of the Earth and Sun, which is according to Kleidon (2010):

$$\sigma_{mix,s} = J_{in,s}(\frac{1}{T_s} - \frac{1}{T_{sun}}) \tag{1.5}$$

$$\sigma_{mix,a} = J_{in,a}(\frac{1}{T_a} - \frac{1}{T_{sun}}) \tag{1.6}$$

Entropy mixing by the heat flux J_{heat},which is exchanging heat between the surface and atmospheric reservoir is written in a similar fashion (Eq. 1.7).

$$\sigma_{heat} = J_{heat}(\frac{1}{T_a} - \frac{1}{T_s}) \tag{1.7}$$

So far we have characterized the entropy input into the system (Eqs. 1.5 and 1.6) from the sun and entropy production within the system (Eq. 1.7). Finally, we must not forget about the net entropy exchange (NEE) across the Earth system's boundaries (Eq 1.8). The NEE is a difference between the outgoing entropy due to the Earth's surface and atmospheric longwave radiation and the incoming entropy from the solar radiation.

$$NEE = (\frac{J_{out,s}}{T_s} + \frac{J_{out,a}}{T_a}) - (\frac{J_{in,s} + J_{in,a}}{T_{sun}}) \tag{1.8}$$

The formulation in Eq. 1.4 explains the underlying processes of the disequilibrium. One can notice that disequilibrium is maintained due to energy exchange across the Earth's boundaries, the driving force of all the entropy production terms except for the mixing heat term σ_{heat}. Were the Earth System isolated, the total entropy would reach a maximum value, determined exclusively by the weakening heat mixing term. The heat exchange between the surface and the atmosphere would deplete the temperature gradient up to a point where the system would have reached a thermal equilibrium. That is not the case because the energy input from the Sun maintains the temperature gradient in the vertical, thus facilitating the permanent export of entropy through the system's boundaries. Finally, the resulting heat flux and the prevailing temperature gradients are a source of potential energy that drive the atmospheric and oceanic motions.

1.2.2 Maximum Power Generation of the Atmospheric Heat Engine

We can illustrate the ability of the atmosphere to preform work by describing it as a heat engine. Atmospheric heat engine is an idealized system that illustrates the conversion

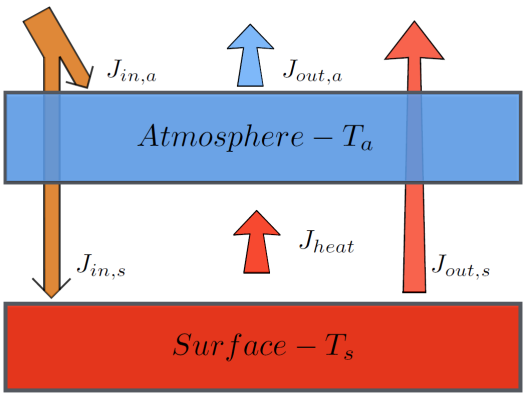

Figure 1.1: A simple two reservoir model. Schematic representation of the energy fluxes in the Earth system that is in a state of thermodynamic disequilibrium. The system consists of the surface reservoir with temperature T_S and the atmospheric reservoir with temperature T_A. The surface is warmed due to absorbed solar radiation flux $J_{in,s}$ and cooled by the outgoing longwave radiation (atmospheric window) $J_{out,s}$, whereas the atmosphere is warmed by the solar radiation flux $J_{in,a}$ and cooled by atmospheric radiation $J_{out,a}$. The surface absorbs more energy from the Sun than atmosphere. This heating difference results in a temperature difference between the reservoirs that drives the vertical heat transfer from a warmer (T_S) to a colder (T_A) reservoir J_{heat}. Adapted from Kleidon et al., (2014).

of turbulent heat fluxes into convective motions. We follow the steps of the framework presented in Fig. 1.1, extending it with such a heat engine, locked between the surface and the atmosphere, which together with the heat engine constitute the bigger energetic system (Fig. 1.2). The following part of the derivation only focuses on the smaller heat engine system, which is why for the time being we omit the energy balance at the surface and the atmosphere and the corresponding thermodynamic disequilibrium equations. The system is assumed to be in a steady state, implying constant temperatures of both reservoirs and no change in the internal energy and entropy of the system. This assumption is only used at this point of the presentation in order to simplify the derivation, whereas the steady state assumption is not applied in the final model framework. The engine is powered by the heat flux, running from the surface J_{heat}. Like in any heat engine, a part of the heat flux is used to extract power P_{ex}. Also, one must not forget to include the dissipative processes D in the atmosphere, which provide an additional heating source for the engine. That is because the power, which manifests itself in convective motions, is eventually dissipated within the heat engine and is therefore not extracted to be used outside the heat engine system as is the case for a mechanical heat engine (Kleidon and Renner, 2013). Furthermore, there is a justification why the dissipation term was fed back to the the heat engine's input. The friction is strongest close to the surface, which is why the bulk of dissipation occurs in the lower part of the boundary layer, i.e. close to the surface (Stull, p.155, 1988). Starting from the first law of thermodynamics, we obtain

the energy balance equation of the small heat engine system (Eq. 1.9). The heat inputs J_{heat} and D are supplied to the engine from the surface, whereas J_{out} is the output at the atmospheric reservoir, after a fraction of the surface heat was converted into power.

$$J_{heat} + D - P_{ex} = J_{out} \tag{1.9}$$

At this point we apply the steady state assumption between the dissipation and power generation $P_{ex} = D$. Even though this assumption cannot be justified at diurnal time scales, it is a simplification that has to be applied at this stage to obtain a determined system of equations. Also, the power generation and dissipation terms are about an order of magnitude smaller than the other terms in the energy balance equation, which is why the simplification should not play a detrimental role in the model. The net entropy exchange of the system consists of J_{heat} and D, added at a temperature T_s and J_{out} removed at a temperature T_a (Eq. 1.10). Using the second law of thermodynamics (Eq. 1.1), we know that maximum power is extracted from a smaller heat engine when no irreversible processes take place within the system i.e. when the rate of entropy production within the system and its exchange across the boundaries equals zero (Eq. 1.10) (Kleidon, 2010). Note that the maximum power extraction occurs when the entropy production within the smaller system is at its theoretical minimum. However, this does not contradict with the state of disequilibrium, which is preconditioned on a positive entropy production of the entire energetic system. The disequilibrium within that system is sustained and the entropy production remains positive (Eq. 1.6), as the MPP principle adheres only to the smaller atmospheric heat engine system (Eq. 1.10 and Fig. 1.2).

$$\frac{dS_{system}}{dt} = (\frac{J_{heat} + D}{T_s} - \frac{J_{out}}{T_a}) = 0 \tag{1.10}$$

Inferring J_{out} from Eq. 1.9 and inserting it into Eq. 1.10 we obtain the MPP limit (Eq. 1.11). The limit that adheres to the zero entropy production is commonly known as the Carnot limit, even though the derived limit slightly differs from the original theoretical Carnot limit (Kleidon, 2012). That is because in the presented model the power is not extracted from the engine, but rather fed back into the system as heat in the form of dissipation. It is evident from the Eq. 1.11 that power extraction is proportional to the temperature gradient and the heat flux. These terms are in fact interdependent; the temperature gradient is driving the convective heat transfer, which is at the same time depleting the gradient. As much as both factors contribute to the maximum power extraction they are jointly also its limiting factors.

$$P_{ex} = J_{heat}\frac{T_s - T_a}{T_a} \tag{1.11}$$

We should keep in mind that the model's simplicity implies the use of some essential assumptions. Firstly, a steady state was assumed where dissipation equals the power generation and the temperature gradient is in balance with the heat flux. Within diurnal

time scales, particularly during the boundary layer evolution, such steady state is not an adequate assumption (Kleidon et al. 2014). What one usually observes is a power-intense buildup of boundary layer in the morning followed by a period of an approximate steady-state around the afternoon, before the dominating dissipation breaks down the boundary layer at the end of the day. Also, a two reservoir model aggregates very distinct properties of the atmosphere in only one atmospheric reservoir, thus failing to capture pronounced diurnal cycles within the bottom part of the atmosphere, namely the boundary layer. The described model also considers that the heat flux is only driven by the surface fluxes, thus disregarding horizontal heat advection that occurs frequently with passing of the fronts and other synoptic weather systems. This thesis is to a large extent an attempt to prove these shortcomings can be overcome or be at least significantly reduced by an introduction of an additional, energetic boundary layer reservoir. Nevertheless, even the simplest thermodynamic limit frameworks have already proven its ability to accurately model the dynamics of some essential planetary processes, as we have demonstrated in the literature overview section.

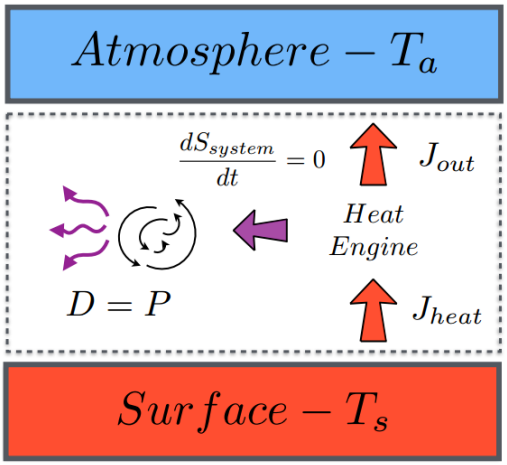

Figure 1.2: A simple two reservoir model with a heat engine system. The scheme illustrates functioning of the atmospheric heat engine that operates at the MPP limit. The heat engine is primarily driven by the surface heat flux J_{heat}, a fraction of which is transferred into power P (represented with a violet arrow) that drives turbulent convective motions. Convective motions are being dissipated at the surface D (three violet arrows), thus providing an additional heat input in the engine. The remainder of the heat flux that is not utilized in the conversion to power J_{out} is transferring heat to the atmospheric reservoir. Adapted from Kleidon and Renner (2014).

1.3 Energetic Boundary Layer, a Heart of the Atmospheric Heat Engine

1.3.1 Energetic Boundary Layer Extension of the Two Reservoir Model

An atmospheric heat engine is characterized by a rather peculiar fact concerning its power source. Although entirely dependent on the incoming solar radiation, the engine is not driven directly by that source. On the contrary, the atmospheric heat engine is predominantly driven by the surface sensible heat flux which facilitates convective exchange between the surface and the atmosphere, a consequence of the Earth's surface capacity to better absorb shortwave energy from the penetrating solar radiation than the air. On a sunny day the surface heats up more efficiently than the atmosphere. This results in a temperature gradient between the surface and the near surface atmospheric layer which starts the turbulent heat transport in the vertical, thus warming the surface atmospheric layer. With some delay the heated surface atmospheric layer transfers a part of the received energy to the layer above. What we observed is a gradual heating of the atmospheric column up to a point where the surface triggered heating completely diminishes. We define that part of the atmosphere as the energetic boundary layer. Note that the proposed definition of the boundary layer differs from the one applied in boundary layer meteorology, where the boundary layer thickness exhibits a large temporal variability on the diurnal scale. Alternatively, the energetic boundary layer (EBL) is defined as a reservoir with a fixed upper boundary, which separates the atmospheric layer, which internal energy is significantly influenced by the surface at any given time of the diurnal cycle from the rest of the atmosphere (Kleidon and Renner, 2014). An educated guess, based on the EBL observations at high latitude field stations informs us that a fixed boundary should be set at approximately 400 hPa above surface pressure.

Differential heating and cooling in the vertical is an important property of the atmosphere that can not be represented by the simple model presented in the subsection 1.2.2. In that model the transfer of heat is assumed to take place uniformly from the surface reservoir to the atmospheric one. In truth however, the atmosphere as a whole is non-uniform in its thermal properties (Stull, 1988). Whereas the surface layer features temperatures comparable to those of the surface, the top of the troposphere usually exhibits temperatures that are several tens of degrees lower. Therefore, it is reasonable to partition the one uniform atmospheric reservoir into layers. We have partitioned the atmosphere into two reservoirs, the first one being the aforementioned EBL and the second one top of the atmosphere (TOA). Hence, the aggregates the entire atmosphere above the boundary layer into one reservoir. The EBL on the other hand is where differential diurnal heating takes place and thus also serves as a reservoir for the heat storage and release H_a. The EBL is being heated during the day. Therefore, a part of the energy, supplied by the surface, is stored in the EBL. At the night time however, the EBL gradually cools

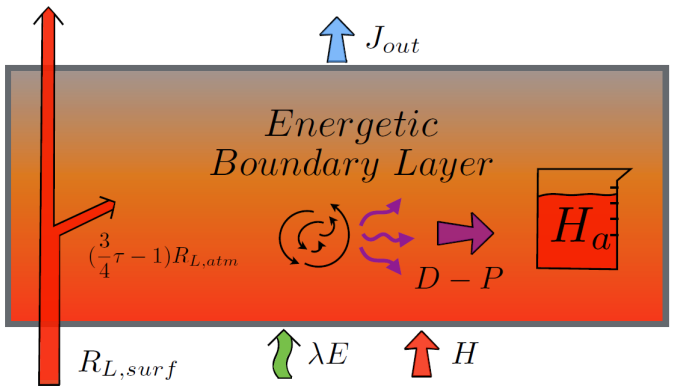

Figure 1.3: An illustration of the EBL, an atmospheric reservoir positioned between the surface and TOA. The EBL is a "small" thermodynamic system that performs as a medium of the atmospheric heat engine, driven by the surface turbulent fluxes H & λE and the absorbed longwave radiation $(\frac{3}{4}\tau - 1)R_{L,atm}$. Apart from facilitating the convective motions in the system, as described in Fig. 1.2, the EBL also stores and releases heat. The heat storage of the system H_a is portrayed with a "measuring jug", thus indicating the energetic state of the system.

down and as a result, releases heat into the TOA. The EBL is also heated by longwave absorption. Containing a high density of water vapor, the EBL plays an important role in the greenhouse effect.

The EBL extension thus provides an additional reservoir to the framework. Due to its heat containing properties, a new reservoir also affects the entropy production in the system. Further implications and a complete derivation of the extended framework are too extensive to be explained in the introduction and will therefore be presented in the following chapters, namely. For now let us just keep in mind that by altering the entropy production, the boundary layer extension also influences the power limit of the system, which affects the partitioning of the turbulent fluxes. At first sight, an introduction of the EBL heat storage looks only as a slight modification in the system. However, it turns us to be an essential one, as it allows us to capture convective and radiative dynamics of the system on diurnal time scales.

1.4 Objectives and Aims of Thesis Research

Numerous research studies, which have been previously discussed, indicate that application of the thermodynamic limits clearly has a potential in the Earth Systems modelling. Yet, its scope and a particular use within more complex systems is still largely unclear and therefore remains to be resolved. That determined a starting point which set me on a path of trial and error to devise an alternative framework. From the start the research was aimed at modelling land-atmosphere dynamics for small-scale ecological systems, centered

around two key aspects. The first main theme of study was the temporal dynamics of the surface turbulent fluxes, which drive the land-atmosphere exchange, associated with vertical convection, while the second topic to be investigated was the use of the MPP concept in the boundary layer growth dynamics. Early stages of research have shown that modelling of the boundary layer dynamics would require an additional degree of complexity in the model associated with inevitable modelling of vertical temperature profiles which was beyond my capabilities within a relatively narrow time frame. Consequently, the research emphasis has moved towards the use of the MPP concepts as a tool to analyze diurnal variability in surface energy fluxes. Nevertheless, as a consequence of a closed energy balance in the atmospheric column we can besides the turbulent fluxes also get an additional insight into the other energy fluxes in the column.

With their model, Kleidon, Renner and Porada (2014) have proven that the application of the MPP provides reasonable first-order estimates for annually averaged surface heat fluxes. A major goal of this research is to transform this simple model into a non-steady state framework that will be able to project reasonable first-order estimates on much shorter diurnal time scales. The centerpiece of the framework will be an atmospheric column energy equilibrium model, where the EBL is treated as a convective and radiative atmospheric heat engine with a temporally varying heat storage that performs at the MPP limit. A step-wise modular design approach is proposed, where the model's framework is complemented with new sources and drivers of the land-atmosphere exchange, thus improving physical consistency and precision of the model. The model will consist of the following modules: a soil moisture module for calculating water availability, a soil heat flux module and vegetation module for estimating stomatal conductance, a key regulator of the latent heat transpiration (Jarvis, 1976).

The model's performance will be evaluated by a comparison of the projected turbulent heat fluxes with the observations from a high latitude field station in Finland, Hyytiälä. After the quality assessment of the model projections, a potential further application of the proposed framework to study surface energy exchange at other sites and also a possible implementation of the MPP principle in the more complex general circulation models will be discussed.

Special attention in our research will be given to an examination of the EBL heat storage term H_a, a crucial part for the diurnal extension of the atmospheric heat engine. The EBL heat storage is a fundamentally new concept in the land-atmosphere interaction studies that was in a rudimentary form proposed by Kleidon and Renner, (2014). For that reason, it is still largely unknown whether our perception of the storage term and its temporal variability corresponds to the actual diurnal energy dynamics in the EBL. Therefore, one of the aims is to validate the conceptual construction of the EBL heat storage by comparing the modelled diurnal evolution of the storage term with an analytical calculation from radiosonde measurements. The model will also be used for studying the effects of changing climatological conditions, especially a projected greenhouse enhancement on the partitioning of the surface fluxes, vertical transport and as a control experiment, mean surface temperature. Conclusions from sensitivity analysis will be com-

pared with trends from the IPCC climate projections. A detailed physical explication of the framework, including description of the selected modules and conducted experiments, will be provided in the thesis report.

1.4.1 Research goals

1. To construct a physically consistent modelling framework and test whether the atmosphere performs as a thermodynamic heat engine, subjected to the maximum power limit.

2. To devise such an alternative approach to model surface turbulent heat fluxes, which would require only a limited number of measured variables.

3. To study the effects of a changing climate on the partitioning of the surface turbulent heat fluxes, vertical transport and mean temperature, using sensitivity analysis to an enhanced greenhouse effect.

4. To explore a potential applicability of the maximum power generation limit in the more complex models.

1.4.2 Hypotheses

1. Turbulent heat transport between the surface and the atmosphere can be interpreted as the driving force of the atmospheric heat engine that is operating at its theoretical maximum power generation limit.

2. Application of the maximum power generation principle in the atmospheric heat engine leads to reasonable first order projections of the diurnal surface turbulent heat fluxes, using only a limited number of generally accessible input variables.

3. Energetic boundary layer heat storage H_a captures the diurnal variations of energy in the atmospheric layer that is energetically influenced by the surface.

Chapter 2

Modelling Framework

Aim of the Introduction chapter was to provide a brief explanation of the key thermodynamic processes behind the atmospheric heat engine. The outline was complemented with an indication about the framework's potential applications which will be assessed in this thesis. The goal of this chapter is to further present the most salient features of the model framework. We will start with a description of the column energy balance model, constructed for the purposes of our research. Further on, the design of a soil heat flux, a soil moisture and vegetation modules, which are coupled to the energy balance framework will be briefly presented. Key aspects of the extensive framework will be holistically captured in a comprehensive model graphics scheme.

2.1 Equations of the Radiative and Convective Atmospheric Heat Engine with the MPP Limit

For the purpose of a holistic understanding and application of the framework, we now make a step beyond the previously presented conceptual reasoning by quantifying the flows of energy and entropy in the system. We start with energy balance equations at the surface, energetic boundary layer and top of the atmosphere. When separating the energy components, we follow the global radiation budget scheme by Trenberth et al., (2009). A set of energy balance equations is presented with incoming components on the left-hand side of equations and outgoing on the right-hand side. Afterwards, the MPP limit of the extended framework is inferred from energy balance of the heat engine and the entropy law (Kleidon and Renner, (2013) and Renner (2014)). Throughout derivation, it might be helpful to keep the comprehensive model scheme in mind (Fig. 2.2).

2.1.1 Surface Energy Balance

$$(1-\varphi)R_s + \frac{3}{4}\tau R_{L,atm} = R_{L,surf} + H + \lambda E + Q_g \tag{2.1}$$

Total absorbed solar radiation at the surface and in the atmosphere R_s is partitioned into the part that is absorbed by the atmosphere φR_s and therefore not available at the surface, and the component which is absorbed at the surface $(1-\varphi)R_s$ (Eq. 2.1). An additional energy input is provided by the atmosphere, which radiates in the longwave spectrum as a gray body $R_{L,atm} = \sigma T_a^4$ (Nakajima et al., 1992). In the process of atmospheric downward radiation transfer the longwave radiation component is increased by the radiative properties of the greenhouse gases (Inamdar et al., 1998). The downgoing longwave radiation is commonly known as the greenhouse effect and is in our model parameterized as $\frac{3}{4}\tau R_{L,atm}$. This parametrization accounts for the greenhouse enhancement of the incoming longwave radiation by applying a spectrally uniform Gray atmosphere model with Eddington's approximation, where we assign a multiplier that is proportional to the optical depth τ of all the greenhouse gases (Nakajima et al., 1992). The details of the Gray model are not essential in order to understand the column energy balance model. The essential feature is that the optical depth in the radiative transfer relates to the atmospheric ability to absorb and emit longwave radiation. Specific dependance of the optical depth on greenhouse gases concentrations and other variables is beyond the scope of this thesis study. The incoming fluxes are balanced by the outgoing longwave radiation $R_{L,surf}$ and surface turbulent heat fluxes, namely the sensible and latent components H and λE. Additionally, a small energy fraction is either being stored or released from the ground by the soil heat flux Q_g.

2.1.2 Energetic Boundary Layer Energy Balance

It was explained in the introduction that, besides functioning as a medium for extracting power, the EBL also stores and releases heat. For that reason the energetic boundary layer heat storage term H_a was introduced. The storage term is a difference between the heat flux input $(\lambda E + H + D + (\frac{3}{4}\tau - 1) \cdot R_{L,atm})$ in the heat engine and the sum of power generation P and the outgoing fluxes J_{out} from the engine (Eq. 2.2).

$$\lambda E + H + (\frac{3}{4}\tau - 1) \cdot R_{L,atm} + D - P - J_{out} = H_a \tag{2.2}$$

It was also explained that the engine is powered by the surface turbulent heat fluxes and the absorbed longwave radiation. The EBL is the most dense part of the atmosphere with respect to water vapor, a highly absorbent greenhouse gas in the longwave spectrum, which is why the EBL is partially also heated and cooled by a recurrent absorption and emission of longwave radiation (Held and Soden, 2000). The amount of longwave radiation that is "trapped" in the boundary layer is not easy to determine since it is temporally highly variable as it depends on numerous factors, such as the water content and its vertical distribution in the atmosphere, inclination of the sun and cloud cover amongst others (Inamdar et al., 1998). In an elementary model such as ours, these factors are far too complex to be explicitly included. For that reason, the absorbed longwave radiation term in the EBL was resolved with a simple approach. Knowing that the longwave

radiation emitted at the TOA equals $R_{L,atm}$ and that the incoming longwave radiation at the surface equals $\frac{3}{4}\tau R_{L,atm}$, implies the difference in the terms comes from the the greenhouse-enhancing property of water vapor. Water vapor is by far the most important greenhouse gas in the atmosphere (Held and Soden, 2000) with most of the water vapor content situated in the EBL part of the atmosphere. For that reason, the greenhouse enhancement of the downgoing longwave radiation $(\frac{3}{4}\tau - 1)R_{L,atm}$ was attributed to the water vapor in the EBL (Fig. 2.1). The source of the longwave radiative heating in the boundary layer comes from the surface outgoing longwave radiation that is partially absorbed in EBL (Fig 2.1). Accordingly, we assume that the amount of the outgoing surface longwave radiation, absorbed in the boundary layer, equals the greenhouse enhancement. The proposed solution, depicted in Fig. 2.1, therefore follows a typical text-book illustration, portraying the greenhouse effect as a radiation recycling mechanism (Trenberth et al., 2009).

When inserting the surface and TOA energy balance equations, presented in the following subsection (Eqs. 2.1., 2.4 and 2.7) in Eq. 2.2, the EBL heat storage term can be written as a function of external forcing:

$$H_a = (1 - \varphi)R_s - Q_g - (1 - \varphi)\overline{R_s} \tag{2.3}$$

The latter expression enables a clearer interpretation of the heat storage term. According to Eq. 2.3, the EBL stores the remaining energy from the surface solar radiation $(1 - \varphi)R_s$ that is not absorbed by the soil Q_g or released in outer space $(1 - \varphi)\overline{R}_s$ (Eqs. 2.3 and 2.7). Such formulation intuitively makes sense, as it presents the storage term in a form of a residual reservoir, which implicitly stems from our definition of the energetic boundary layer.

2.1.3 Top of the Atmosphere Energy Balance

The TOA reservoir receives energy from the surface $R_{L,surf}$. Due to the greenhouse effect, a part of the surface outgoing longwave is absorbed in EBL, thus decreasing the absorbed longwave radiation in the TOA reservoir. The other source of energy for the reservoir comes from the outgoing convective heat engine flux J_{out}. Additionally, the atmosphere is heated up by a proportion of the total incoming solar radiation φR_s. The atmosphere releases received energy in the form of gray body radiation, which is according to the Stefan-Boltzmann law a function of the reservoir's temperature $R_{L,atm} = \sigma T_A^4$ (Inamdar et al., 1998). Radiation is emitted back to the surface as well as into space, the downgoing component being enhanced by the greenhouse effect. The total outgoing radiation from the TOA reservoir therefore equals $(1 + 1 \cdot \frac{3}{4}\tau)R_{L,atm}$. A complete energy balance equation for the TOA reservoir is shown in Eq. 2.4.

$$R_{L,surf} - (\frac{3}{4}\tau - 1) \cdot R_{L,atm} + J_{out} + \varphi R_s = (1 + \frac{3}{4}\tau)R_{L,atm} \tag{2.4}$$

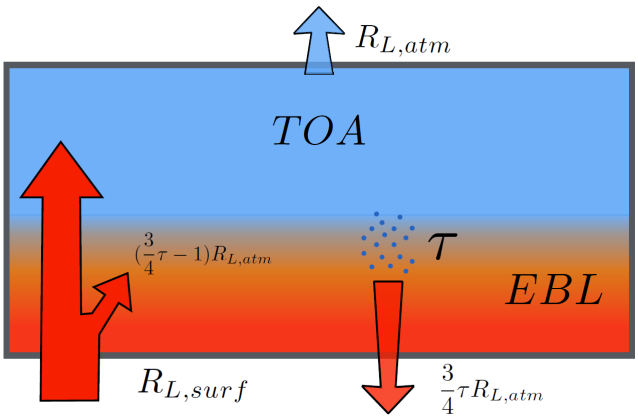

Figure 2.1: The scheme illustrates the EBL and TOA reservoirs that jointly constitute the atmosphere and the longwave fluxes in the system. The outgoing longwave radiation at the surface $R_{L,surf}$ is partly absorbed in the EBL and partly in the TOA. The TOA radiates to outer space $R_{L,atm}$ and back to the surface $\frac{3}{4}\tau R_{L,atm}$. The downgoing longwave radiation from the TOA is enhanced due to radiative properties of the greenhouse gases τ. (Adapted from Trenberth et al., 2009).

By averaging Eq. 2.4 and deducing the averaged expression from the same equation, we obtain an additional constraint to the atmospheric energy balance (Eq. 2.5). The derivation steps are a pure technical routine of applying daily averaging rules and are as such hereby omitted.

$$R_{L,atm} = \overline{R_{L,atm}} + \varphi(R_s - \overline{R_s}) \tag{2.5}$$

A closed energy balance in the atmospheric column postulates that the diurnal average of incoming solar radiation equals the daily average of outgoing longwave radiation at the top of the atmosphere, therefore:

$$\overline{R_{L,atm}} = \overline{R_s} \tag{2.6}$$

After inserting Eq. 2.6 into Eq. 2.5, we can see that the temporal atmospheric longwave term equals the average solar radiation at the surface plus a variable proportion of the total incoming solar radiation:

$$R_{L,atm} = (1 - \varphi)\overline{R_s} + \varphi R_s \tag{2.7}$$

Finally, we must address the simplifications, which were made in the derivation of Eqs. 2.1 - 2.7, and the consequent limitations of the framework. We assume the whole atmospheric column (EBL and TOA) as completely opaque, which implies that there is no longwave penetration of the atmosphere. This simplification, which effectively neglects the existence of the atmospheric window flux (Trenberth et al., 2009), was not intended in the initial framework design. Unfortunately, adding the atmospheric window has made

the system underdetermined as we could not come up with an additional equation. We thus complied with the opaque atmosphere assumption, which implications will be thoroughly addressed in the results and discussion chapters. Horizontal heat advection in the atmospheric column is also neglected. An addition of that term would require a temporal determination of the flux at the systems's boundaries, requiring a multitude of measurements around the modelling observation site. For average meteorological conditions, the horizontal advection is not the dominating term in the column energy balance. Grimmond and Oke (1995) supported this claim in an evaluation of the urban energy balances, where horizontal advection plays a more important role due to the anthropogenic heat flux. They conclude that horizontal advection is difficult to evaluate, but can probably be neglected. We have also excluded the effects of clouds, which not only vary the partitioning of solar radiation absorption at the surface and atmosphere φ, but also significantly alters the greenhouse effect (Trenberth et al., 2009).

2.1.4 Power of the Atmospheric Heat Engine

So far a set of energy balance equations was presented. Now we complement the set by assuming that the atmosphere works as a heat engine performing at the MPP limit. This proposition distinguishes the proposed framework from conventional energy balance models, which do not (explicitly) apply the entropy law in the system closure. We start by evaluating the entropy production in the heat engine. Heat transfer is analogous to the system, described in section 1.2.2 (Eq. 1.10). With an introduction of the EBL this intermediate reservoir is not just transferring heat from the surface to the atmosphere, but is also exchanging heat as it is being warmed up or cooled down. For this reason, a EBL entropy production term $\frac{dS_b}{dt}$ is introduced (Eq 2.8).

$$\frac{J_{in}}{T_S} - \frac{J_{out}}{T_A} = \frac{dS_b}{dt} \tag{2.8}$$

A general idealization of the boundary layer and atmosphere is that it consists of two gases, i.e. dry air and water vapor, commonly assumed to adhere to an ideal gas law. The entropy state of any ideal gas can according to Hauf and Höller, (1987) be written as:

$$S = c_p ln(\frac{T}{T_{ref}}) - R \cdot ln\frac{p}{p_{ref}} + S_{ref} \tag{2.9}$$

where R is the gas constant, c_p specific heat at constant pressure and the ref index an arbitrary reference state of the system. Mathematically speaking the reference state is a constant of integration which drops out in our analysis, since we are not really interested in the absolute amount of entropy in the system, but rather in the entropy changes of the system. The entropy can be expressed more compactly using the definition of a potential temperature for moist air $\theta_i = T_i(\frac{p_0}{p_i})^{\frac{R}{c_p}}$(Hauf and Höller, 1987). Inserting the latter expression in Eq. 2.9, we get:

$$S = c_p ln \frac{\theta}{\theta_{ref}} + S_{ref} \tag{2.10}$$

The entropy state of the EBL is thus directly related to the potential temperature for moist air (Eq. 2.10). As we know from boundary layer meteorology, the dynamic boundary layer tends to have a non-static vertical profile of potential temperature, which is also true for the EBL (Stull, p.284, 1988). A simple reservoir approach does not explicitly allow such a degree of complexity. Therefore, a bulk potential temperature of the EBL is introduced $< \theta_b >$, a variable which represents an average potential temperature and consequently also the energy and entropic state of the reservoir. With an introduction of the bulk temperature, the EBL entropy production term can now be written as a derivative of Eq. 2.10:

$$\frac{dS_b}{dt} = \frac{\rho c_p h \cdot d < \theta_b >}{< \theta_b > dt} \tag{2.11}$$

where h represents a static EBL height. The numerator in the equations actually stands for the heat storage or release within the EBL. Besides being an indicator of the entropy production in the system, the average temperature in the column$< \theta_b >$ is also a representative value of internal energy in the EBL calculated as $\rho c_p h \cdot < \theta_b >$. Heating of the boundary layer is provided by a sum of the surface sensible heat flux and greenhouse longwave absorption $(\frac{3}{4}\tau - 1)R_{L,atm}$, whereas the EBL is cooled down by the outgoing heat flux (Eq. 2.12).

$$\rho c_p h \cdot \frac{d < \theta_b >}{dt} = H + (\frac{3}{4}\tau - 1)R_{L,atm} - J_{out} \tag{2.12}$$

In absence of moisture condensation, the surface latent heat flux only provides moisture into the system and should therefore not be included in the equation. Exclusion of the latent heat flux is the only difference between the internal energy of the EBL and EBL heat storage H_a, where latent heat is also included. We have assumed no condensation in the entropy production equation because the physics behind the process is just too complex to model. On days when there is very little or no precipitation, the released latent heat does not play a role in the entropy production of the engine making this a valid assumption.

We once more apply the steady state assumption between power generation and surface friction dissipation $P = D$. The right hand site of Eq. 2.12 thus equals $H_a - \lambda E$ (Eq. 2.2). We insert the latter term in Eq. (2.12) to finally obtain an expression for the EBL entropy production:

$$\frac{dS_b}{dt} = \frac{H_a - \lambda E}{< \theta_b >} \tag{2.13}$$

We continue with an explanation of the left hand side of Eq. 2.8, which related the entropy production in the heat engine with the heat transfer from the surface to the TOA.

The ingoing heat flux J_{in} is a sum of the greenhouse longwave absorption, surface sensible heat flux and dissipation by friction D, which equals power generation P. The expression for the outgoing heat flux J_{out} is inferred from Eq. 2.2. Thus, we obtain a detailed entropy production equation:

$$\frac{H + P + (\frac{3}{4}\tau - 1)R_{L,atm}}{T_S} - \frac{H + \lambda E + (\frac{3}{4}\tau - 1)R_{L,atm} - H_a}{T_A} = \frac{H_a - \lambda E}{< \theta_b >} \tag{2.14}$$

In order to avoid an underdetermined system of equations, we assume that the bulk temperature of the boundary layer approximately equals surface temperature $< \theta_b > \approx T_s$, a valid assumption in a convective boundary layer model (Stull, p.442, 1988). Validity of the latter assumption was addressed in the evaluation of the framework using field station data, obtaining an average difference in the temperatures $\overline{< \theta_b > - T_S} = 3.4°C$. This justifies our approximation as we only underestimates the bulk temperature on the order of 1 %. After a rearrangement of the terms (Eq. 2.14), where we put all the terms except for P on the right-hand side of the Eq. 2.14, we get a simple expression for the atmospheric power generation P, with a fairly straightforward interpretation (Eq. 2.15).

$$P = \frac{H + \lambda E - H_a + (\frac{3}{4}\tau - 1)R_{L,atm}}{T_A} \cdot (T_S - T_A) \tag{2.15}$$

Power generation is primarily driven by the ingoing heat fluxes from the surface and the absorbed longwave radiation from the surface. The EBL heat storage H_a acts as a buffer that takes away a part of available heat during the daytime when H_a is positive, thus decreasing the power generation and releases it into the system in the night when the term is negative, thus sustaining the power generation of the system. The power generation is also proportional to the temperature difference between the surface and atmosphere, consistently with the Carnot heat engine model, in which the temperature difference determines the power generation efficiency (Schmiedl and Seifert, 2008).

2.1.5 Derivation of the MPP Limit

Having obtained the power expression (Eq. 2.15), we can proceed with the derivation of the maximum power limit. The limit of the framework, including soil and vegetation modules can only be solved numerically because of a non-linearity in the latent heat flux parametrization (Eq. 2.38). For that reason, an analytical solution of the limit is presented, using a representative conceptual control model. In the control model the parametrization of the latent heat flux is linear, which makes it possible to analytically solve the system of equations, thus enabling us a clearer interpretation of the framework's results. Sensible and latent heat fluxes in the control model are initially aggregated in one term called the surface turbulent heat flux: $J = H + \lambda E$. Hence, the MPP limit takes a slightly different form (Eq. 2.16).

$$P = \frac{J - H_a + (\frac{3}{4}\tau - 1)R_{L,atm}}{T_A} \cdot (T_S - T_A) \tag{2.16}$$

We have obtained an expression for the power generation that is dependent on the energy fluxes in the EBL and the surface-atmosphere temperature difference. In the following step we will look for the maximum of the expression, which is an ultimate constrain in our system. The formulation presented in Eq. 2.16 does not allow the maximization yet, because the functional form on the right side consists of two interdependent processes, namely the temperature difference $T_S - T_A$ and the turbulent heat fluxes. Fortunately we can rewrite the temperature difference as a function of external forcings to the system (R_s & Q_g) by a use of the surface energy balance equation (Eq. 2.1). In order to do so, we linearize the net radiation at the surface by transforming it to a form, where radiation is proportional to the temperature difference $R_{net} = R_{L,surf} - \frac{3}{4}\tau R_{L,atm} \approx (T_S - T_A)$. Firstly, the Stefan-Boltzmann law is used to calculate the longwave radiation components (Eqs. 2.17 and 2.18). The surface outgoing longwave component $R_{L,surf}$ is linearized, using the Taylor expansion around the average diurnal surface temperature T_0 (Eq. 2.18). A radiative exchange parameter kr that equals the value of a first derivative of the $R_{L,surf}$ at the average surface temperature is introduced to linearize the net radiative exchange (Eqs. 2.19). In the following step, we rewrite the net radiation at the surface (Eq. 2.20). As we can see, the linearization around the average temperature does not bring us to the desired functional form yet. For that reason, we introduce the net radiation constant $R_{L,0}$ (Kleidon, 2015) (Eq. 2.21), which finally allows us to write the net surface radiation as a function of the temperature difference (Eq. 2.22).

$$R_{L,atm} = \sigma T_a^4 \tag{2.17}$$

$$R_{L,surf} = \sigma T_s^4 \approx \sigma T_0^4 + 4T_0^3(T_S - T_0) \tag{2.18}$$

$$kr = 4\sigma T_0^3 \tag{2.19}$$

$$R_{L,surf} - \frac{3}{4}\tau R_{L,atm} = \sigma T_0^4 + kr \cdot (T_S - T_0) - \frac{3}{4}\tau\sigma T_A^4 \tag{2.20}$$

$$R_{L,0} = \sigma T_0^4 - 4\sigma T_0^3(T_0 - T_A) - \frac{3}{4}\tau\sigma T_A^4 \tag{2.21}$$

$$R_{net} = R_{L,surf} - \frac{3}{4}\tau R_{L,atm} = R_{L,0} + kr \cdot (T_S - T_A) \tag{2.22}$$

A linearized net longwave radiation balance at the surface enables us to factor out the temperature difference in the surface energy balance, after inserting the expression forR_{net} Eq. 2.22 in Eq. 2.1:

$$(T_S - T_A) = \frac{(1 - \varphi)R_s - Q_g - J - R_{L,0}}{kr} \tag{2.23}$$

By inserting the later equation into Eq. 2.16 the power generation can be rewritten as a function of the surface energy balance (Eq. 2.24).

$$P = \frac{(J - H_a + (\frac{3}{4}\tau - 1)R_{L,atm}) \cdot ((1-\varphi)R_s - Q_g - J - R_{L,0})}{kr \cdot T_A} \tag{2.24}$$

A basic calculus rule states that for a function to have a maximum, the first derivative of the function must equal zero, whereas the second derivative must be negative. We solve the expression for the first derivative over J, as we are interested in the maximum power generation with respect to the surface turbulence fluxes, knowing that other variables are independent of J (Kleidon and Renner, 2013). The first derivative, given by Eq 2.25, is then used to obtain the optimum surface turbulent fluxes, corresponding to the maximum power generation of the atmospheric heat engine (Eq. 2.26). In the case of the complete model, the turbulent fluxes are partitioned into the latent and sensible component $H \,\&\, \lambda E$. In the model, the power generation is numerically derived with respect to the vertical exchange velocity w, which regulates the convection interdependently with the temperature difference (Eqs. 2.28 and 2.29).

$$\frac{dP}{dJ} = \frac{-2J + (1-\varphi)R_s - Q_g - R_{L,0} + H_a - (\frac{3}{4}\tau - 1)R_{L,atm}}{kr \cdot T_A} = 0 \tag{2.25}$$

$$J_{opt} = \frac{(1-\varphi)R_s - Q_g - R_{L,0} + H_a - (\frac{3}{4}\tau - 1)R_{L,atm}}{2} \tag{2.26}$$

Evidently, the optimum surface turbulent flux is powered by a half of available surface solar radiation, half of boundary layer heat storage and soil heat flux and a half of the longwave radiation terms $-R_{L,0} - (\frac{3}{4}\tau - 1)R_{L,atm}$. A brief back of the envelope calculation of the radiation terms shows that their contribution to the optimum turbulent flux is positive under the expected values of the T_A. With Eqs.: 2.1, 2.2, 2.4, 2.7 and 2.26 we have obtained a closed set of equations that determine the stete of the atmospheric heat engine at its maximum power limit. More importantly, the framework now makes it possible to model the crucial processes and variables of the surface-atmosphere energy balance and heat transfer (J, P, H_a, T_S, J_{out}), requiring only a limited set of external forcing data: the soil heat flux and the absorbed solar radiation at the surface ($Q_g \,\&\, R_s$) and some model parameters. The simplicity of the this energy equilibrium framework in reflected in the fact that the derived expressions determine the state of the atmospheric heat engine and the dynamics of its energetic processes independently of the previous states of the system. In order to calculate the energetic process in the system, we do not need to solve the temporal differential equations. Instead, the temporal evolution of the state is determined by the current state of the forcing variables and a slow transient response of the storage and longwave radiation terms. Of course the simplicity of the framework implies certain limitations, which will be thoroughly examined in the discussion chapter.

2.2 Surface Turbulent Heat Fluxes Parametrization

Surface turbulent heat fluxes in global circulation models and numerical models for weather prediction are usually parametrized using bulk transfer relations, based on the Monin-Obukhov similarity theory (Eq. 2.27).

$$H = c_p \rho \frac{1}{r_{aH}} (\theta_S - \theta) \quad \lambda E_0 = \lambda \rho \frac{1}{r_{aV}} (q_S - q) \tag{2.27}$$

The theory postulates that both sensible and latent heat fluxes are driven by vertical gradients of potential temperature and specific humidity near surface (Eq. 2.27) (Garratt, p.39, 1992). On the other hand, the magnitude of the fluxes is limited by the aerodynamic resistance r_a, which is used to capture the properties of atmospheric stability and surface roughness that inhibit or facilitate the fluxes (Garratt, p.55, 1992). Experimental theory suggests that $r_{aH} = r_{aV}$, when surface sources of heat and vapor are coincident, which is true for the bare surface (Garratt, p.54, 1992). Such parametrization is not directly applicable to our model with its course vertical resolution of only three reservoirs. Therefore, uniformity of the sensible and latent heat fluxes between the surface and the EBL is assumed. Moreover, the driving force of the fluxes is a difference in ambient temperatures of the surface T_S and top of the energetic boundary layer T_{TBL}. In that way, we implicitly assume a linear temperature profile in the atmosphere. A more adequate alternative would be to model vertical potential temperature profile and vertically varying heat fluxes. Yet, the proposed solution is unfeasible to be applied in the three reservoir framework, where vertical temperature profile can only be determined with the three reservoir temperatures. After linearizing specific humidity and, additionally, assuming saturated air at the top of the boundary layer reservoir (Kleidon et al., 2014), we obtain the following parametrization for the sensible and latent heat fluxes:

$$H = \rho c_p w \cdot (T_S - T_{TBL}) \tag{2.28}$$

$$\lambda E_0 = \lambda \rho w \cdot f_w \cdot (q_S - q_{TBL}) \approx c_p (\rho w) \cdot \frac{f_w s}{\gamma} \cdot (T_S - T_{TBL}) \tag{2.29}$$

where w is a vertical exchange coefficient, f_w is a water availability parameter, which expresses the role of soil moisture availability in bare soil evaporation with a value in the range: 0-1, and s saturation vapor pressure curve (Kleidon and Renner, 2013). This parametrization yields adequate partitioning at times when large convective motions take place, i.e., when a convective boundary layer is observed (Garratt, p.58, 1992). One should keep in mind though that in principle the surface turbulent heat fluxes are not determined by a difference between the surface and top of the boundary layer temperatures, but rather by temperature differences near surface. Therefore, the modelled fluxes are expected to be particularly inaccurate on shorter time scales and cannot be used in certain developments of the boundary layer, such as temperature inversion near surface. Parameterizations

used in Eqs. 2.28 and 2.29 are thus a simplification, which averages out the temperature gradients within boundary layer, inherent to the application of the simple reservoir models.

2.3 Soil and Vegetation Modules

Land-atmosphere exchange processes are largely dependent on the characteristics of the surface. For that purpose, we have designed the soil and vegetation modules, which are coupled to the atmospheric heat engine model. The soil module is used to model the soil heat flux, used in the surface energy balance equation (Eq. 2.1). It is also playing a role of a moisture reservoir, which provides vegetation or bare soil with water, available for evapotranspiration. The vegetation module also exhibits a twofold functionality. First of all, vegetation canopy acts as an intermediate water reservoir for evaporation on its own. Secondly, it utilizes a simple ecosystem stomatal resistance model (Garratt, p.235, 1992), (IFS Model cycle - Cy40r1, 2013) that mimics the vegetation's property of regulating moisture release into the atmosphere. In this section each module is only briefly summarized. For a more detailed description of the modules and their analysis, we refer to Appendix A.

2.3.1 Soil Heat Flux

The soil is assumed to be isotropically homogeneous in its conductive properties but not in soil temperature T_{soil}. That is why the soil is partitioned in 4 layers of some characteristic layer depth. A layer depth of 6 cm is proposed because temperature variations at the depths higher than 25 cm are negligible on diurnal time scales (Garratt, p.117, 1992). The role of radiation and convection in the soil can be neglected (De Vries, 1975). Fourier's law for heat conduction characterizes the heat flux between two layers, where k_s is thermal conductivity (Garratt, p.117, 1992):

$$Q_g = -k_s \frac{\partial T_{soil}}{\partial z} \tag{2.30}$$

As one can infer from from Eq. 2.30, the soil heat flux Q_g depends on the soil temperature gradient and conductive properties of the soil, reflected by its thermal conductivity. The latter is a function of soil heat capacity, soil density and soil diffusivity (Farouki, 1986) according to (Eq. 2.31). Soil density ρ_s, specific soil heat capacity c_s and thermal diffusivity κ_s are besides being characteristic for individual soil types also functions of the moisture content in the soil θ_i (Farouki, 1986). Surface temperature and moisture storage W_i can therefore be considered as the only forcing terms of the soil heat flux.

$$k_s = \rho_s \cdot c_s \cdot \kappa_s \tag{2.31}$$

Temperature change in an individual soil layer is determined by the difference between the incoming and outgoing soil heat flux. An implicit Euler method is applied for solving the four layer system with differential equations (Eq. 2.32).

$$\frac{\partial Q_g}{\partial z} = \rho_s \cdot c_s \cdot \frac{\partial T_{soil}}{\partial t} \tag{2.32}$$

2.3.2 Soil Moisture

Soil moisture storage is a vital component of the water cycle that is necessary to determine the thermally conductive properties of a soil. Moreover, the moisture storage is also indirectly related to the potential evaporation at the surface, which is our model parameterized with the water availability parameter f_w. A modified implementation of a bucket model by Manabe (1969) was used to calculate the moisture storage and water availability. As the name speaks for itself, the bucket model quantifies moisture in the soil in terms of the water level in the bucket. Maximum water level is specified by the respective soil's saturation value and depth of the soil profile. The problem of a single bucket model is that weaker precipitation events usually only slightly alters the relative saturation in the bucket whereas in reality the top of the soil gets considerably saturated (Garratt, p.231, 1992). Consequently, a single bucket model response to precipitation or drainage is very slow. Due to the long residence times of the single buckets these models do not adequately deal with moisture changes on diurnal scales. Therefore, the soil was differentiated into three buckets, interconnected by the groundwater flow. The depth of the buckets was determined by the thickness of the respective soil horizon/layer and its moisture saturation value: $W_{max} = dz \cdot \theta_{sat}$.

2.3.2.1 Water Balance Equations in the Soil

Moisture content W is a measure of the total water column that resides in each soil profile. It is related to the degree of saturation, a variable that tells us what proportion of the soil is being occupied by water (De Vries, 1975). The degree of saturation is defined as:

$$\theta_i = \frac{W_i}{W_{max,i}} \cdot \theta_{sat,i} \tag{2.33}$$

Here $W_{max,i}$ characterizes the maximum water capacity of the layer i. When more water is added to the soil that would result in an enhanced runoff, which would remove the additional moisture over time. $\theta_{sat,i}$ approximately equals the fractional proportion of pores in layer i, which have a potential to be filled up with water (IFS Model cycle - Cy40r1, 2013). Moisture contents of the three buckets are determined with a system of interconnected continuity equations (IFS Model cycle - Cy40r1, 2013). A change in the moisture storage for the surface bucket (bucket number one) is calculated as a sum of four processes: throughfall, which stands for the precipitation that penetrates the canopy Th and can also be called as vegetation runoff, root extraction $root_i \cdot E(t)$ and groundwater flow F_{g1} (Eq. 2.34).

$$W_1(t+\Delta t) = W_1(t) - [root_1 \cdot E(t) + F_{g1}(W_1(t)) - Th(t+\Delta t)] \cdot \Delta t \tag{2.34}$$

For buckets two and three, the flow is only determined by a sum of groundwater flows and root extraction. Root extraction describes moisture extraction by the vegetation in an individual layer. In ecological models the term is better known as the sap flow (Garratt, p.240, 1992).

$$W_i(t+\Delta t) = W_i(t) - [root_i \cdot E(t) + F_{gi-1}(W_{i-1}(t)) - F_{gi}(W_i(t))] \cdot \Delta t \tag{2.35}$$

Throughfall is an input variable, whereas evapotranspiration is among the outputs of the model from the previous time step $E(t)$.

2.3.2.2 Water Availability

The parameter that relates bare soil evaporation at the surface with moisture storage is water availability f_w (Kleidon et al., 2014). Water availability, with its value ranging from 0 to 1, depends on the specific humidity gradient between the surface and top of EBL $q_{sat}(T_S) - q_{sat}(T_{TBL})$. Specific humidity varies as a function of both temperature and relative humidity at the surface for bare soil (Eq. 2.36). The expression was derived by equating the model parameterization of the bare soil latent heat flux (Eq. 2.29) with the "Monin-Obukhov parameterization" (Eq. 2.27).

$$f_w = \frac{r_h \cdot q_{sat}(T_S) - q_{sat}(T_{TBL})}{q_{sat}(T_S) - q_{sat}(T_{TBL})} \tag{2.36}$$

2.3.3 Vegetation

The evaporation flux presented in Eq. 2.23 is only valid in the cases of a bare soil surface. However, the observations used in the model analysis have been conducted over a densely vegetated surface. That calls for a different parameterization of the surface evaporation flux the one that captures the distinct evapotranspirative properties of a forest ecosystem. Water is an elementary physiological need for trees, which is why vegetation does not evaporate as "indifferently" as a bare soil (Garratt, p. 132, 1992). One can imagine plants as water retention reservoirs coupled with soil that tend to regulate moisture transfer in a way that optimizes their gross primary production. As a result, evapotranspiration from dry vegetation can be considerably smaller than the evaporation from a bare soil, as it not only depends on water availability in the soil, but also on other ambient conditions such as temperature, nutrients concentration and the incoming short wave radiation amongst others (Farquhar et al., 1980). This calls for an additional extension of the soil module. Still, it is desirable to keep the model as simple as possible, which is why a simplistic isothermal canopy vegetation model was implemented. In this

model we account for a decrease in evaporation by introducing stomatal resistance r_c, a variable that represents opening of the stomata in the foliage, which facilitates moisture exchange through the leaves (Garratt, p.236, 1992). Evapotranspiration of dry vegetated area is therefore parametrized as (Garratt, p.236, 1992):

$$E_v = \rho \frac{s}{\gamma(r_{aV} + r_c)} \cdot (T_S - T_{TBL}) \tag{2.37}$$

A detailed description of the vegetation module is not essential to our research and is therefore omitted from the report. A brief complementary explanation on the Jarvis model can be found in Appendix A.

2.3.3.1 Extension of the Surface-Water Balance

Vegetation significantly alters the surface water balance, especially when it has a thick canopy. The canopy's foliage acts as an interception reservoir, which is why the throughfall in vegetated areas usually does not equal precipitation (Ilvesniemi et al., 2010). This requires an introduction of an additional vegetation canopy water reservoir in the model (Eq. 2.34). The water balance in the canopy reservoir was adapted from Garratt, (p.237, 1992) and is a function of precipitation $Prec$, which increases the water content of the canopy, and the sinks: throughfall Th (vegetation canopy runoff) and evapotranspiration E_v, which deplete the reservoir. A maximum canopy water storage m is deemed proportional to the canopy leaf area, characterized with the dimensionless leaf area index LAI (Garratt, p.237, 1992):

$$m \approx 0.2 \cdot LAI \tag{2.38}$$

$$W_{veg}(t + \Delta t) = W_{veg}(t) + [Prec(t + \Delta t) - E(t) - Th(t)] \cdot \Delta t \tag{2.39}$$

Vegetation canopy runoff Th equals zero when $W_{veg} < m$, whereas it equals precipitation $Prec$ when $W_{veg} \geq m$. At times when the canopy reservoir is at its maximum capacity, the vegetation evaporates as a bare soil E_0. When there is no moisture on foliage, canopy evaporates as a dry vegetation E_v. Finally, in the intermediate regime the evapotranspiration is parameterized as a linear combination of both boundary condition regimes. To sum up, we present evapotranspiration for all the wetness regimes of the canopy (Eq. 2.40).

$$E = \begin{cases} E_v & ; m = 0 \quad dry\,canopy \\ \left[\frac{W_{veg}}{m} \cdot E_0 + (1 - \frac{W_{veg}}{m}) \cdot E_v\right]; & 0 < W_{veg} < m \quad partially\,dry\,canopy \\ E_0 & ; W_{veg} \geq m \quad wet\,canopy \end{cases} \tag{2.40}$$

So far we have only presented the parameterizations for evaporation over a bare soil surface and evapotranspiration over a vegetation. Usually though, evapotranspiration

includes contributions from the vegetation as well as the soil. A convenient solution is to present the total evapotranspirative flux as a linear combination of both partial terms (Eq. 2.41). For example, if the modelling site is partially covered with vegetation (C_{veg}) and partly with bare soil, the aggregate evapotranspiration is calculated as:

$$E = (1 - C_{veg}) \cdot E_0 + C_{veg} \cdot E_v \tag{2.41}$$

2.4 Schematic Representation of the Model

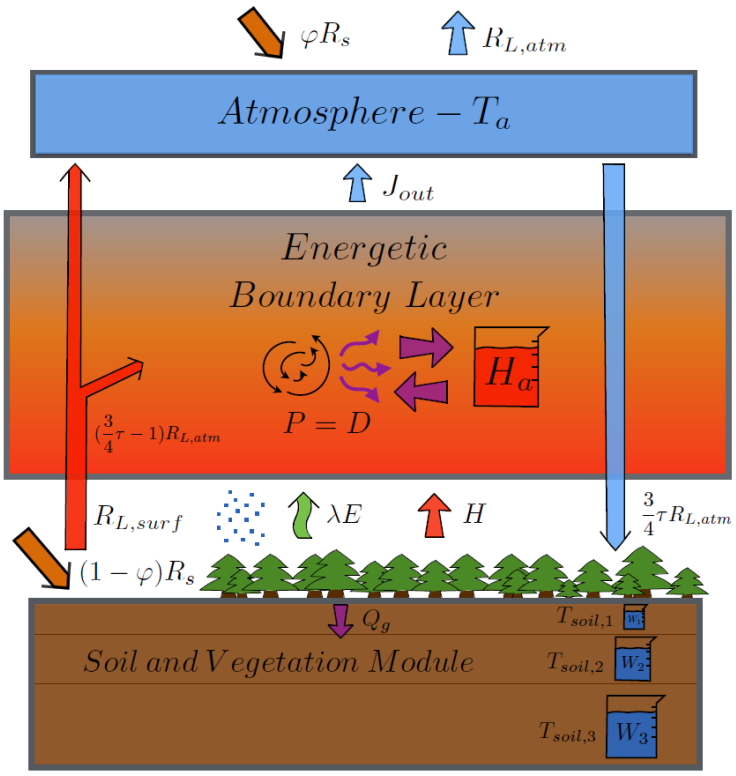

Figure 2.2: A complete scheme of the modelling framework illustrates all the key processes in the system. It shows a three layer soil moisture module with a set of three interconnected buckets. On top of the soil module lies the vegetation module which regulates stomatal resistance of the forest, thus affecting the magnitude of the surface the latent heat fluxes. The scheme also illustrates the framework's energy fluxes, the EBL heat storage and energy balances of the reservoirs. The atmospheric heat engine in the EBL is portrayed next to the heat storage bucket in the form of convective motions that are being dissipated near the surface.

Chapter 3

Methodology

The primary objective of our study, the modelling of the vertical turbulent heat transport, was conducted with a model study of atmospheric thermodynamics. The modelling was conducted in several stages. After finalizing the outline of the theoretical framework, which was presented in the previous chapter, a representative conceptual model of the convective and radiative atmospheric heat engine was constructed. The conceptual model, which incorporated the energy balance in the atmospheric column, but lacked the dynamic coupling with soil and vegetation, was designed with the intention to qualitatively demonstrate the ability of the framework to simulate the observed diurnal dynamics of the system. Upon a successful simulation of the diurnal dynamics with the conceptual model, we added individually tested soil and vegetation modules, thus obtaining the operating model that interactively coupled the atmospheric heat engine with the surface. The model experiments were performed in relation to the research questions presented in the introduction. The bulk of the runs was performed with intention to validate the MPP hypotheses and prove that the alternative approach has a practical potential. Finally, a local sensitivity analysis of the model was performed to test the robustness and reliability of the model and also to provide an additional climatological insight in the modelled system. Accordingly, the sensitivity analysis was designed in the form of the global warming experiments.

3.1 Application of the Conceptual Model

The conceptual model was designed in order to test, whether the energy balance framework with the MPP constraint, can reproduce the diurnal characteristics of the energy fluxes and vertical exchange velocity in the atmospheric column. Additionally, the surface temperature was simulated as a control test. Climatological site that was chosen for the control model analysis was Barstow, California, a semi-arid location with plentiful of insolation and scarce vegetation cover. With 11 mm of average precipitation in July, the water availability is presumably very low (NCDC, 2015). A weak greenhouse effect

was prescribed with the greenhouse forcing parameter of $\tau = 1.5$ due to a presumed low vapor density in the atmosphere. A theoretical absorbed solar radiation signal R_s was generated, assuming the albedo of the desert ~ 0.35 and calculating sun movement at the site for the 15th of July (Henderson-Sellers and Wilson, 1983). As a semi-arid area, Barstow was assumed to be a relatively cloudless region. Therefore, we assumed that only 10% of the total absorbed solar radiation is absorbed in the atmosphere. An idealized diurnal surface temperature signal which was based on the daily average, maximum and the minimum temperature at the site for July was generated. That data was obtained from the National Climatic Data Center archive (NCDC, 2015). The temperature signal was used to calculate the soil heat flux at the surface Q_g by using the Fourier equation (Eq. 2.30). The water availability parameter f_w was prescribed as a linear function with a weakly negative slope (educated guess), ranging from 0.12 at sunrise to 0.08 at sunset, the values that are characteristic for a very dry soil. A comparison of the modelled temperature output to the generated temperature signal was used in combination with the surface energy balance closure as an independent verification of the framework. The energy fluxes in the column were only qualitatively assessed.

3.2 Observations

A set ob observation data has a twofold significance for the research. First of all, a number of observation data is used in the form of input variables in the model and secondly, some observation variables (H, E, T_S) serve as the comparison data for the modelled output. Hence, the observations played a key role in all the modelling processes: initialization, model runs, verification and analysis. We used measurements from Hyytiälä Forestry SMEAR-II station (Station for Measuring Ecosystem-Atmosphere Relations) with a temporal resolution of 30 minutes. The data is freely accessible online (AVAA database, 2014). Additionally, we have used high-resolution radiosonde data which were released from the station site as a part of the HUMPPA/COPEC field campaign (Ouwersloot et al., 2012). All the data was collected from 13/07/2010 to 10/08/2010. The main reason for a relatively narrow time frame and a selection of only one observation site is rarity of high-resolution radiosonde data. At least four daily radiosonde measurements were required for an approximate calculation of the EBL heat storage H_a, while the standard synoptic stations only provide up to two radiosonde releases per day. The data handling and application in the model is further described in the following subsections. A complete list of the observation variables can be found in the tables of variables and parameters (Appendix C).

3.2.1 Hyytiälä Forestry Field Station Data

3.2.1.1 Soil and Vegetation Module

Soil and Vegetation modules were individually tested and compared with the observations from the Hyytiälä field station. The following variables were used in the analysis: precipitation $Prec$, evapotranspiration E, soil moisture θ, soil heat flux Q_g and the temperature at 4.4m T_S. The soil was classified as Haplic podzol, a common soil type in Scandinavia. As a consequence, we applied the corresponding sandy loam empirical parameters in the soil module (Ilvesniemi et al., 2010; Greve et al., 1998; Clapp and Hornberger, 1978). Estimates of evapotranspiration were obtained from the eddy-covariance measurements. The latent and sensible turbulent fluxes were measured approximately 23 m above ground, which is about 10 m above the canopy (Ilvesniemi et al., 2010; Description of the SMEAR II Station, 2014). In order to avoid numerical errors, the precipitation was temporally down-scaled to the intervals of 30 seconds using uniform distribution. Vertical root distribution $root$ was adapted from the specified values for evergreen needleleaf trees biome in the IFS Model cycle - Cy40r1 (2013). The seven-layer soil profile from the observations was aggregated into three layers, corresponding with the number of buckets in the model. Near surface temperature observations ($T_{4.4m}$) were used to calculate the soil heat flux and temperature of each soil profile. Soil heat flux observations were then used to calibrate the conductivity and specific heat capacity of the soil. It was assumed that 70% of the evapotranspiration flux is provided by vegetation, and the residual is accounted as bare-soil evaporation, which was inferred from satellite images of the observation site (Description of the SMEAR II Station, 2014).

3.2.1.2 Solar Radiation Forcing

The proportion of solar radiation that is absorbed at the surface $(1-\varphi)R_s$ was inferred from the global radiation measurements taken 16 m above the surface. The observations were corrected with an albedo of the pine forest $(1-\alpha) = 0.93$ (Betts and Ball, 1997). An educated guess was made for the incoming solar radiation absorbed at top of the atmosphere φR_s. We started with an assumption that 20% of the total incident solar radiation R_{tot} is absorbed by clouds and atmosphere, which is supported in the global energy balance schemes (Lacis and Hansen, 1974; Trenberth et al., 2009; Ramanathan and Vogelmann, 1997). It is also suggested that approximately 20% of the total incident solar radiation is reflected at the top of the atmosphere (Ramanathan and Vogelmann, 1997) (Eq. 3.1). From these assumptions, which are demonstrated with Eqs. 3.1 and 3.2, the parameter value $\varphi = 0.26$ was inferred.

$$(1-\varphi)R_s = 0.6 \cdot (1-\alpha)R_{tot} \tag{3.1}$$

$$\varphi R_s = 0.2R_{tot} \tag{3.2}$$

3.2.1.3 The Greenhouse Effect

The greenhouse enhancement in the model was represented by a constant optical depth parameter τ. The parameter was calculated from an averaged observed incoming longwave radiation at the surface $\overline{L}\downarrow$ and the average outgoing longwave radiation $\overline{R_a}$ at Hyytiälä (Eq. 3.3).

$$\frac{3}{4}\tau \cdot \overline{R}_{L,atm} = \overline{L}_{\downarrow} \tag{3.3}$$

3.2.1.4 Surface Turbulent Heat Fluxes

Surface turbulent heat fluxes H, λE were measured with the eddy-covariance instruments (EC) positioned slightly above the canopy. Both H and λE data sets were subjected to filtering, which eliminated the corrupted data and the measurements collected at times of temperature inversion (a noticeable negative sensible heat flux), because the model cannot reproduce these situations.

3.2.2 Calculation of the Energetic Boundary Layer Heat Storage

The heat storage term H_a is primarily increased by both surface turbulent heat fluxes (Eq. 2.2). In order to calculate the heat storage contributions from both turbulent heat fluxes, we separated the term in two parts, the sensible Ha_{SH} and the latent heat storage Ha_{LH}. Sensible heat storage was defined as a transient change of the EBL internal energy $Q_{SH} = \rho_{dry} \cdot c_p \cdot T \cdot z$ in the vertical over time (Eq. 3.4). By assuming a hydrostatic equilibrium, which is a standard assumption in the atmospheric modelling science: $\frac{\partial p}{\partial z} = -\rho_{dry} \cdot g$ (Stull, p. 84, 1988), we replaced the atmospheric height coordinates z with pressure coordinates p (Eq. 3.4). The internal energy can be imagined as as an integral of temperature with respect to height, multiplied by the specific heat capacity of the energetic boundary layer (Fig. 3.1).

$$Ha_{SH} = \frac{dQ_{SH}}{dt} = -\frac{c_p}{g}(dp \cdot \frac{\partial T}{\partial t}) - \frac{c_p}{g}(T \cdot \frac{\partial p}{\partial t}) \tag{3.4}$$

The first part of Eq. 3.4 represents local heating in the atmosphere, while the second one stands for pressure tendency, which represents the contribution of the column's vertical expansion or compression, thus regulating quantity of the dry air in the column. A brief back of the envelope analysis has shown that the second term tends to dominate the sensible heat storage when there is a slight temporal pressure change at the surface ($\sim 0.1\,hPa$). The pressure tendency is strongly dominated by synoptic changes, which are independent of the local surface heating. Synoptic weather developments can therefore introduce considerable noise in the Ha_{SH}. In order to solve this problem, we have introduced a cutoff pressure thickness Δp, hence imposing a fixed thickness of the EBL column. By using the cutoff pressure we contain the atmospheric column within a constant pressure difference which partly diminishes the importance of the second term

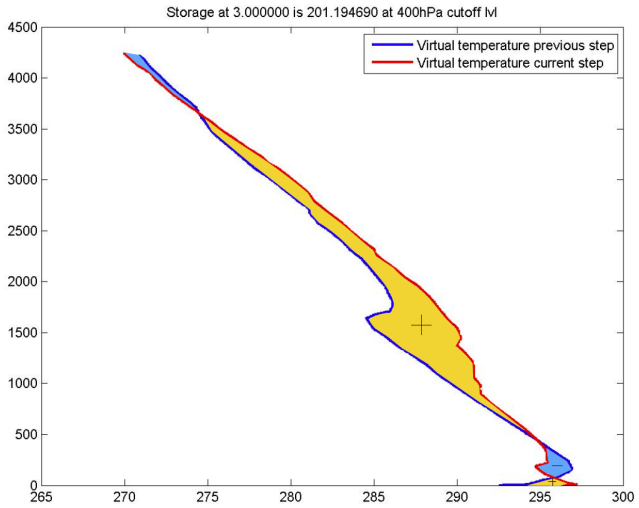

Figure 3.1: Illustration of the EBL sensible heat storage calculation. The figure portrays two vertical temperature profiles at different times. The sensible heat storage Ha_{SH} is a difference in the internal energy of the column over time, which can be calculated as an integral of the vertical temperature over height, divided by the time difference. The difference in the integrals of two vertical temperature profiles is illustrated in the figure as a coloured surface area. A positive contribution to the Ha_{SH} is indicated with an orange colour, whereas the blue reflects a negative contribution to the term.

altogether (Eq. 3.5). This approach was also used for practical reasons. Because the radiosondes do not cover the entire vertical extent of the atmosphere, as they eventually break down, a reference point is needed for an execution of the comparative analysis of the measured profiles. Equation 3.5 shows a numerical summation of the internal energy difference over time up to the cutoff difference of the column Δp:

$$Ha_{SH} = \frac{dQ_{SH}}{dt} = \frac{c_p}{g}\left[\int_{p_s}^{p_s-\Delta p} \dot{T}(p,t)\cdot dp\right]$$
$$= \frac{c_p}{g\cdot\Delta t}\cdot\left[\sum_{i=1}^{n}\frac{T(p_{i+1},t+1)+T(p_i,t+1)}{2}\cdot(p_i-p_{i+1}) - \sum_{i=1}^{n}\frac{T(p_{i+1},t)+T(p_i,t)}{2}\cdot(p_i-p_{i+1})\right] \tag{3.5}$$

The EBL latent heat storage Ha_{LH} is a measure of changes in the moisture content in the EBL (Eq. 3.6). By assuming a hydrostatic equilibrium and an ideal gas law for water vapor $e = \rho_v R_v T$ and dry air $p = \rho_{dry} R_{dry} T$ (Stull, p. 81, 1988), Eq. 3.6 can be rewritten to a more convenient form without the vertically varying densities of water vapor ρ_v and dry air ρ_{dry} (Eq. 3.7). The term was then calculated as a vertical summation of the water vapor pressure e multiplied by the heat capacity constants (Eq. 3.8).

$$Q_{LH} = \lambda \rho_v dz \tag{3.6}$$

$$Q_{LH} = -\frac{\lambda \cdot e \cdot R_{dry} \cdot dp}{g \cdot R_v \cdot p} \tag{3.7}$$

$$\begin{aligned} Ha_{LH} = \frac{dQ_{LH}}{dt} &= \int_{p_s-\Delta p}^{p_s} \frac{\lambda \cdot R_{dry} \cdot \dot{e}}{g \cdot R_v \cdot p} dp \\ &= \frac{\lambda \cdot R_{dry}}{g \cdot R_v \Delta t} \cdot \left[\sum_{i=1}^{n} \frac{e_{i+1}(t+1) + e_i(t+1)}{(p_{i+1} + p_i)} \cdot (p_i - p_{i+1}) - \sum_{i=1}^{n} \frac{e_{i+1}(t) + e_i(t)}{(p_{i+1} + p_i)} \cdot (p_i - p_{i+1}) \right] \end{aligned} \tag{3.8}$$

The heat storage components were calculated from 146 irregular radiosonde measurements released at Hyytiälä. The cutoff thickness of 400 hPa was chosen as the column thickness because of an insignificant diurnal variation of the internal energy and moisture content above that threshold. A maximum time step for an adequate calculation of the total heat storage was determined as six hours. Vertical temperature profiles that were further apart were excluded from the analysis. The calculated total heat storage $H_a = Ha_{LH} + Ha_{SH}$ represents an approximate value of heat, released or stored at the midpoint of a given time interval.

3.2.3 Output Data Analysis

The modeled surface turbulent heat fluxes were paired with the corresponding observation values, thus forming the prime data set for the analysis. Scatter plots were then used to portray the correlations between the observations and the outputs. By comparing Theil-Sew estimator analysis with a simple linear regression, it has been proved that the data is not significantly skewed or homoscedastic which justifies a simple linear regression analysis. The analyzed data set was unevenly distributed with more frequent measurements around noon and less frequent ones in the morning, thus disqualifying the possibility of ensemble averaging. For that reason the data was fitted diurnally. Variable means were obtained from an integral over the diurnal distribution of each respective variable (Eq. 3.9). The averaging was also used to compare the modelled surface energy balance with the averaged measurements.

$$\overline{variable} = \frac{\int_{t_{sunrise}}^{t_{sunset}} fit\,(variable) \cdot dt}{t_{sunset} - t_{sunrise}} \tag{3.9}$$

The modeled EBL heat storage was compared to the calculated storage from the radiosonde data and also to the analytically calculated term (Eq. 2.3), by applying the

same diurnal analysis as for the turbulent fluxes. Besides the aforementioned variables, a less attentive analysis was conducted for the surface temperature T_S, the soil heat flux Q_g and the soil moisture storage θ. Analysis of the latter two variables can be found in the Appendix A.

3.3 Changing Climate Sensitivity Analysis

An explicit representation of the greenhouse effect in the model enables us to design climate change experiments in a relatively straightforward manner. By varying the optical depth τ we change the incoming longwave radiation component (greenhouse enhancement) at the surface, which is a particular example of the one at a time sensitivity analysis, and study the changes of relevant energetic variables. The climate sensitivity parameter Λ characterizes a response of a given variable to the changes of the greenhouse effect (Eq. 3.10).

$$\Delta variable = \Lambda \cdot \Delta \overline{L}_{\downarrow} \tag{3.10}$$

The reference point in the analysis is the current climate optical depth $\tau = 2.036$ which is calculated from an averaged incoming longwave radiation at the surface $\overline{L}_{\downarrow} = 375.6\,\frac{W}{m^2}$ (Eq. 3.3). The parameter was varied within a selected range, corresponding to the nine greenhouse enhancement scenarios:$[\overline{L}_{\downarrow} - 2.8\frac{W}{m^2}, \overline{L}_{\downarrow} + 6.5\frac{W}{m^2}]$, which lower range roughly corresponds to the pre-industrial radiative forcing (Myhre et al., 2013) while the upper range corresponds to the 8.5 RCP (Representative Concentration Pathways) scenario by the IPCC (Moss et al., 2010). This was done with deliberation to compare the sensitivity analysis of our model with the selected climate models. After an execution of the first set of experiments, we have realized that our definition of an enhanced greenhouse effect does not directly relate to the IPCC's definition of the radiative forcing (RF), which defines the RF as: "the change in net downward radiative flux at the tropopause after allowing for stratospheric temperatures to readjust to radiative equilibrium, while holding surface and tropospheric temperatures and state variables such as water vapor and cloud cover fixed at the unperturbed values" (Myhre et al., 2013). Therefore we omit from using the expression radiative forcing in the analysis, but rather characterize the analysis as sensitivity with respect to an enhanced greenhouse radiation at the surface. The sensitivity analysis was conducted on four characteristic variables: mean surface temperature $\overline{T_S}$, convective transport w_*, sensible heat H and latent heat flux λE. Other terms of the surface energy balance equation were also studied. Finally, we should be aware of the limitations of our climate sensitivity analysis. First of all, as it was already explained, the IPCC community executes the climate sensitivity analysis by using different definitions on a change in radiative forcing. Secondly, the diurnal averages in our model were calculated over the July-August measuring period, both being unconventional averaging periods as the climate sensitivities are usually performed with respect to the annual or seasonal averages. Moreover, our sensitivity analysis was performed on a specific land-based observation site. On contrary, a vast majority of climate sensitivity analyses is executed over

large-scale surfaces, therefore their values represent an aggregated sensitivity over various types of land and even the oceans. Thus, we should keep in mind that our research is not necessarily directly comparable with the conventional sensitivity analyses.

Chapter 4

Results

The modelling results are presented in three sections. We first present the results of the conceptual model, which validate the applicability of the framework on the diurnal time scales. We then evaluate a general performance of the complete framework by comparing the diurnally averaged surface energy balance outputs with the corresponding analysis of the observations from Hyytiälä. This is followed by an examination of the partitioning of the surface turbulent fluxes. Diurnal averages are used to identify systematic differences between the observations and the modelled results. Then the potential effects of the horizontal heat advection, assumed as the most considerable systematic disturbance in the model-observation comparison, are explored. In the following subsection we test the concept of the EBL heat storage by comparing the modelled diurnal variation of the term with calculated values from the radiosonde measurements and an analytical calculation of the term from observed solar radiation and the modelled soil heat flux (Eq. 2.3). Afterwards, the framework's potential use for estimating the rates of vertical convective transport is explored. Finally, we perform a sensitivity analysis of the model, which is designed to validate the framework, but also with an intention to provide an insight into the system's response in temperature, partitioning of the surface turbulent fluxes and changes in the rate of evaporation, all under the probable greenhouse enhancement in the 21st century. Sensitivity of the model will be compared with climate sensitivites of the state of the art GCMs. A coherent interpretation of the results and their implications for the validity of the hypotheses will be further developed in the discussion section.

4.1 Conceptual Model

The conceptual model was used to simulate a climatological July day in Barstow, California (Fig. 4.1). Before we look into the results, we should mention an important limitation of the model. Its design inherently limits the applicability of results to daytime when the model correctly projects the heat transfer in the direction from the warmer surface to the colder TOA reservoir. Negative values of the turbulent heat fluxes imply a

heat transfer from the cold to the warm reservoir, which contradicts with the second law of thermodynamics (Eq. 1.1). Gray-shaded segments of the Fig. 4.1, which depict the nonphysical results, are therefore omitted from the analysis. The implicit focus on the diurnal time frame does not mean that the negative values of the surface heat fluxes are negative. In fact, the negative values are plausible in the case of a vertical temperature inversion. However, they are unphysical in our modelling framework, where due to a course vertical resolution the temperature difference that drives the turbulent heat fluxes is always positive.

A symmetry in the forcing functions as well as the outputs, plotted in the upper left of Fig. 4.1 clearly demonstrate a high degree of idealization in the system. This is a consequence of neglecting physical processes such as clouds, horizontal advection of heat and moisture, condensation of moisture, explicit radiative warming and cooling in the EBL and turbulent dissipation. In other words, solar radiation R_S and the soil heat flux Q_g are the only energy inputs in the system. Consequently, the results resemble their diurnal symmetry as well. The outputs must therefore be treated as a rough first order approximation of the typical diurnal cycles in energy fluxes and other terms of the system.

The temperature control experiment, depicted in the upper right of the figure indicates that the model reproduces the net absorbed energy at the surface reasonably well. The modeled temperature amplitude is only slightly exaggerated. A greater inconsistency can be observed in an overestimation of the morning warming and cooling at dawn. The discrepancy can be largely attributed to two factors, 1) an inadequate representation of the surface solar forcing $(1-\varphi)R_s$, which is in reality a more sinusoidal-like function than the dome shaped as depicted in Fig. 4.1, and 2) a disregard of the surface heat capacity, which prolongs the time it takes to warm or cool the surface. The inferred energy fluxes in the column capture the observed diurnal cycle reasonably well (Fig. 4.1, bottom left). Net longwave radiation between surface and atmosphere Rl reflects the temperature differences of the reservoirs. The surface turbulent heat fluxes are within the range expected for a semi-arid location. Due to a relatively low water availability f_w, the sensible heat flux H is dominating. The Bowen ratio $\frac{\lambda E}{H}$ was calculated for a further evaluation of the framework, its values being in accordance with semi-arid surfaces (Garratt, p.36, 1994). Optimum sensible and latent heat fluxes, which are inferred from the maximum power constraint (Eq. 2.20) are strongly dependent on solar radiation whereas the other terms in the equation contribute less energy. The modelled EBL heat storage H_a resembles the characteristics that were illustrated in the introduction. During daytime the heat storage is typically positive, indicating that the EBL is storing a significant amount of energy. Around 6 pm, after solar heating is weakened, the EBL starts to release heat, thus powering the heat engine in the absence of surface turbulent heat fluxes (Eq. 2.26).

Finally, let us look at the vertical exchange velocity w, the driving variable of the surface turbulent fluxes (Eqs. 2.22 and 2.23). The vertical exchange velocity characterizes the dependence of the vertical heat transport on the vertical temperature gradient. As a consequence, the shape of the velocity plot reflects the diurnal evolution of the turbulent fluxes (Fig. 4.1, bottom right). Vertical exchange velocity is a proportionality parameter

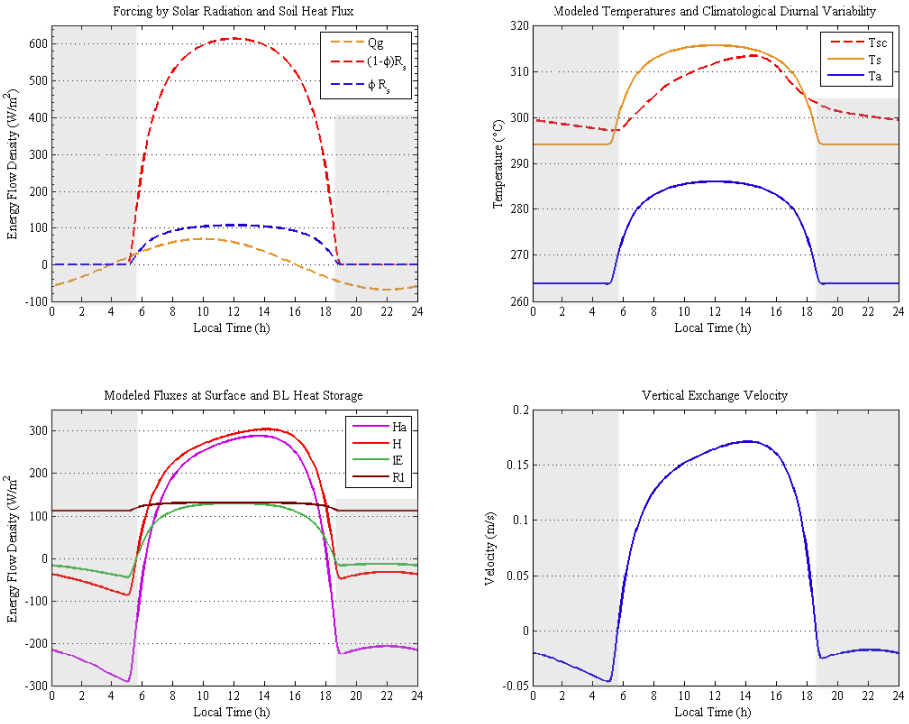

Figure 4.1: The conceptual model outputs. The four figures represent the diurnal-cycle of the conceptual model outputs for a single climatological July day in Barstow, California. Model inputs are shown in the dashed plot-lines, wheareas the outputs are shown in the solid plot-lines. The gray-shaded areas of the figures indicate the non-physical night-time results. The upper left panel depicts the forcing functions in the system: the absorbed radiation components R_s and the modelled soil heat flux Q_g. The upper right part of the figure shows the modelled diurnal surface temperature next to the generated climatological temperature signal and the modelled atmospheric temperature. The bottom left panel shows the selected energy fluxes in the atmospheric column, including both surface turbulent fluxes H & λE, the net radiative exchange at the surface R_l and the EBL heat storage H_a. Finally, the bottom right panel vertical exchange velocity coefficient w, a variable that is related to the intensity of the vertical convective transport.

for vertical transport of heat and moisture. However, this does not mean it can be directly related to the convective velocity w_*, a scaling parameter for vertical turbulent transport in a convective boundary layer (Stull, p.188, 1988), even though both variables share the appropriate units. Nonetheless, these parameters are closely related which is why the modelled vertical exchange transport (Fig. 4.1, bottom right) closely resembles the diurnal dynamics of convection (Eq. 4.3), (Stull, p.118, 1988).

4.2 Radiative and Convective Atmospheric Heat Engine Model

Whereas the conceptual model is only designed to provide a general insight in the energy exchange processes, thus confirming a general physical consistency of the framework's equations, the complete model aims to provide reasonable estimates of the energy fluxes at the selected observation site at any given point of the day. Different objectives of the models are also reflected in their complexity and the properties of the input data. The conceptual model calculations are executed with the generated input data, which were based on the monthly mean climatological values. The complete model on the other hand projects the energy exchange on a basis of the conducted measurements in the system.

4.2.1 Surface Energy Balance

Analysis of the surface energy balance components is a crucial prerequisite in testing the quality of the model. The evaluation was executed by comparing a diurnally averaged energy balance of the model with the averaged observations from Hyytiälä (Fig. 4.2).

A notable overestimation in the model can be observed in the outgoing longwave ($+85.3\,W/m^2$) and incoming longwave ($+63.6\,W/m^2$) components. Thus, the model projects that the surface receives and radiates approximately 20% more than observed in the measurements. This inaccuracy can be attributed to the opaque atmosphere assumption in the framework. Remember that we neglected the existence of an atmospheric window, which reflects the role of a direct longwave radiation release to space. In Trenberth et al., (2009) a global average of the atmospheric window is estimated at $40\,W/m^2$, a value that is comparable to the overestimation in our model. A higher absolute increase in the outgoing longwave compared to the incoming longwave component results in a decrease in the total turbulent fluxes. The sum of turbulent fluxes is therefore underestimated in the model ($-17.7\,W/m^2$), but the more pronounced difference lies in the partitioning of the turbulent fluxes, with the model projecting a higher latent flux compared to the observations, whereas the observations indicate a higher sensible flux. A more detailed comparison of the partitioned heat fluxes will be explained in the next subsection. Also as a consequence of an additional energy input at the surface, the projected mean surface temperature is substantially overestimated ($\Delta\overline{T_s} = 14.8\,K$).

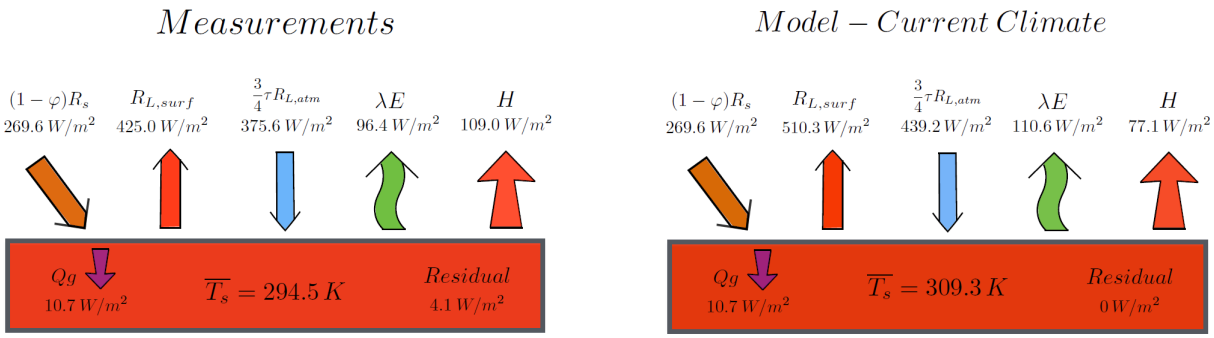

Figure 4.2: Surface energy balance - measurements and the model. The graphics portray the diurnal means of the surface energy balance fluxes and the mean surface temperature $\overline{T_S}$. The left panel scheme portrays the means at the Hyytiälä measuring site, whereas the right panel figure depicts the means from our model. The model clearly overestimates both longwave radiation components $R_{L,surf}$ & $\frac{3}{4}\tau R_{L,atm}$ and the latent heat flux λE, but on the other hand underestimates the surface sensible heat flux H.

4.2.2 Surface Turbulent Heat Fluxes

We present the results of the diurnally averaged fluxes and then evaluate correlations between observations and the outputs. Correlation between the absorbed solar radiation at the surface $(1-\varphi)R_s$ and the turbulent fluxes is also studied.

Figures 4.2b and 4.3b clearly show that the model reproduces the diurnal cycle. There appears to be a time delay (phase shift) in the observations in regard to the model in both figures. The shift is not uniform, as both sensible and latent fluxes peak after 11 am local time. It can be inferred from the figures that the shift is a consequence of a quicker buildup of the modelled surface turbulent fluxes in the morning, as well as their faster decrease in the afternoon compared to the observations. Comparable standard deviations of the monthly averages (box-plots) indicate that the model captures the extent of the intermonthly flux variations reasonably well. The figures also show a noticeable difference in the magnitudes between the observations and the model outputs. Projected latent heat fluxes are higher, whereas the sensible fluxes are lower than in the measurements. That aspect is more clearly demonstrated in the left panels of the figures (Figs. 4.3a and 4.4a), where all 674 model results are shown jointly with the corresponding measured values including a 1:1 line and the linear regression fit. Coefficient of determination for the both components shows linear trends with noticeable scatter $R^2_{\lambda E} \approx 0.57$ and $R^2_H \approx 0.70$. The diurnal averages show a mean underestimation of projected surface sensible heat flux by 29%, whereas the surface latent heat flux comparison shows an average overestimation by 15%.

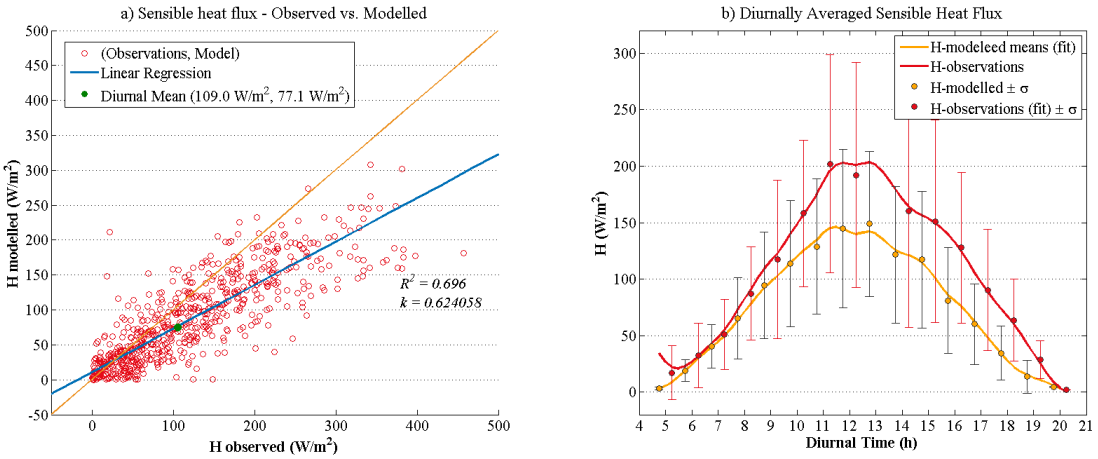

Figure 4.3: Sensible heat flux analysis. A comprehensive comparative analysis of the sensible heat fluxes in the model and at the observation site. a) depicts all the 674 model runs, which are paired with the corresponding observed values at the site (H_{obs}, $H_{modelled}$). The scatter plot and the linear regression fit are portrayed next to a 1:1 (orange) line, to point out the difference between the observations and the modelled values. b) shows an average diurnal cycle of the observed (red) and modelled (orange) sensible heat flux. The box plots show standard deviations of the modelled and measured values at a given diurnal time.

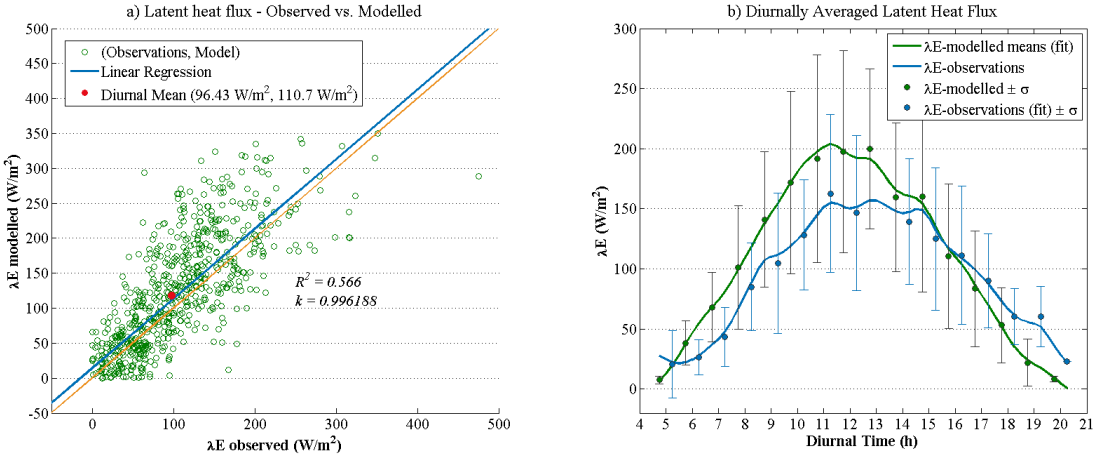

Figure 4.4: Latent heat flux model analysis. A comprehensive comparative analysis of the latent heat fluxes in the model and at the observation site. a) shows all the 674 model runs, which are paired with the corresponding observed values at the site (λE_{obs}, $\lambda E_{modelled}$). The scatter plot and the linear regression fit are portrayed next to a 1:1 (orange) line, to point out the difference between the observations and the modelled values. b) depicts an average diurnal cycle of the observed (blue) and modelled (green) latent heat flux. The box plots show standard deviations of the modelled and measured values at a given diurnal time. An observed shift between the observation and the model plot suggests a premature morning buildup and an afternoon breakdown of the temperature gradients in the model.

4.2.2.1 H and λE Dependence on R_S

The derivation of the optimum surface turbulent heat flux indicates a strong correlation with the surface solar radiation, since half of the radiation is used to directly power the turbulent fluxes in the heat engine (Eq. 2.20). Figures 4.4a and 4.4b show the diurnal evolution of the turbulent heat fluxes as a function of radiation, thus confirming a strong interdependence with a correlation coefficient of $r = 0.88$ for the modelled fluxes and $r = 0.80$ for the observations. Yet, a closer inspection of the figures points out a clear distinction between the observed and modelled values including a hysteresis in the diurnal cycle of the fluxes. The hysteresis is clearly visible in the measurements (Fig. 4.5b), where we can observe morning fluxes occurring at higher solar radiation values compared to the the afternoon values. That points that there needs to be stronger radiation in the morning, in order to initialize the temperature and moisture gradients, which drive the turbulent fluxes, than to sustain the gradients in the afternoon. The model fails to reproduce the hysteresis as it actually makes a contrary projection with an unpronounced reverse hysteresis i.e., there needs to be a slightly stronger radiation in the afternoon to sustain the turbulent fluxes. This tendency was already observed in the diurnally averaged turbulent heat fluxes where the morning fluxes are overestimated and the afternoon fluxes underestimated compared to the observations (Figs. 4.3b and 4.4b). The hysteresis in the observations can be explained with the transient response of the observation site to the solar heating. Early in the morning the sun is relatively weak, so it takes some time (about 1 hour, according to the Fig. 4.4b) for the surface, the canopy and near surface layer of air to warm up sufficiently and initialize turbulent heat fluxes. In contrast, in the late afternoon when the gradients are sustained relatively longer due to the heat storage at the surface and the near-surface boundary layer. The framework clearly does not reproduce this transient response adequately. The misrepresentation is indicated with a higher correlation coefficient for the simulated surface flux and solar radiation dependence compared to the observed relationship between surface fluxes and radiation. The first and foremost candidate for the discrepancy is the heat capacity of the vegetation canopy, because that factor is completely neglected in the framework. Heat storage in high canopies, as is the case for Hyytiälä, may reach several tens of W/m^2, which approximately equals the difference in the morning latent heat values between the model and the observations (Garratt, p.120, 1994). The overall effect of the storage terms, which represent the dynamic responses in the system, therefore still seems to be underestimated in the model framework. Moreover, a combination of modelled soil heat flux Q_g and the EBL heat storage H_a fails to reproduce the observed hysteresis. We also should not dismiss other possible factors that contribute to the hysteresis and are not incorporated in the model, such as: the apparent higher probability of clouds in the afternoon (Fig. 4.6b), which are indicated by a reduction in the averaged R_s. The latter could offer an explanation for the reverse hysteresis in the model output. Lower R_s in the afternoon also implies a lower modelled heat storage H_a (Eq. 2.20). Consequently, the heat storage contributes less energy to the turbulent heat fluxes in the afternoon than in

the morning (Figs. 4.6).

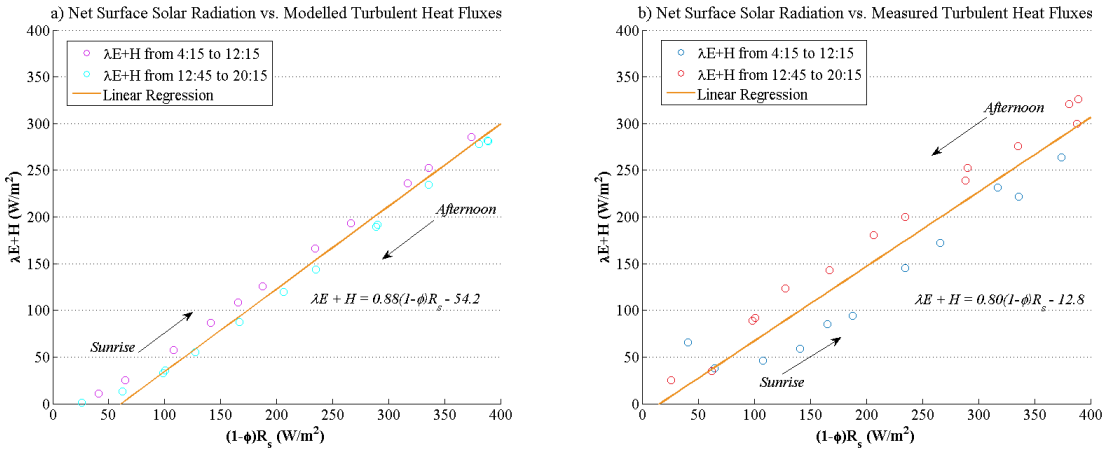

Figure 4.5: Turbulent heat fluxes dependence on solar radiation. Dependence of the surface turbulent heat fluxes on the absorbed solar radiation at the surface. a) The reverse hysteresis of the modelled turbulent heat fluxes suggests that an initialization of the fluxes requires less energy from the solar radiation than its sustenance in the afternoon. This is opposite to the observations b) that in indicate a stronger radiation is required in the morning, in order to build up the gradients than to sustain them in the afternoon. The figures also suggest the interdependence of the turbulent fluxes and radiation in the model is overestimated.

4.2.3 Energetic Boundary Layer Heat Storage

We conduct the analysis of the EBL heat storage with a two-fold comparison of the term. Firstly, we compare the heat storage calculated from the radiosonde data with the analytical storage that has been inferred from the modelled soil heat flux Q_g and observed solar radiation R_s (Eq. 2.3). The comparison is then extended with the diurnally averaged modelled heat storage. The averaged heat storage, calculated from the available radiosonde data is presented together with the analytically calculated heat storage in a whiskers plot (Fig. 4.6a). We observe that the mean values, which are indicated by circles, approximately fit the analytical curve, but the interquartile range is substantial and most of the outliers lie beyond the vertical axis range (Fig. 4.6b). The interquantile range of observations that can exceed $1000\,W/m^2$ implies that a difference of about $100\,W/m^2$ still means a reasonable match of the data sets. Naturally, changes in the boundary layer heat storage cannot exceed the sum of the heat inputs $H + \lambda E + (\frac{3}{4}\tau - 1)R_{L,atm}$ in the system. Ranges of the third quartile in the whiskers plot (Fig. 4.6a) at 11 am and 5 pm therefore, together with most of the upper whisker ranges, appear to be non-physical. However, the results are not really non-physical, they just clearly demonstrate the limitations of a local closure of the system, when there is in fact a significant contribution to the energy changes in the column that is coming from the horizontally advected air masses

with different temperature and moisture properties. This discrepancy demonstrates a troublesome nature of calculating the heat storage from the radiosonde data, which was already indicated in the methodology chapter. Nonetheless, a relatively adequate match in the mean values and the probability distribution of the interquartile ranges indicates that there is a normal distribution of the non-local heating and pressure disturbances. Comparison of the analytically calculated storage term to the averaged modelled storage also shows a reasonable match (Fig. 4.7). Analogous to the modelled turbulent heat fluxes, we observe a slightly quicker buildup of the storage in the morning, and a more rapid demise of the term in the afternoon.

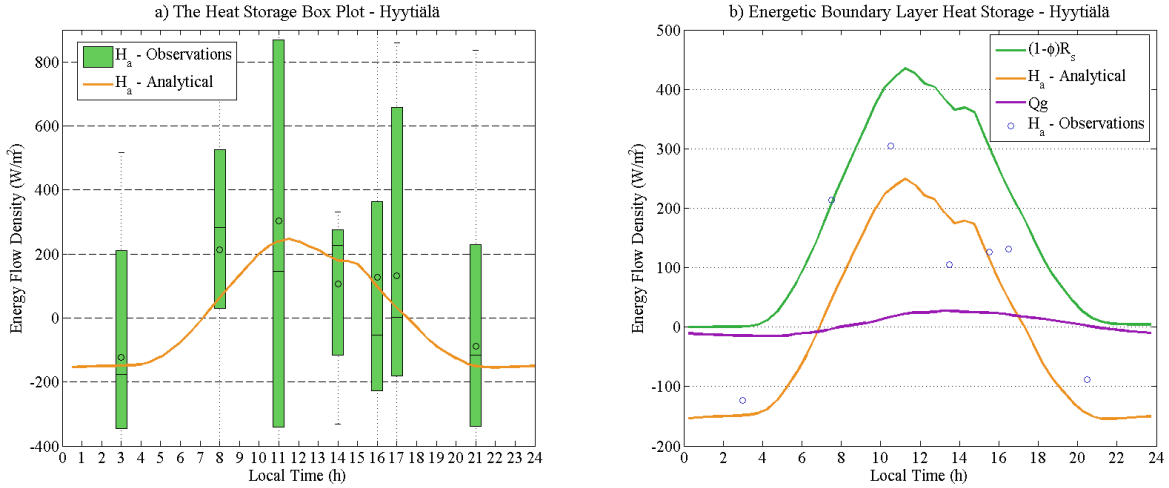

Figure 4.6: Energetic boundary layer heat storage analysis. a) Comparison of the EBL heat storage calculations from the radiosonde data (whisker plot) and the forcing terms (Q_g & $(1-\varphi)\cdot R_s$. The whiskers plot shows a wide inter-quartile range of the radiosonde calculations with the outliers even out of the figure's range. b) The analytical EBL heat storage is plotted together with the forcing terms and the mean values from the radiosonde heat storage (indicated by circles).

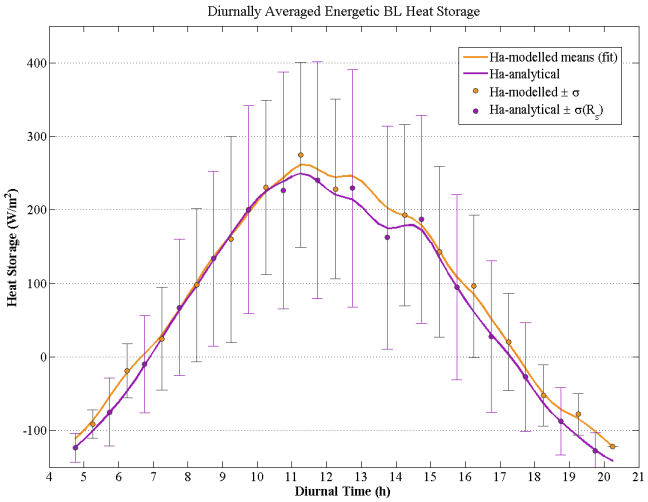

Figure 4.7: Average diurnal cylcle of the modelled EBL heat storage. Comparison of an average diurnal cycle of the observed (violet) and modelled (orange) EBL heat storage. The box plots show standard deviations of the modelled and measured values at a given diurnal time. A close agreement of the plots confirms the physical consistency of the EBL heat storage implementation in the model.

4.2.4 Vertical Exchange Velocity

The diurnally averaged vertical exchange velocity roughly reproduces a typical diurnal shape of the convective velocity scale w_* in a convective boundary layer (Figure 4.8.), (Stull, p. 119, 1988). The variables however differ in the magnitude. A typical magnitude for the convective velocity on a very turbulent afternoon can be in the order of $1\,m/s$ to $2\,m/s$ (Stull, p.118, 1984), whereas the vertical exchange velocity in the model ranges from $4 \cdot 10^{-3}\,m/s$ to $5 \cdot 10^{-3}\,m/s$. By equating an averaged convective boundary layer (CBL) parametrization with our parametrization of the sensible heat flux, we can relate the vertical exchange velocity with the convective velocity scale (Eq. 2.28) (Stull, p. 118, 1988). This step facilitates an approximate modelling of the average rate of vertical convection (Eq. 4.1). The value of the Von Karman constant is set at $k \approx 0.4$ (Stull, p.181, 1988), and the average reference height in the dynamic boundary layer is put at one half of the boundary layer thickness $\overline{z} = \frac{h}{2}$. Finally, by inferring an average ambient temperature difference in Hyytiälä $\overline{(T_S - T_{TBL})} = 30\,K$ and guessing a potential temperature difference in a convective boundary layer $\overline{\theta_S - \theta_{TBL}} = 3\,K$, we roughly approximate the proportion of the temperature difference as $\frac{\overline{T_S - T_{TBL}}}{\overline{\theta_S - \theta_{TBL}}} \approx 10$. This leads us to a first order conversion from w to w_* (Eq. 4.2). Using the conversion, we can see that the model suggests an average convective velocity scale of $0.8\,\frac{m}{s}$ at noon, which is a reasonable first order projection.

$$k \cdot w_* \overline{z} \cdot (1 - \tfrac{\overline{z}}{h})^2 \cdot \frac{\overline{(\theta_S - \theta_{TBL})}}{h} = w \cdot \overline{(T_S - T_{TBL})} \tag{4.1}$$

$$w_* \doteq 200 \cdot w \tag{4.2}$$

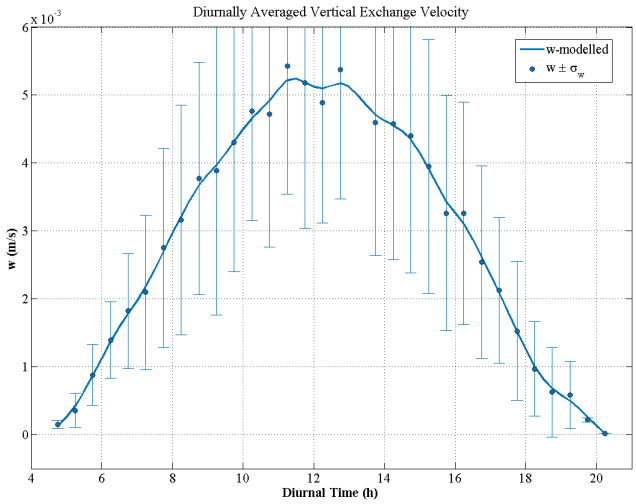

Figure 4.8: Vertical exchange velocity. A diurnal evolution of the modelled vertical exchange velocity closely resembles that of the convective velocity scale w_*, thus demonstrating that our simple framework can be used to provide first-order estimates of the convective transport.

4.2.5 Surface and Atmospheric Temperatures

It was shown in the surface energy balance analysis that the model overestimates the mean surface temperature $\overline{T}_S$ (Fig. 4.2). The diurnal comparison of the modelled and observed surface temperatures reveals that besides the magnitude, the diurnal amplitude of the modelled temperature variation is also seriously exaggerated (Fig. 4.9a). The same outcome applies to the modelled atmospheric temperature (Fig. 4.9b). Even though the model was not designed with an intention to model temperature, this inconsistency points out to a possible major shortcoming of the framework. The underlying reasons for the inconsistency will be presented in the discussion section.

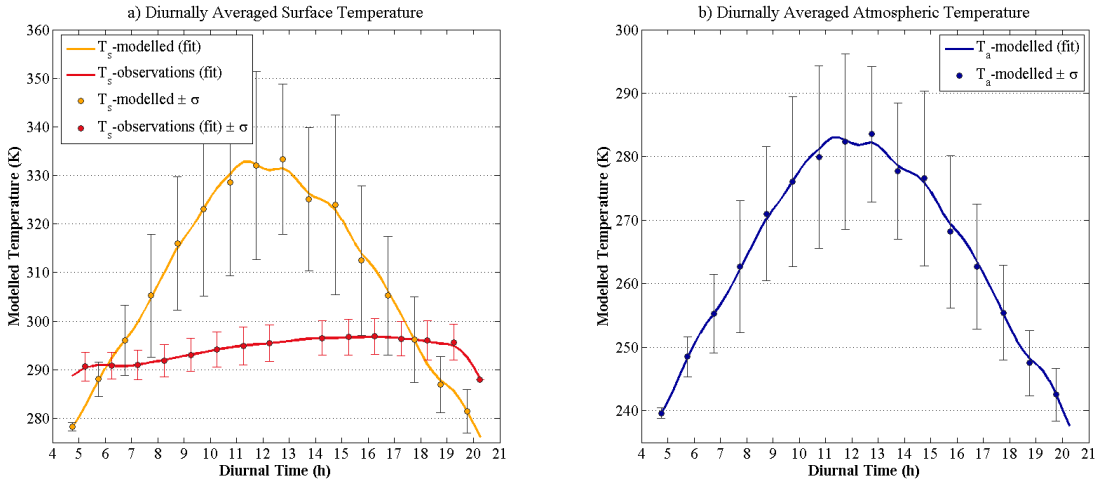

Figure 4.9: A mean diurnal cycle of the surface T_S and atmospheric temperatures T_A. a) Comparison of the modelled diurnal surface temperature evolution with the observed temperature evolution at Hyytiälä. We can see that the model drastically overestimates the amplitude of the cycle. b) The same conclusion can be made for the atmospheric temperature of the TOA reservoir. The box plots in both figures suggest an unnaturally high daily variability of the modelled temperatures (up to 35°C). In comparison, the observed variability of the surface temperature ranges only up to 5°C.

4.3 Changing Climate Sensitivity Analysis

By performing the changing climate sensitivity analysis we explore the response of the systemic variables to an altered radiative forcing at the surface. The design of the executed climate experiments is simplistic, because we only change one systemic variable, namely the optical depth τ that regulates the greenhouse effect. Such basic approach is applied because the framework relies in a considerable extent on the real time observations from the field station. Climate change effects on soil water availability, the soil heat flux, relative humidity at the surface and other environmental factors, such as the physiological properties of vegetation are non trivial and consequently difficult to model. As a detailed systemic climate analysis was not one of our research goals, we did not design climate scenarios for the aforementioned variables and systemic environmental factors, which were determined with the observation data, but rather kept them constant. Still, in the process of testing robustness of the model we conducted a one at a time sensitivity analysis to study the response of the model to the changes in a selection of the environmental parameters: φ, ρ_s, θ_{sat}, r_{min}, $\kappa_s \, and \, C_{veg}$. In that respect, the analysis suggested that minor perturbations of the systemic environmental factors only result in a second-order climate response of the system. On the other hand changes in the greenhouse enhancement and surface temperature represent the first order responses to a changing climate. As we shall see, a change in a greenhouse effect alone significantly alters the dynamics of the system, first and foremost in the processes that depend on the surface temperature. The sensitivity analysis is executed in the following steps. We firstly conduct a general analysis of the surface energy balance under a changing climate. This is followed by a sensitivity analysis of the mean surface temperature $\overline{T_S}$ with respect to an enhanced greenhouse effect. Furthermore, we present the sensitivity analyses of the surface turbulent fluxes and convective exchange, both with respect to $\overline{T_S}$, in order to alow a comparison with the climate sensitivities of the GCMs. EBL heat storage formulation in our model is not sensitive to an enhanced global warming, as it only depends on solar radiation and the soil heat flux (Eq. 2.3). Therefore the sensitivity analysis was not performed on that particular variable.

4.3.1 Surface Energy Balance

Sensitivity of the surface energy budget to the greenhouse effect was tested using a range of nine enhanced greenhouse effect scenarios, as mentioned in the methodology. Here we only present the results of the lowest and the highest greenhouse forcing scenario, because these two examples fully capture the trend of energy redistribution between the fluxes at the surface. Figures 4.9a and 4.9b show the difference in the fluxes with respect to the current climate (Fig. 4.2b). The first observation for both scenarios is that the sum of the turbulent fluxes, as well as the net longwave radiation $R_{net} = R_{L,surf} - \frac{3}{4}\tau R_{L,atm}$ at the surface, is not affected by the changes in the greenhouse effect. Both longwave components show a distinct increase in the $\Delta\overline{L}_{\downarrow} = 8.5\, W/m^2$ scenario and a decrease in

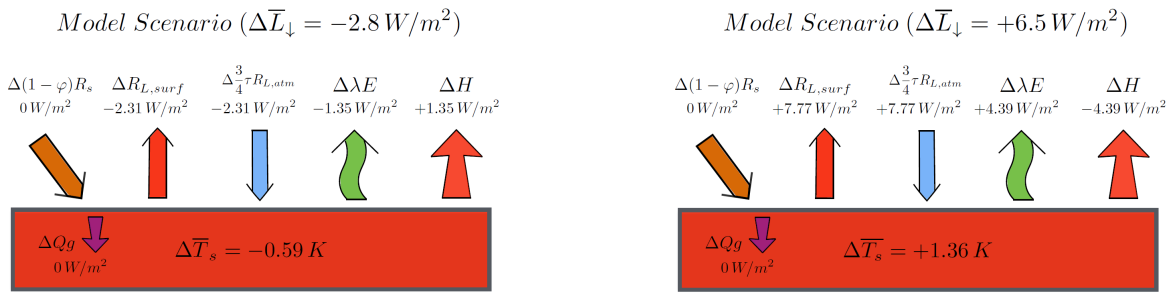

Figure 4.10: The schemes illustrate the responses of the surface energy balance fluxes and the mean surface temperature $\Delta\overline{T_S}$ to the changes in the greenhouse effect. The left panel of scheme presents the responses in a decreased greenhouse forcing, roughly representing the pre-industrial state of the system. The right panel presents the responses in a significantly warmer climate. The illustrations suggest that an enhancement of the greenhouse effect leads to an increased longwave radiation components $R_{L,surf}$ & $R_{L,atm}$ and the latent heat flux λE on one hand, and a decrease in the sensible heat flux H on the other hand.

the $\Delta\overline{L}_{\downarrow} = -2.8\,W/m^2$ scenario. A comparison of the depicted scenarios also shows that global warming is refleced in a shift from the sensible heat flux H to the latent heat flux λE. Trends of an increase in both longwave radiation components as well as in λE and a decrease in H under enhanced greenhouse are consistent with the trends reported by Boer (1993), Gutowski et al., (1991) and Andrews and Forster (2009), who independently performed climate sensitivity analyses on the ensembles of the GCMs outputs. There is however less agreement with the studies regarding absolute changes in the fluxes. The referenced studies agree that an enhanced incoming radiation does not implicitly lead to an equal enhancement of the outgoing radiation component, as suggested by the model. The same holds for the turbulent fluxes. In fact, the studies suggest that for a doubling in CO_2, the increase in the incoming longwave radiation exceeds the outgoing radiation increase by $\Delta R_{net} = [1\,W/m^2{}^{\circ}C,\ 1.4\,W/m^2{}^{\circ}C]$. Thus provided excess heat at the surface is mostly released with an enhanced latent heat flux (Andrews and Forster, 2009). The sensible heat flux sensitivity is in comparison significantly smaller.

4.3.2 Mean Surface Temperature

We can infer from Fig. 4.10b that as a result of a greenhouse enhancement of $8.5\,W$ the surface is projected to get warmer by $1.36^{\circ}C$ above the current mean surface temperature. This is a significantly lower value than the mid range of the warming, projected by the equilibrium climate sensitivity which is likely between $1.5^{\circ}C to 4.5^{\circ}C$ for a doubling of CO_2 concentrations, which represents the radiative forcing of $3.7\,W/m^2$ (Collins et al., 2013; Myhre et al., 1998). The underestimation is reflected in a lower climate sensitivity Λ of the model $\Lambda = 0.21^{\circ}\mathrm{C}/W\,m^{-2}$, when compared with the mean value of the equilibrium

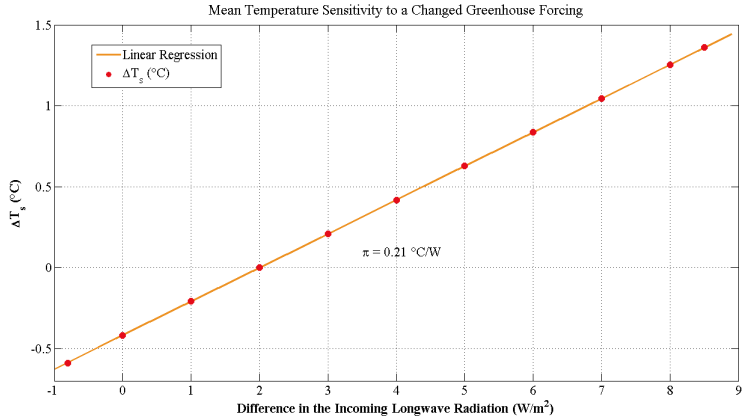

Figure 4.11: Sensitivity of the Mean Surface Temperature to a Changed Greenhouse Forcing. The figure shows temperature responses of the model to a changed greenhouse forcing in relation to the current states. A linear temperature response and a significantly lower climate sensitivity value $\Lambda = 0.27°C/W$ in comparison to the mean equlibirium climate sensitivity from GCMs $\Lambda = 0.81°C/W$ demonstrates that our simple framework disregards some of the crucial positive feedbacks in the climate system.

climate sensitivity range $\Lambda = 0.81°\mathrm{C}/W\,m^{-2}$ (Collins et al., 2013).

In the following step the sensitivity analysis of the greenhouse enhancement was extended up to a value corresponding to a $3.7°C$ warming, the mean projected temperature increase by 2100 in the RCP 8.5 scenario (Collins et al., 2013). This enabled us to perform the sensitivity analysis of the surface fluxes and the convective transport with respect to a mean temperature change, which is a common approach when presenting climate sensitivities of the other variables.

4.3.3 Surface Turbulent Heat Fluxes

Changes in the surface turbulent fluxes in the global warming scenarios can be attributed to the projected alteration of the surface energy balance and higher temperatures at the surface (Collins et al., 2013). The studies suggest a considerably higher sensitivity of the latent heat flux compared to the sensible heat flux. For that reason the analysis will mostly address the global warming effects on evaporation. The most important effect on surface evaporation is the saturation water vapor pressure s (Eq. 2.23), which would on average increase the evaporation at a rate of $6.5\%\,°C^{-1}$ (Boer, 1993). The saturation vapor pressure sensitivity is an upper limit of a relative increase in evaporation that can only be achieved under a sufficient availability of moisture and energy for evaporation (Boer, 1993). Therefore, the projected changes in evaporation cannot be adequately made just by looking at the temperature dependence of the saturation vapor pressure. The reported range of sensitivities from climate models with $\Delta\lambda E$ from $1.7\,W/m^2°C$ to $2.2\,W/m^2°C$ supports the existence of the processes that inhibit the potential increase of evaporative

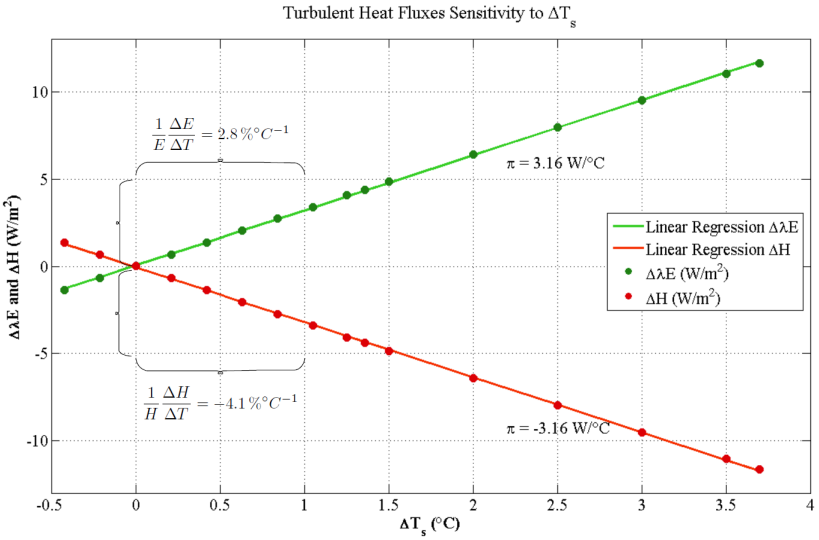

Figure 4.12: Sensitivity of the surface turbulent heat fluxes to a mean surface temperature change. The figure shows the surface sensible and latent heat responses to an increased mean surface temperature $\overline{T_S}$. In absolute terms the sensitivity of the latent heat flux equals $\Lambda = 3.16\,W/°\mathrm{C}$, whereas the sensitivity of the sensible heat flux equals $\Lambda = -3.16\,W/°C$. It is also demonstrated that in relative terms, a decrease in the sensible heat flux is larger than a relative increase in the latent heat flux, a consequence of the smaller current value of the sensible heat flux compared to the latent heat flux.

rates (Boer, 1993; Gutowski et al., 1991; Andrews and Forster 2009). The modelled sensitivity of evaporation $\Delta\lambda E = 3.16\,W/°C$ agrees well with the reported sensitivities from the climate models (Fig. 4.12). A more detailed analysis showed that $\sim 90\%$ of an increase in the model can be contributed to a change in saturation vapor pressure, and the remainder directly to an increased surface temperature. An increase in $\Delta\lambda E$ in the model is compensated by an equal decrease of the sensible heat flux $\Delta H = -3.16\,W/°C$. The literature also projects a decrease in the sensible heat flux, however the projected decrease ΔH ranges from $-0.2\,W/m^2°C$ to $-0.7\,W/m^2°C$ and is consequently significantly smaller than our model projections (Boer, 1993; Gutowski et al., 1991; Andrews and Forster 2009). In relative terms the evaporation is projected to increase by $2.8\%\,°C^{-1}$, whereas the sensible heat flux is projected to decrease by $-4.1\%\,°C^{-1}$. This is comparable with the study of Kleidon and Renner (2013), who performed a similar study with an even simpler MPP framework, and obtained the relative sensitivity of evaporation of $2.2\%\,°C^{-1}$.

4.3.4 Convective Transport

Mean convective transport, which is related to the vertical exchange velocity in our model w is a very important characteristic of global climate. Our claim stems from the fact that the deep convection in the tropics is the driving process of vertical moisture transport in the Inter Tropical Convergence Zone (ITCZ), the upwelling part of the Hadley cell, which decisively co-regulates the global climate system (Holton, p.378, 1973). The climate sensitivity of convective transport is largely uncertain, as the convective transport is not explicitly modelled in the comprehensive climate models (Betts, 1998; Held and Soden, 2006). Still, there are studies that suggest a likely decrease in the convective transport. Betts (1998) presents a simple reasoning for this trend that is applicable to our model as well. The explanation is based on a parametrization for the latent heat flux that is very similar to ours (Eqs. 2.29 and 4.3). We adapt his reasoning to the particular design of our framework.

$$\lambda E = \lambda \rho w \cdot (q_S - q_{TBL}) \tag{4.3}$$

The climate models project a relative climate sensitivity of the latent heat flux that is smaller than the relative sensitivity of the saturation mixing ratios between the surface and the top of the dynamic boundary layer $q_S - q_{TBL}$. This argument can be supported with our analysis and literature review in the previous section, where we have explained that the saturation vapor pressure climate sensitivity equals $6.5\%\,°C^{-1}$. Climate sensitivity of the mixing ratios is directly proportional to the saturation vapor pressure and therefore also has a relative sensitivity of $6.5\%\,°C^{-1}$ (Boer, 1993). A smaller proportional change in the surface latent heat flux (left hand side of Eq. 3.3) compared to the mixing ratios (the right hand side) therefore requires a decrease in another control variable. The only variable that can change because average density of the air remains approximately constant is the vertical exchange velocity w. Deriving from a simple radiation-convective equilibrium model, Betts and Ridgway (1989) therefore suggest a decrease in convective transport, associated with a change in temperature on the order of $-6.6\%\,°C^{-1}$. Very similar values are suggested by Held and Soden (2006) with $-7.0\%\,°C^{-1}$ and Kleidon and Renner (2013) with $-6.7\%\,°C^{-1}$. The relative sensitivity of the modeled convective velocity scale equals $-6.0\%\,°C^{-1}$ and therefore comes close to the reported values.

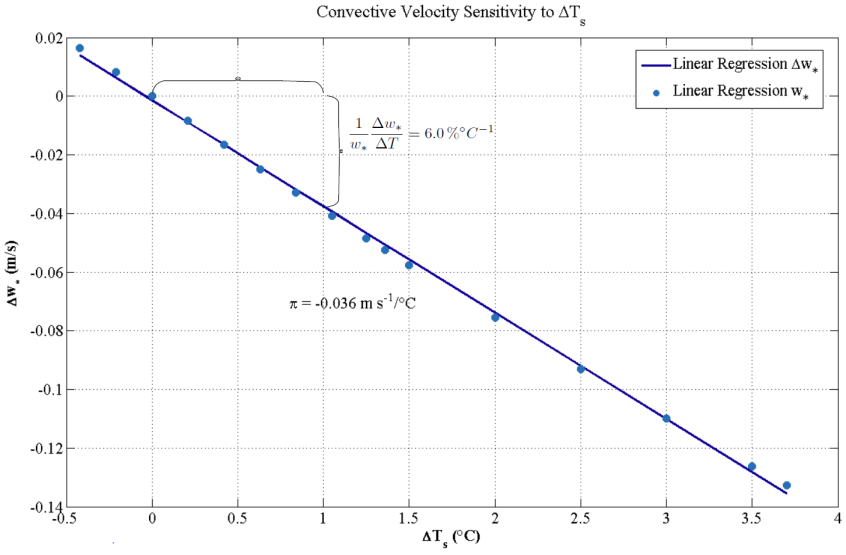

Figure 4.13: Sensitivity of the convective velocity scale to a mean surface temperature change. The figure shows an absolute and a relative response of the convective velocity w_* to the mean surface temperature change $\overline{T_S}$. The modelled relative sensitivity $\frac{\triangle w_*}{w_* \Delta \overline{T_S}} = -6.0\% \, ^\circ C^{-1}$ is in agreement with the provided literature overview. The suggested relative sensitivity implies a significant reduction in the mean convective transport under the temperature increases projected in the RCP climate scenarios by the end of the century:$1.0^\circ C \, to \, 3.7^\circ C$, (Collins et al, 2013).

Chapter 5

Discussion

Even though the proposed framework is extremely simple, the results demonstrate it can provide adequate estimates of the diurnal energy exchange in the land-atmosphere interactions. However, the empirical analysis alone does not provide a sufficient reasoning of the more fundamental question of how the system is regulated and why, if that is the case, there is a tendency in the system to maximize its power generation. Hence, we begin the discussion by providing a clarification of the processes that determine the MPP state of the atmospheric heat engine. This is followed by a holistic evaluation of the alternative framework in projecting the diurnal surface turbulent heat fluxes. We then discuss the implications of the results on the EBL heat storage concept. The implications section is concluded with an overview of the consequences from the changing climate sensitivity analysis. The simplicity of the system naturally comes at a cost of limitations, some of which are presented in the following section. After identifying the limitations, we outline some possible improvements in the design for future work. Finally, we evaluate the prospective use of the MPP limit in the more complex models.

5.1 Implications

5.1.1 The MPP Mechanism

In the first hypothesis we postulated that the surface turbulent heat fluxes drive the atmospheric heat engine which can be assumed to operate according to the MPP limit. The correlation of the modelled projections and the observations, presented in the results section, strongly suggests this is the case but it cannot be interpreted as a sufficient proof of the former hypothesis. After all, the fact that the system is transporting the same amount of heat as a system in a MPP state does not prove that the system is necessarily seeking such a state (Ozawa et al., 2003). For that reason, the MPP and related extremal principles hypotheses have been dismissed by some as coincidental correlations (Ozawa et al., 2003; Goody, 2007). With the intention to remove the shroud of mystery that has up to the point surrounded the MPP concept in our research we present a qualitative

explanation adapted after Kleidon and Renner (2013) and Ozawa et al., (2003), which provides reasoning of how is the system brought to a state of the maximum power generation. In this illustration, we propose the existence of a self-regulating MPP mechanism in the atmospheric heat engine. The working hypothesis of the atmospheric heat engine is that when turbulent fluxes transport heat from a warm T_S to a cold reservoir T_A a part of that heat is converted into kinetic energy. The power generation, given by Eq. 2.15, is proportional to the sum of the surface turbulent fluxes $J = H + \lambda E$ and the absorbed longwave radiation $(\frac{3}{4}\tau - 1)R_{L,atm}$ minus the EBL heat storage H_a, multiplied by the temperature difference of the reservoirs $(T_S - T_A)$. The EBL heat storage H_a and the longwave radiation $(\frac{3}{4}\tau - 1)R_{L,atm}$ can be treated as independent of the temperature difference as well as of the amount of turbulent heat transport (Eqs. 2.3 and 2.17). Therefore, these terms can be treated as constants with respect to the intensity of turbulent heat transport. Consequently, the power generation varies with respect to the turbulent heat transport multiplied by the temperature difference (Eq. 5.1).

$$P \approx J \cdot (T_S - T_A) + const \cdot (T_S - T_A) \tag{5.1}$$

These are in fact two interactive properties of the system. Whereas the temperature difference on one hand drives the turbulent heat transport (Eqs. 2.28 and 2.29), the transported heat on the other hand regulates the temperature difference, thus implicitly affecting the heat transport. The interdependence in the power equation (Eq. 5.1) thus suggests a strong interaction of the surface and the atmosphere (Kleidon and Renner, 2013). The possible states of heat transport and associated power generation range from the static case with no turbulent heat transport where $J = 0 \,\&\, (T_S - T_A) = max$ to the extreme mixing case where $J = max \,\&\, (T_S - T_A) = min$ with the MPP somewhere in between these two cases (Fig. 5.1). The main question is why would the system strive towards the MPP state? Figure 5.1 illustrates the proposed self-regulating feedback mechanism that suggests an explanation for this tendency of the system. Imagine the system in a non-maximum state A, shown on the left side of the figure. A small positive turbulent fluctuation $+\triangle J$ would increase the power generation in the system (Eq. 5.1). An increase in the power generation leads to an increased convective transport, represented by the vertical exchange coefficient w, which leads again to an increased turbulent heat transport J because $H \,\&\, \lambda E \propto w$. Therefore, the fluctuation tends to develop a positive feedback mechanism where $\frac{dP}{dJ} > 0$, which continues to increase the convective transport and turbulent heat fluxes until the system reaches the MPP state (Fig. 5.2a). On the other hand, if the system is in a non-maximum power generation state B, a positive turbulent fluctuation triggers a negative feedback which suppresses the fluctuations (Fig 5.2b) (Ozawa et al., 2003). In contrast, a negative turbulent fluctuation $-\Delta J$ triggers a positive feedback between the temperature difference and an enhanced power generation (Fig. 5.1), which again drives the system towards the MPP state. The proposed mechanism explains the system's tendency towards the MPP state, which is a single stable state of the system and therefore provides justification for our first hypothesis. Still, we should be

aware that this is only a qualitative suggestion of a possible regulation mechanism in the system that still needs further empirical and theoretical study to be properly validated (Paltridge, 1979; Ozawa et al., 2003; Lorenz, 1960).

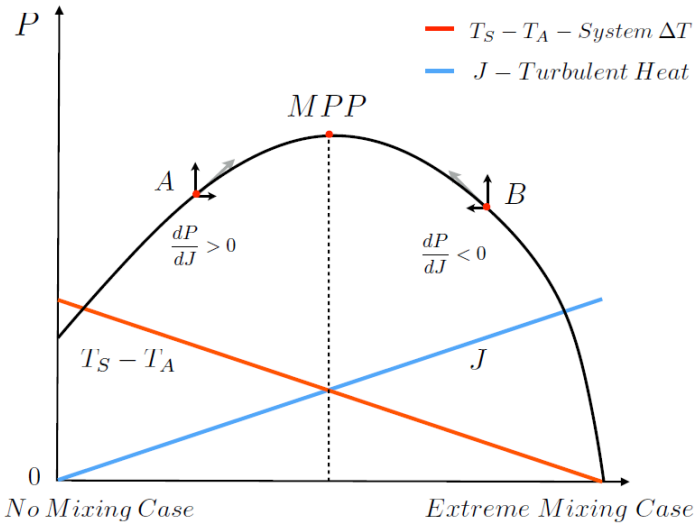

Figure 5.1: Schematic illustration of the proposed self-regulating MPP mechanism, showing power generation as a function of surface turbulent heat fluxes J and temperature difference $(T_S - T_A)$. A positive turbulent fluctuation at A and a negative fluctuation at B trigger a self-perpetuating increase in power generation towards the stable MPP state. Adapted from Ozawa et al., (2003).

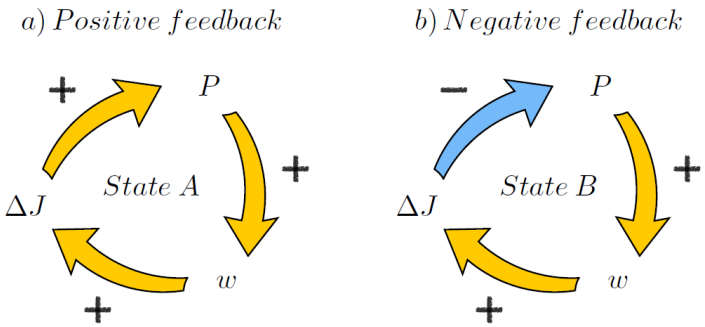

Figure 5.2: Feedbacks in the proposed self-regulating MPP mechanism. If an increase in one variable leads to an increase of the other variable, this positive relation is denoted with an orange arrow and a + sign, while the negative relation is illustrated with a blue arrow and a - sign. a) A positive feedback drives the system from the state A (Fig. 5.1) towards the MPP state. b) A negative feedback suppresses the positive turbulent fluctuations $+\Delta J$ in the state B. On contrary, a negative fluctuation $-\Delta J$ initializes a positive feedback towards the MPP state.

5.1.2 Alternative Approach for the Modelling of the Surface Turbulent Fluxes

A key defining characteristic of the proposed alternative approach is its simplicity. The framework design is capable of modelling the energy dynamics of the atmospheric column with the focus on the near-surface turbulent heat transport. In addition, the framework is capable of modelling the diurnal dynamics of convective transport. What distinguishes our approach from conventional models is the ability to describe the system without an explicit quantification of the motion, described by the Navier-Stokes equations (Stull, p.90, 1988) or alternatively, by the semi-empirical parametrizations of the the boundary layer dynamics (Garratt, p.49, 1992). Furthermore, the state of the system is calculated independently of the previous system's states and only depends on the current state of the forcing variables and the energetic system response captured by the EBL heat storage. Finally, the most advantageous feature of our system is reflected in its ability to model all of the aforementioned processes by using a very limited number of input variables which can be easily obtainable with remote sensing instruments. The diurnal temporal variation of the surface turbulent fluxes in the framework is a function of two energy sources, firstly the radiative terms, which consist of the absorbed solar radiation at the surface $(1-\varphi)R_s$ and longwave radiation terms $-R_{L,0}-(\frac{3}{4}\tau-1)R_{L,atm}$, and secondly by the heat storage terms H_a and Q_g (soil heat flux actually represents the heat storage/release of the soil) (Eq. 2.20). The turbulent heat fluxes are therefore partly regulated by the the solar radiation terms and partly by the transient response of the surface and the EBL represented by the storage terms. Comparative correlation analysis between the surface turbulent heat fluxes and solar radiation (Fig. 4.5) suggests that the model overestimates the role of solar radiation, even though the observations confirm a high dependence of the fluxes on solar radiation. Nonetheless, the results are a clear indication of an improvement over a more simplistic long-term average framework by Kleidon, Renner and Porada, (2014), where the surface turbulent fluxes were entirely dependent on the solar radiation $J_{opt} = \frac{R_s}{2}$, as a consequence of the heat storage extensions. Moreover, we are confident that the overestimation of the solar radiation could be decisively eliminated with an introduction of a canopy storage term, which is potentially a significant energy contribution in a tall pine forest canopy at Hyytiälä (Garratt, p.120, 1994).

The model undoubtedly reproduces the observed diurnal cycle of the surface turbulent fluxes reasonably well (Figs. 4.3b and 4.4b), but on the other hand performs less optimal when it comes to the magnitudes of the fluxes (Figs. 4.3a and 4.3a). As it was explained in the results chapter, the sensible heat flux is underestimated almost by a third, whereas the latent heat flux is overestimated by 15%. There are three factors that may have affected the performance of the model. First and the foremost is a coarse vertical resolution of the two reservoir atmosphere, which implied the use of the parameterizations in which the turbulent fluxes are proportional to the temperature difference between the surface and the top of the EBL. We implicitly do not actually model the surface turbulent fluxes but instead obtain the value of a uniform turbulent heat transport in the EBL. In other words,

as a consequence of a linearized temperature vertical temperature profile, we project the vertically averaged turbulent heat fluxes in the EBL. If we take a look at the mean characteristics of the turbulent heat fluxes within a convective mixed boundary layer (Fig. 5.3), we clearly see that the vertically averaged sensible heat flux is considerably smaller than its surface value whereas an averaged latent heat flux is higher than its surface value. Therefore, the characteristics of the convective boundary layer (CBL) confirm our explanation that the model outputs cannot be strictly regarded as the surface fluxes.

Another indicative reasoning for a discrepancy in the modelled and observed magnitudes comes from a previously conducted data analyses at the Hyytiälä field station and other Scandinavian pine forest sites (Ilvesniemi et al., 2010; Suni et al., 2003). In the article *Water balance of a boreal Scots pine forest* by Ilvesniemi et al. (2010), the hydrological cycle of the site was thoroughly analyzed in the years 1998-2006. Among the most interesting findings is an observation from a number of field studies in Scandinavia that the energy balance could not be closed by the eddy covariance (EC) measurements, possibly because the method underestimates evapotranspiration (Ilvesniemi et al., 2010). The authors therefore suggested that the EC measurements underestimate the fluxes on the order of $\sim 10\%$ and probably up to 40% annually. The EC method at Hyytiälä has been compared with the residual method where all the other water flows have been measured. The residual method infers higher annual fluxes up to 78%, though the method lacks reliability (Ilvesniemi et al., 2010). On the basis of these conclusions, a negative instrumentation bias should be assumed for the measured evapotranspiration values. The authors suggest that the sensible heat flux is probably also subjected to a negative instrumentation bias but do arrive at an estimate. Due to significant standard deviations the suggested instrumentation bias and the time-scale methodological differences in the analysis by Ilvesniemi et al., (2010), the suggested corrections were not used to correct our observation data set. Still, for the purpose of a qualitative analysis we can assume that the observed surface turbulent heat fluxes should be evidently increased.

Finally, the third factor is a probable flaw in the framework design that is related to the greenhouse radiation term in the EBL. After we had already conducted the model runs and completed most of the model analysis, it was discovered that the proposed concept of greenhouse absorption in the EBL is not physically consistent. However, this inconsistency does not seriously affect the qualitative implications of the results. The flaw will be described in more detail in the following section. At this point it should only be noted that a correction of the faulty greenhouse term leads to a slightly altered expression for the sum of optimum turbulent heat fluxes (Eq. 5.2).

$$J_{opt} = \frac{(1-\varphi)R_s - Q_g - R_{L,0} + H_a}{2} \tag{5.2}$$

The new expression only differs from the previous one (Eq. 2.26) by effectively excluding the negative greenhouse absorption term, which reflects the assumed net longwave absorption in the boundary layer. Elimination of the term results in a net increase of the surface turbulent fluxes J. On average, the change implies an increase of the turbulent

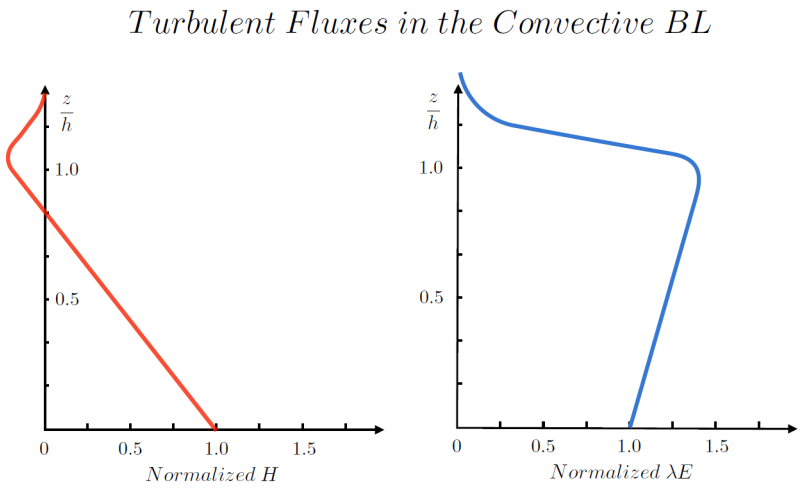

Figure 5.3: Schematic illustration of the mean turbulent heat fluxes within an idealized CBL. Horizontal axes are normalized with respect to the surface values of the heat fluxes, whereas the vertical axes are normalized with respect to the top of the boundary layer height. It is commonly observed that the sensible heat flux H decreases with height, while the latent heat λE increases with height. Adapted from Stull, p.442, (1988).

fluxes by $68\,W/m^2$ which is a 36% relative increase.

In the following step the three presented factors are qualitatively put together. A misrepresentation of the modelled surface turbulent fluxes due to the coarse two reservoir resolution implies that the modelled latent heat flux should be increased, whereas the modelled sensible heat flux should be decreased in order to correspond with the realistic surface values. An exclusion of the greenhouse term implies an increase in the both modelled fluxes. The sum of these two corrections would therefore imply a significant increase in the modelled sensible heat flux and a slight increase in the latent heat flux (Table 5.1). Finally, the negative instrumentation bias means a necessary increase in both turbulent heat fluxes from the observations. Consequently, a consistent consideration of the three factors would most likely lead towards a better agreement of the latent heat fluxes and also to a significantly better match of the sensible heat fluxes. The overall implications of the qualitative analysis are presented in Table 5.1. The qualitative analysis, which outlays some potential improvements in the framework thus only strengthens the argument of the framework's potential applicability in modelling the surface turbulent fluxes and in that way confirms our second hypothesis.

Another notable demonstration of the the framework's applicability is its ability to give reasonable first order estimates of the transport within the CBL. By relating the vertical exchange velocity w to the convective velocity scale w_* (Eqs. 4.1 and 4.2) we have connected two distinct boundary layer concepts, namely the dynamic boundary layer and the EBL. The modelled convective scale velocity is therefore not just an additional

	Uncorrected values	Vertical uniformity	Instrument bias	No GHG
H_{obs}	$109.0\,W/m^2$	/	↑	/
H_{model}	$77.1\,W/m^2$	↑	/	↑↑
λE_{obs}	$96.4\,W/m^2$	/	↑↑	/
λE_{model}	$110.7\,W/m^2$	↓	/	↑↑

Table 5.1: The table presents the identified factors that have affected the bias of the modelled surface turbulent heat fluxes. The effects are presented with arrows. An upward facing arrow suggests a positive correction of the flux, wheareas the downward facing arrow suggests a negative correction. The number of arrows demonstrates the assumed magnitude of a recommended correction of the variable. Overall, we can see that the modelled and the observed λE and H should probably be increased. The proposed corrections would presumably lead to a better agreement between the observations and the model.

modelling feature. It is also an affirmation that the two boundary layer concepts are not mutually exclusive but rather complementary.

5.1.3 The Changing Climate Experiments

A changing climate sensitivity provides insight in the model's response to an enhanced greenhouse effect. The projected sensitivity responses which were presented in the results chapter are generally comparable with the trends of the more complex climate models. There are however considerable differences in the magnitudes of the climate projection trends. In this subsection we further discuss the interpretation of the results and explain their implications for the climate system.

The analysis of the model's surface energy balance sensitivity shows that the increases in the outgoing surface longwave radiation $R_{L,surf}$ and latent heat λE are balanced by equal decreases in the atmospheric longwave radiation $R_{L,atm}$ and sensible heat H. Therefore, on contrary to the referenced models, our climate experiments suggests that there is no interaction between the longwave components and the turbulent heat fluxes responses. Increases in the surface longwave radiation $R_{L,surf}$ and latent heat λE are balanced by the equal decreases in the atmospheric longwave radiation $R_{L,atm}$ and sensible heat H. The reason behind an inconsistency between the referenced and modelled surface energy balance sensitivity analyses lies in the simplistic longwave radiation transfer of our model. The sensitivity analysis showed that the $R_{L,surf}$ response of the model equals a change in the incoming longwave radiation: $\Delta R_{L,surf} = \frac{3}{4}\Delta\tau \cdot R_{L,atm}$ Consequently, even though the equation for a difference in the surface energy budget at different climatological conditions: $\Delta R_{net} = \Delta H + \Delta\lambda E$ (Boer, 1993) holds also for our model, the model does not consider a possible energy transfer between the longwave and turbulent heat fluxes because the longwave interdependence allows no changes in the net radiation at the surface ($\Delta R_{net} = 0$).

An oversimplified parametrization of the longwave radiation also explains the overestimation of the sensible heat flux response to a surface warming. The model also projects a significantly lower climate temperature sensitivity $\Lambda = 0.21°\mathrm{C}/W$ when compared to the mean value of the equilibrium climate sensitivity range value $\Lambda = 0.81°\mathrm{C}/W$ (Collins et al., 2013). Nonetheless, we should not jump to conclusions about the model's performance. Naturally, the simple framework does not incorporate the positive climate feedbacks, such as the cloud feedback, the vapor feedback and the ice-albedo feedback which are essential features to be considered in a comprehensive climate sensitivity analysis. Therefore, a smaller climate sensitivity of the model, when compared to the sensitivities of the state of the art GCMs, should be expected. As a matter of fact, the sensitivity analysis of the model closely resembles the climate sensitivity due to the greenhouse effect without climate feedbacks: $\Lambda = 0.27°C/W$, which is given in the IPCC's Third Assessment Report (IPCC, 2001). Exclusion of the positive feedbacks also explains why the modelled sensitivity perfectly fits a linear function (Fig. 4.11).

Sensitivity analysis of the mean diurnal convective transport showed the best agreement with the reported values of the mean global convective transport. The results suggest strong global warming implications on the convective systems. Would vertical rates of transport really be decreased by $\sim -6\%\,°C$, as suggested by our model, that would imply an approximate reduction of the vertical transport by about 20 % by the end of the century for the RCP 8.5 climate scenario (Collins et al., 2013). The corresponding weakening of the Hadley cell could seriously alter the patterns of heat transport to the mid-latitudes. Finally, we should briefly discuss the implications of an enhanced evaporation on the water cycle. Normally one would expect that higher rates of evaporation would also imply more precipitation. That may be true on a global scale, however, the water cycle is a complex non-local system implying that a steady state assumption between precipitation and evaporation does not hold for the local systems such as ours. An enhanced evaporation alone therefore does not provide a full picture of the effects on the water cycle at a particular site. While an enhanced evaporation can lead to the drying of the soils and vegetation, the actual state of the modules clearly also depends on the local changes in precipitation (Collins et al., 2013).

5.2 Limitations

Our simple framework is evidently subjected to a number of limitations, some of which were already briefly outlined in the previous sections and in the results chapter. Here we present the most crucial limitations and hence outline the possible future improvements.

5.2.1 The Two Reservoir Representation of the Atmosphere

Even though an introduction of the EBL reservoir was an improvement over the previous MPP frameworks with a single atmospheric reservoir (Kleidon, Renner and Porada, 2014), it still provides a coarse resolution in the model. As it was explained in the previous section, the single EBL reservoir imposes a uniform heat transfer in the system, thus making the framework generally applicable only for the certain conditions that resemble the presence of a well-mixed CBL. Even then, with an assumed EBL depth of $\sim 5\,km$ we are representing a vertical domain that is more than twice the size of the typical CBL vertical domain (1500-2000m) (Stull, p.460, 1988) Commonly observed conditions of a non-linear vertical temperature profile and temperature inversions in certain parts of the boundary layer therefore cannot be reproduced with this framework. A coarse resolution is even more problematic in the TOA reservoir, the energetic reservoir that aggregates the properties of an entire upper troposphere and stratosphere, which are thermodynamically very diverse, with a single reference temperature T_A. That temperature is together with the surface temperature T_S regulating the entire longwave exchange in the system. Moreover, the top of the boundary layer temperature T_{TBL} is directly coupled with the TOA temperature, therefore T_A additionally also co-regulates the surface turbulent heat transport. In reality however, the stratospheric temperatures and the temperatures in the upper troposphere, which are represented with the T_A do not play a role in the land-atmosphere exchange. This unrealistic coupling of the surface and the TOA reservoir is clearly reflected in the diurnal cycle and an overestimated amplitude of the T_A (Fig. 4.9b). That also implies a high variability and an overestimation of the atmospheric longwave radiation $R_{L,atm}$ around noon and its underestimation in the morning and late afternoon. Atmospheric radiation is an important source of energy for the surface reservoir, therefore the overestimated variability of the TOA reservoir temperature also affects the surface temperature (Fig. 4.10). In that way the coupling explains an unrealistic diurnal variability of the T_S.

Besides this misrepresentation of the temporal variability in the temperatures, the model also overestimates the surface temperature magnitudes with the modelled mean temperature $\overline{T_S}$ approximately $14°C$ higher than the observed mean value at Hyytiälä. The higher $\overline{T_S}$ as well as the overestimated surface longwave components are a consequence of the opaque atmosphere assumption. With this assumption we assume no direct longwave radiation release from the surface into space. The energy that should be emitted into space is instead absorbed in the atmosphere with a significant part then radiated back to the surface. The opaque atmosphere therefore overestimates the longwave radia-

tion fluxes at the surface, which results in a considerably warmer surface. A back of the envelope calculation of the surface energy balance, assuming that$\sim$ 20% of the surface radiation $R_{L,surf}$ is directly radiated into space (Trenberth et al., 2009; Staley and Jurica, 1972), shows a reduction in the surface temperature by $\sim 13°C$, which brings the mean surface temperature very close to the observed mean value.

The two reservoir representation of the atmosphere also does not explicitly model the clouds which limits the framework's applicability to the relatively cloudless meteorological conditions. The effect of clouds is actually implicitly included in the framework because the clouds decrease the measured solar radiation at the surface $(1-\varphi)R_s$, which is used as a forcing input in the model. However, this representation proves to be insufficient. As we know, the model projections are made from the current state of the forcing variables, thus ignoring the previous states of the system. In that way the model disregards the inertial processes in the system that for example sustain the temperature gradients. Whereas the presence of clouds decreases the absorbed solar radiation at the surface, this does not directly imply an immediate temperature difference decrease in the system, as suggested by our framework. This example clearly demonstrates a significant deficiency of the energy equilibrium calculations without referring to the state of the system in the previous time step.

5.2.2 Soil and Vegetation Modules

A significant effort was invested in the soil and vegetation modules design, which is reflected in the relatively advanced 4-layer soil heat flux module, a 3-layer soil moisture module and an isothermal canopy vegetation module (appendix A). The modules are relatively complex when compared with the considerably coarser atmospheric heat engine framework. That raises the question whether the additional complexity in the modules considerably improves the quality of our framework, or should the invested time be more rationally spent for other model improvements? The results, presented in the appendix A, undoubtedly show that the modules capture the observed moisture and soil heat flux dynamics reasonably well. However, the precision of the modules' outputs is actually much less detrimental for the physical consistency of the framework than some other issues, which could be improved, for example the opaque atmosphere assumption. In addition, a possible implementation of the canopy heat storage has been proven to be much more essential to improve the precision of the model than the additional reservoirs or layers in the soil. The obtained results and gained insights in the application of the framework have thus led to a redefinition of the priorities of the framework components, which should be considered in the future.

5.2.3 The EBL Heat Storage

Energetic partitioning of the atmosphere with an introduction of the EBL heat storage, which was proposed by Kleidon and Renner (2014), is a fundamentally new concept in the MPP heat engine model. The extension transforms a static representation of the convective heat transfer, occurring between the surface and atmospheric reservoirs (Fig. 1.2), into a diurnally variable process, which interactively responds to the energetic state of the near-surface atmosphere (Fig. 1.3). An analytical calculation of the storage term together with the heat storage calculated from the radiosonde measurements agree reasonably well with the model outputs (Fig. 4.7), thus suggesting that the energetic partitioning of the atmosphere is physically consistent. However, a wide scatter also demonstrates the difficulty of inferring the EBL heat storage from measurements (Fig. 4.6). In the methodology chapter, it was suggested that the main source of error might stem from the role of synoptic weather systems, which are independent of the local surface heating. These changes lead to a quick drop/increase in the surface pressure and vertical temperature profile, which can have a dominating effect on the calculated sensible heat storage Ha_{SH} (Eq. 3.4). We proposed a solution by introducing a fixed pressure thickness of the EBL Δp, thus effectively conserving the heat capacity of the air in the column, which removes the noise effects of the surface pressure tendency. Nevertheless, even with a fixed pressure thickness of the column, the system is still subjected to the horizontal transport of heat and moisture, which are changing the energy properties of the atmosphere at a measuring site. Therefore, our solution does not fully eliminate the effects of synoptic changes. Moreover, it should be noted that the pressure tendency term is also a result of a local heating. By eliminating the second term in Eq. 3.4 the surface heating effect is unavoidably eliminated and the storage term can become either underestimated or overestimated. Calculation of the storage from radiosonde measurements is for that reason alone, besides the errors in the measurements, always subjected to a mistake, either by an inadvertent inclusion of the synoptically associated pressure tendency coming from a horizontal heat transport or by an exclusion of the local pressure tendency. These points stress the importance of including the horizontal heat advection in the EBL heat storage calculation in order to improve the system's projections on a daily basis. The current implementation of the EBL is only applicable when the local heating dominates, a good example being the calm and cloudless sunny days. Furthermore, the radiosonde measurements do not necessarily reflect the local heat storage at the observation site, as they are normally being horizontally transported by the wind. In that way, during their ascent to the 400 hPa, the radiosondes can measure the atmospheric properties over the surface types which have little or no resemblance to the surface at the site of their release.

Another problem in the current EBL heat storage design is an inaccurate representation of the greenhouse effect. While it is true that the water vapor in EBL does play a significant role of an absorbent in the greenhouse effect, thus absorbing a fraction of the longwave radiation in the system, the water vapor is also emitting longwave radiation (Held and Soden, 2000). Furthermore, the boundary layer is usually (when there is

no vertical temperature inversion) a net emitter of the longwave radiation (Stull, p.507, 1988), though the longwave cooling is not the dominating energetic term in the CBL. Our representation of the greenhouse effect in the EBL disregarded the emitted longwave radiation, thus wrongly attributing the reservoir with an additional energy input. This mistake should be corrected by assuming a net zero greenhouse heating of the boundary layer, which would actually simplify the calculation of the turbulent heat fluxes (Eq. 5.1). The correction would imply an average increase in the surface turbulent fluxes by $\approx 36\%$. As a consequence of the increased surface turbulent heat fluxes, the mistake does not affect the values of the EBL heat storage because the decrease in heating, associated with the greenhouse enhancement, would be compensated by an increased turbulent heating.

5.2.4 Power Generation and Dissipation in a Steady State

Another limitation relates to the power-dissipation steady state assumption $P = D$. While turbulent convective dynamics and dissipation are indeed two inherently related processes, they certainly are not codependent as suggested by the steady state. First of all, the assumption is not realistic due to a chaotic nature of the turbulent processes (Stull, p.168, 1988). Clearly the system cannot be treated in a steady state during the power generation dominated buildup of the boundary layer in the morning and the dissipation dominated breakdown of the boundary layer in the late afternoon (Kleidon, Renner and Porada, 2014). Yet, the diurnal average of the system can be regarded to have reached a steady state, particularly in the periods of a relatively constant sustenance of the convective motions (Kleidon, Renner and Porada, 2014). We briefly outline a theoretical proposal how to circumvent the steady state assumption. We first introduce the aerodynamic friction force which determines the rate at which the power generation of the atmospheric engine is dissipated near the surface:

$$F_{drag} = C_D \cdot \rho v^2 \tag{5.3}$$

where C_D is a drag coefficient, depending on the dynamic stability of the atmosphere and v is near surface wind at the chosen reference height. This is a standard approach in the surface friction modelling (Kleidon and Renner, 2013; Garratt, 1977). We rewrite the friction equation into the Reynolds stress form (Stull, p.63, 1988):

$$C_D \cdot \rho v^2 = (\rho v) \cdot w \tag{5.4}$$

This enables us to interpret the friction force as a result of a surface pull on the air due to a momentum exchange ρv between the surface and near-surface atmosphere that happens with an effective vertical exchange velocity $w = C_d v$ (Kleidon and Renner, 2013). The friction force dissipates the power near the surface at the rate that is proportional to the near-surface wind $D = F_{drag} \cdot v = \rho w \cdot v^3$(Kleidon and Renner, 2013). This parameterization of the dissipation introduces an additional unknown variable in the system of equations, namely the near surface wind v. To obtain a determined system of equations,

we have to express the latter variable as a function of other variables and parameters. One of the possible approaches to resolve this problem is application of empirical boundary layer relations. Garratt, (1977) suggests to use the following experimental relation between the exchange velocity and the near-surface wind $w = \frac{0.75 \cdot v + 0.067 \cdot v^2}{10000}$. By using such an empirical relation, in order to express v with w we implicitly assume that the dissipation is proportional to the intensity of convective motions in the system w_*, an assumption that was also made in the proposed self-regulating MPP mechanism (Ozawa et al., 2003). A further improvement would be to relate the velocities without applying the empirical relations. A decrease in reliance on the empirical relations was after all one of the main advantages of the MPP framework in relation to the conventional frameworks. Such an extension should enable us to model the surface turbulent fluxes without the steady-state assumption, which should in theory improve the precision and physical adequacy of the framework. On the other hand, an application of the empirical relations advantages of our framework, namely reliance on empirical parameterizations.

5.2.5 Representation of the Water Cycle

We derived the entropy production in the system by applying the assumption of no latent heat release in the boundary layer (Eq. 2.24). While the moisture input in the system is supplied by the latent heat flux, the discharge of moisture from the EBL is represented only implicitly, namely by the outgoing turbulent heat flux J_{out}. The J_{out} accounts for the transport of the remaining sensible and latent heat from the heat engine into the TOA reservoir. There the latent heat release is not properly addressed as the framework does not simulate precipitation. The water supply from precipitation that provides water for soil moisture is therefore modelled from the measured precipitation rates. Even so, the framework's representation of the water cycle still fails to capture the actual circulation of water moisture in the system. As we know, the precipitation i.e., the convective latent heat release predominantly occurs within the boundary layer (Koenings et al., 2012). The considered role of moisture transport into the TOA reservoir is therefore inadequate. Also, the water cycle generally cannot be treated as a closed local system. The precipitation events are especially in the high latitudes normally dominated by the advected convective systems and weather fronts, which would require an introduction of the horizontal moisture transport. Surprisingly, the deficiencies in the water cycle representation did not decisively affect the comparative EBL heat storage analysis as the modelled EBL heat storage reproduced the diurnal variability of the heat storage calculated from the radiosonde data reasonably well. This is probably a consequence of a relatively dry measuring period with only three notable precipitation events thus making the representation of the water cycle irrelevant in the most model runs.

5.3 Prospective Applications of the MPP in the Complex Models

We conclude the discussion by outlining the possible advantages of applying the MPP limit in the more complex models. While the conventional models have a capability to evaluate the thermodynamic limits in the system, these limits are not used as thermodynamic constraints of the system's dynamics (Kleidon et al., 2006). The research that we have conducted demonstrates that the MPP limit can be employed to roughly reproduce the dynamics of the energetic land-atmosphere interactions. The proposed atmospheric heat engine framework therefore has a potential of becoming a useful concept in atmospheric modelling science. Yet, there is a long way to that point with numerous challenges on its way. The first prerequisite would be to improve the simple conceptual thermodynamic limit models by adding important processes to the framework, which are at this point neglected and and should improve the framework's precision and extend its applicability to different atmospheric conditions. However, even an improved version of the atmospheric heat engine with an additional degree of complexity would still have to be subjected to a thorough performance analysis. Such an analysis would probably be analogous to our comparative analysis between the model and observations. If such a framework proved itself adequate to model the energetic dynamics in the land-atmosphere system, this could provide an alternative approach for the modelling of land-atmosphere exchange. Such an alternative approach could improve the precision of the current GCMs, since these models largely rely on the empirical functions from the similarity theory. While it is true that the empirical functions were derived from numerous detailed field studies, these functions do not explain the fundamental nature of the turbulent processes. It is also clear that the empirical functions, derived from particular sites do not apply equally well to the varieous sites with markedly different systemic properties (Stull, p.348, 1988). The atmospheric heat engine framework on the other hand does not require the empirical functions of the static and dynamic stability in the atmosphere to model the exchange processes, which are in our model represented by w. Rather, in the presented framework, the state of the exchange processes in the system is directly inferred from the MPP generation limit. Finally, if the tendency to maximize power generation will eventually be proven as an inherent characteristic of the system, that would be a tremendous leap forward in the general understanding of the land-atmosphere interactions.

Chapter 6

Conclusions

A simple energy equilibrium framework has been devised to test the applicability of the MPP limit in land-atmosphere interactions on the diurnal time scales. The underlying working hypothesis of our research was that we can describe the processes of vertical turbulent heat transport and convective motions by treating the atmosphere as an idealized heat engine, operating at its thermodynamic limit. Such an atmospheric heat engine strives to maximize power generation in the atmosphere by converting a fraction of the vertically transported turbulent heat flux into convective motions. The convective heat transport tends to take place in the lower troposphere, a part of the atmosphere that is energetically influenced by the turbulent heat fluxes from the surface. For that purpose we have introduced an energetic boundary layer (EBL) which constitutes the operational domain of the atmospheric heat engine. Quantification of energy and entropy production in the EBL has enabled us to make the first order estimates of the surface turbulent heat fluxes E & λE and convective transport w_*in the system. A detailed comparative analysis of the model results with the measurements from Hyytiälä has demonstrated the framework's ability to decently project the diurnal cycle of the surface turbulent heat fluxes and convective transport. The average magnitudes of the projected fluxes have shown a lesser resemblance with the observations. Still, a clear correlation between the model and the observations has proven that there is a consistent representation of the energetic dynamics in the local atmospheric system. Moreover, we have proposed the solutions to the identified flaws in our framework that have affected the precision of the projections, and have provided reasoning that an implementation of these solutions would bring the observations and the model to a better agreement.

Reasonable representation of land-atmosphere interactions with our model has demonstrated that the atmospheric system indeed operates near its thermodynamic state of maximum power generation. In that way has the comparative analysis justified the most important working hypothesis of our research, i.e., treating the atmosphere as an idealized maximum power generating heat engine. Yet, even though the results suggest that the system's dynamics can be modelled with the MPP approach, this in itself does not prove that the system seeks such a state. In order to fully justify such an assertion, the empir-

ical analysis of the model and observations has to be complemented with a fundamental physical theory which would explain the tendency of the system to maximize power generation. Our contribution to that aspect of research was the conceptual illustration of the self-regulating MPP mechanism which was adapted from Ozawa et al., (2003) and Kleidon and Renner, (2013). While the illustration has provided a plausible conceptual reasoning for the MPP limit, the existence of such a self-regulating mechanism remains uncertain. That is because the more particular applications of disequilibrium thermodynamics, such as the MPP limit, constitute a relatively new and unexplored field of research. Therefore, further evaluations are needed to test the applicability and scope of validity of the MPP limits. Crucial prerequisites for a more detailed and rigorous study would be to improve the precision and physical consistency of the alternative models which would extend its applicability to a wider range of observed meteorological conditions. We have identified and outlined the most fundamental improvements for out framework. A multiple heat storage framework would increase the vertical resolution of the model and extent its applicability to non-convective situations. An explicit representation of the dissipative processes would improve the consistency of the framework during the periods of the day when power generation and dissipation are not in a steady state. Finally, the local water cycle extension would broaden the physical consistency of the framework to the situations of wet condensation in the EBL.

The contribution of this research is twofold in its nature. First of all, the demonstration of the model's capabilities in estimating the surface turbulent heat fluxes puts the framework into a perspective of becoming an practically applicable modelling tool.

With an improved precision and reliability, the MPP models could become useful for providing the estimates of the surface turbulent fluxes on the local spatial scales. Framework's simplicity that is best captured by the reliance on generally accessible input data, which can be obtained from the satellite measurements, could make these models suitable for estimating the surface turbulent fluxes worldwide, including the remote and underdeveloped regions which lack the field measurements. Secondly, the research has identified and structured the future potential uses of the MPP limits in the more complex models. We have argued that the MPP approach could potentially complement the conventional GCMs by adding an additional physical constraint to the system, thus reducing their reliance on the empirical parametrization of the fluxes. A more advanced application of the thermodynamic limits could in that way potentially lead to an improved precision of the conventional GCMs. Furthermore, the alternative approach could facilitate a more comprehensive understanding of the fundamental principles of land-atmosphere interactions. At the same time, we have also pointed out some of the challenges that lie ahead before these potentials could materialize. From that perspective we view this thesis as a study that has proven the applicability of the alternative MPP approach and has outlined its prospectives which is why it may serve as a reference guide for future research.

Appendix A

Soil and Vegetation Modules

In this appendix we provide a more detailed description of the soil and vegetation modules design. We also present the model outputs and compare them with observations from Hyytiälä.

A.1 Soil Heat Flux

A.1.1 Model Implementation

Heat transfer and temperature in the soil were calculated from the Fourier's law for heat conduction (Eq. 2.30) and the energy balance equation for each of the four soil layers over a selected period of $\Delta t = 30\,min$ (Eq. 2.32). These equations are solved numerically and are therefore presented in the finite difference form (Eq. A.1). The system of equations is solved with a numerically stable forward Euler method, where Δz stands for the thickness of a single soil layer, ρ refers to the density of the soil and c_s is the specific soil heat capacity:

$$\frac{Q_{g\,i-1\mapsto i} - Q_{g\,i\mapsto i+1}}{\Delta z} = \frac{\rho_{s,i} \cdot c_{s,i} \cdot (T_{s,i}(t+\Delta t) - T_{s,i}(t))}{\Delta t} \tag{A.1}$$

The soil is partitioned into 4 layers so the boundary conditions have to be applied on the top layer and the fourth layer of the soil in the framework. For the top soil layer, which is in contact with the surface, the Fourier's equation represents the conduction between the surface T_S and the top soil layer $T_{s,1}$. Conduction between the surface and the middle part of the top layer implies that we calculate the heat transfer only over one half of the layer depth (Eq. A.2). This equation characterizes the soil heat flux as proportional to the current value of thermal conductivity k_s and temperature difference between the surface T_S and the top soil layer $T_{s,1}$. For the purpose of calculating the soil heat flux we used the near surface temperature from the observations and not the model output!

$$Q_g(t+\Delta t) = -\frac{k \cdot (T_S(t+\Delta t) - T_{s,1}(t+\Delta t))}{\frac{\Delta z}{2}} \tag{A.2}$$

For the fourth layer a no flux boundary condition is applied, thus assuming that only the top four soil layers exhibit a noticeable energy variations on the diurnal time scales (Garratt, p.117, 1992) (Eq. A.3).

$$\frac{F_{3\mapsto 4} - 0}{\Delta z} = \frac{T_{s,4}(t+\Delta t) - T_{s,4}(t)}{\Delta t} \tag{A.3}$$

In that way we have obtained a system of four equations for soil energy balance with five unknowns, i.e. the soil temperatures in the layers $T_{s,i}$. Solving the system of these equations allows us to calculate the soil heat flux (Eq. A.2).

A.1.2 Impact of Moisture on the Conductive Properties of the Soil

Soil moisture storage (also the degree of saturation) θ has an indirect effect on the convective properties of the soil which is why the soil heat flux calculation has been coupled with the calculation of the moisture storage in the soil. One can imagine soil as a multitude of differently shaped soil particles in contact with each other. Different shapes of the particles allow that a large portion of the soil is usually occupied by pores which can be filled with water or air. Fraction of the pores that are filled with water determines the moisture storage within the soil. The degree of saturation changes the density ρ_s, thermal diffusivity κ_s and heat capacity of the soil c_s. In this subsection we present the implementation of the of soil density, specific soil heat capacity and conductivity dependencies on the moisture storage.

A.1.2.1 Soil density

Soil density ρ_s is increased by an additional input of moisture. As more water is added to the soil, the air with negligible mass is displaced by water. A new parameter, the soil dry density ρ_d is introduced. Dry density of the soil stands for the density of a soil without any moisture. This enables us to calculate soil density as a function of the degree of saturation (Eq. A.4):

$$\rho_s = \rho_{dry} + \left(\frac{W}{W_{max.}} \cdot \theta_{sat}\right) \cdot \rho_w \tag{A.4}$$

where W represents the height of the water column in the bucket with a maximum capacity of W_{max}. The proportion of the maximum bucket capacity in relation to the soil layer depth defines the moisture saturation value of that layer $\theta_{sat} = W_{max}/dz$.

A.1.2.2 Heat capacity

Soil is usually not chemically homogeneous. It consists of different chemical compounds with their corresponding fractions. Each of these compounds has its own heat capacity. One can assume that these compounds are evenly distributed throughout the soil. Therefore the aggregate soil heat capacity must be calculated as a sum of capacities from individual compounds, multiplied by the mass fraction of each compound x_i:

$$c_s = x_1c_1 + x_2c_2 + ... + x_ic_i;\ where:\ x_1 + x_2 + ... + x_i = 1 \tag{A.5}$$

We can further simplify the formula by assuming that the soil can be described as a sum of mineral compounds c_q, organic compounds c_o and water c_w, with compounds within a particular group having the same heat capacity (De Vries, 1975):

$$c_s = (1 - \theta_{sat})\, q \cdot c_q + (1 - q) \cdot (1 - \theta_{sat}) \cdot c_o + \left(\frac{W}{W_{max}} \cdot \theta_{sat}\right) \cdot c_w \tag{A.6}$$

Fractional parameter q stands for the proportion of mineral compounds in the soil.

A.1.2.3 Thermal conductivity

Numerous soil scientists have been working on the development of semi-empirical engineering methods, which try to capture the dynamics of the soils' conductive properties. "Thermal properties of soils" by Farouki, (1986) provides an extensive overview and evaluation of these methods for a wide variety of soils. For the purposes of calculating thermal conductivity as a function of moisture for the Hablic podzol, the soil type at Hyytiälä, Farouki (1986) recommends the Johansen's method due to its reliability and satisfactory precision. The following equations that constitute the Johansen's method (Eqs. A.7 - A.14) are all adapted from Farouki, (1986). Johansen's method to calculate thermal conductivity at a partial saturation of the soil is based on the concept of the Kersten's number K_e, which is basically an interpolation between the conductivities of the saturated $k_{s,sat}$ and dry state $k_{s,dry}$(Eq. A.7).

$$K_e = \frac{k_s - k_{s,dry}}{k_{s,sat} - k_{s,dry}} \tag{A.7}$$

By knowing the Kersten number K_e we can calculate the conductivity as:

$$k_s = (k_{s,sat} - k_{s,dry}) \cdot K_e + k_{s,dry} \tag{A.8}$$

Based on the experimental data, Johansen has derived the following relationships between theK_e and the degree of saturation $\theta = \frac{W}{W_{max}}$ for a fine soil (Farouki, p.113, 1986):

$$K_e = \log\left(\frac{W}{W_{max}}\right) + 1.0 \tag{A.9}$$

Furthermore, the author has also formulated the semi-empirical equations for determining the dry and saturated state conductivities $k_{s,dry}$ and $k_{s,sat}$ for different types of soils. Here we present only the relations that are applicable to the unfrozen natural soils, which correspond with the properties of the Hablic podzol. First of all, we calculate the thermal conductivity of a dry soil $k_{s,dry}$ with the following empirical relation (Farouki, p.112, 1986):

$$k_{s,dry} = \frac{0.135 \cdot \rho_{dry} + 64.7}{2700 - 0.347 \cdot \rho_{dry}} \tag{A.10}$$

This is followed by a calculation of the effective thermal conductivity of the solids $k_{s,solid}$, which characterizes the thermal properties of the soil particles, i.e soil without pores, depending on the content of minerals (quartz) and organic matter (Eq. A.11).

$$k_{s,solid} = k_q^q \cdot k_o^{1-q} \tag{A.11}$$

Finally, we need to obtain the thermal conductivity of the soil at a saturated state. Johansen proposes an empirical relation, where the conductivity is calculated as a geometric mean of the conductivity of the solids $k_{s,solid}$ and water k_w, with each term exponentiated at its respective volume faction $(1 - \theta_{sat})$:

$$k_{s,sat} = k_{s,solid}^{1-\theta_{sat}} \cdot k_w^{\theta_{sat}} \tag{A.12}$$

With the known information of dry soil density ρ_{dry}, moisture saturation θ_{sat}, the content of quartz q and moisture storage W we can calculate all of the above mentioned parameters and use them to evaluate the thermal conductivity of the soil k_s as a function of soil moisture storage (Eq. A.8).

A.1.3 Soil Heat Flux Results

We compare the modelled and measured soil heat flux $Q_g$at Hyytiälä from 13/07/2010 to 10/08/2010. This is followed by an analysis of a diurnally averaged soil heat flux. Figure A.1a depicts a continuous time-series of the modelled and measured soil heat flux. The time step on the x axis represents a 30 minute interval between two consecutive values of the flux. The positive values of the heat flux show the net heat storage in the soil, while the negative values imply a net heat release from the soil. We can see from the Fig. A.1a that the model captures the diurnal cycles reasonable well, yet on the other hand also clearly overestimates the amplitude of the flux. Moreover, it can also be observed that the measured heat flux rarely drops bellow zero. The observations therefore imply that the soil is a net absorber of the heat, which does not make sense over longer time periods (Garratt, p.118, 1992), when the daily average of the soil heat flux should be $\sim \overline{Q_g} = 0$. For that reason, we intentionally did not try to calibrate the soil heat flux according to the measurements. We also intentionally calibrated the flux in a way that we have obtained a larger amplitude response of the soil. In that way, we tried to partially compensate for

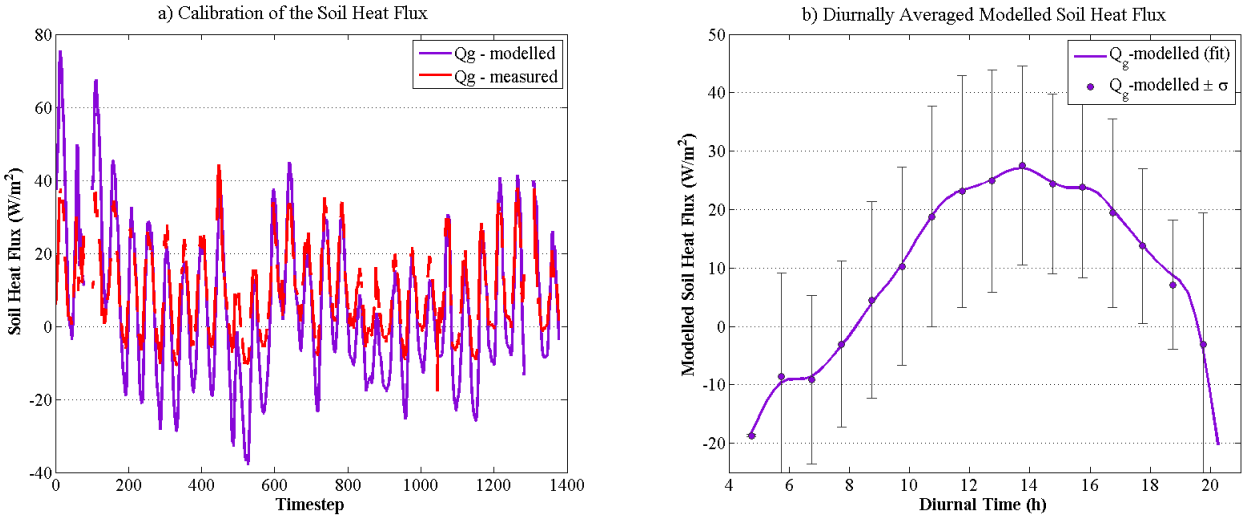

Figure A.1: Soil heat flux $Q_g$model analysis. Fig. A.1a depicts the time-series of the observed and measured soil heat flux. Time step on the x axis represents the 30 minute intervals of the series. Fig. A.1b portrays an averaged diurnal cycle of the modelled soil heat flux. The figure shows that the soil becomes a net absorber of the heat around 7am, which is approximately one hour after a positive increase of the near surface temperature. A similar time delay is observed in the late afternoon when the soil heat flux becomes a net emitter of heat after 7 pm.

the negligence of the canopy heat storage, which is in principle a more important term in the surface energy balance. Figure A.1b depicts a diurnally averaged modelled soil heat flux. By comparing the diurnal variability of the flux with the diurnal variability of the observed near surface temperature (Fig. 4.9a), we can observe a positive time delay of the soil heat flux of approximately one hour, which is a reasonable estimate for the delay of a soil heat response in the forest (Garratt, p.236, 1992).

A.2 Soil Moisture

A.2.1 Groundwater flow

Groundwater flow is based on the Darcy's law, a commonly used approach in soil moisture modeling (Garratt, p.138, 1992) (Eq. A.13). The two variables that determine the magnitude of the groundwater flow are the hydraulic conductivity $K(W)$ and the hydraulic pressure head ψ. Both are specified with empirical functions for various soil types (Clapp and Hornberger, 1978).

$$F_{g,i} = -\rho_w \cdot K(W_i) \cdot \frac{\partial(\psi_i + z)}{\partial z} \tag{A.13}$$

Hydraulic conductivity $K(W)$ is proportional to the hydraulic conductivity value at the saturation $K_{\theta sat}$, multiplied by soil moisture storage θ which is exponentiated with an empirical parameter β (Eq. A.14). Hydraulic pressure head ψ has an analogous functional form (Eq. A.15).

$$K(W_i) = K_{\theta sat} \cdot (\frac{W_i}{W_{max,i}})^{2\beta+3} \tag{A.14}$$

$$\psi_i = \psi_{sat}(\frac{W_i}{W_{max,i}})^{-\beta} \tag{A.15}$$

A.2.2 Water Availability in the Bare Soil

Total evapotranspiration was partitioned into the bare soil evaporation and evapotranspiration of the vegetation (Eq. 2.41). The fractions reflect the surface type proportions at the observation site that is covered by vegetation and bare soil, a method that is applied in the ECMWF model (IFS Model cycle - Cy40r1, 2013). The fraction estimates, which were based on the satellite imagery of the measuring site, are as follows; 30 % of the total evapotranspiration at the Hyytiälä site is attributed to the bare soil evaporation λE_0. The residual 70% is attributed to the evapotranspiration of the vegetation which is described in Eq. 2.40. The parameter that relates bare soil evaporation at the surface with soil moisture storage is water availability f_w (Kleidon et al., 2014). Water availability, with its value ranging from 0 to 1, depends on the specific humidity gradient between the surface and top of EBL $q(T_S) - q_{sat}(T_{TBL})$. Specific humidity at the surface is calculated as a saturated specific humidity, which is a function of surface temperature multiplied by the relative humidity r_h at the surface of the bare soil (Eq. A.16). The expression was derived by equating the model parameterization of the bare soil latent heat flux (Eq. 2.29) with the "Monin-Obukhov parameterization" (Eq. 2.27).

$$f_w = \frac{r_h \cdot q_{sat}(T_S) - q_{sat}(T_{TBL})}{q_{sat}(T_S) - q_{sat}(T_{TBL})} \tag{A.16}$$

Relative humidity at the surface r_h is calculated from an empirical function by Clapp and Hornberger and relates the relative humidity to the soil moisture storage in the top layer of the soil $\theta = \frac{W}{W_{max}}$ (Garratt, p.138, 1994).

$$r_h = \exp(\frac{-g \cdot |\psi_{sat}| \cdot (\frac{W}{W_{max}})^{-\beta}}{R_v \cdot T_S}) \tag{A.17}$$

Finally, the saturated specific humidity is calculated as:

$$q_{sat}(T) = \frac{0.622 \cdot e_{sat}(T)}{p - 0.378 \cdot e_{sat}(T)} \tag{A.18}$$

A.2.3 Soil Moisture Storage Results

Analysis of the soil moisture in the top soil horizon (top 7 cm of the soil) which is detrimental for the bare soil evaporation was conducted by comparing the modelled water column height with the observed water column height (Fig. A.2). Maximum field capacity of the top soil was determined at 17.5 cm. For the purpose of qualitative analysis a water limited regime was determined, which was defined as the water level below which the water availability parameter f_w drops under 0.8. The water limited regime boundary was calculated from the equations A.16 and A.17 and equals $\sim$ 4 cm. We can see from Fig. A.2. that the modelled moisture storage closely matches the observations from 13th of July to 29th of July. In the period between 29th of July and 4th of August the model overestimates the drying of the top soil. On contrary to the observations, which demonstrate a halt in the drying, the model projects an intensification of the drying. Further on the precipitation event on the 4th of August increases the moisture storage of both time series. Finally, the precipitation event on the 8th of August noticeably increases the modelled moisture storage, which returns back to the observed values. Besides the aforementioned overestimation in the drying of the soil this latter disproportional increase in the moisture storage cleary indicates that the model is oversensitive under certain conditions. A detailed analysis of this problem was not performed, since the soil module was not in the central focus of the research. Still, a possible explanation for an overestimated drying of the top soil comes from the fact that the modelled moisture storage never drops beyond the water limited regime. This means that the evapotranspiration was not significantly inhibited by a drop in soil moisture storage, since it never dropped below the water limited regime boundary of $f_w = 0.8$. Such a weak response of the water availability to the moisture storage in the model suggests that the water limited regime in the system probably occurs earlier, at higher storage values.

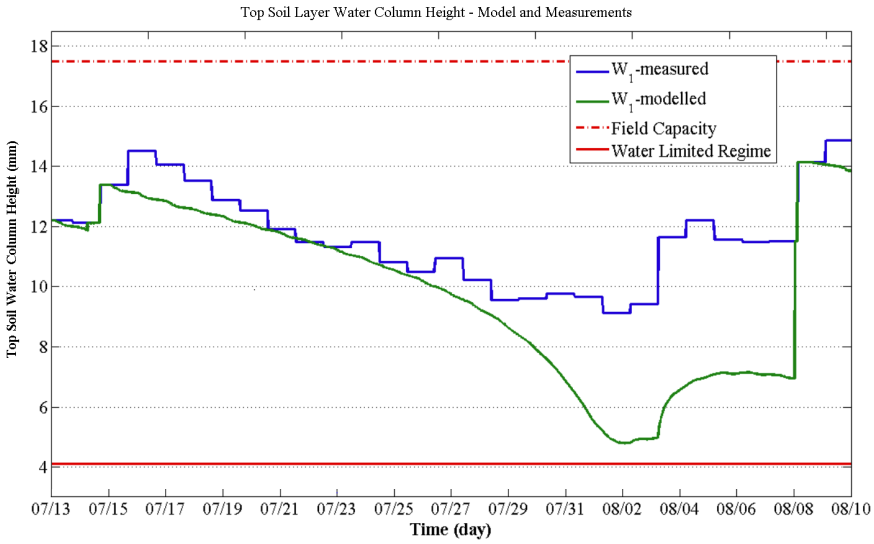

Figure A.2: Soil moisture storage analysis. The figure portrays a comparison of the observed and modelled heights of the water column in the top soil layer. The figure also shows a maximum field capacity of 17.5 cm and the upper boundary of the water limited regime at 4 cm. Evaporation of the bare soil, which is represented by the water availability parameter f_w, drops significantly as the soil is being dried below the water limited regime boundary.

A.3 Vegetation

In this section of the appendix we present a more detailed implementation of the stomatal regulation of evapotranspiration. This regulation is represented with a single stomatal resistance parameter that represents the functioning of the entire ecosystem. Implementation of the stomatal resistance is adapted from the Jarvis model implementation in the ECMWF operational model (IFS Model cycle - Cy40r1, 2013). Stomatal resistance in the model is proportional to the minimum stomatal conductance r_{min} that depends on the vegetation type, over the leaf area index LAI. The selected vegetation type for Hyytiälä was the evergreen needleaf forest with $r_{min} = 250$ and $LAI = 6$ (IFS Model cycle - Cy40r1, 2013). In addition, the stomatal resistance is temporally varying according to the empirical functions of the solar radiation at the surface $(1-\varphi)R_s$, average root water $\overline{\theta}$ and the atmospheric humidity deficit D_a:

$$r_c = \frac{r_{min}}{LAI} \cdot f_1((1-\varphi)R_s) \cdot f_2(\overline{\theta}) \cdot f_3(D_a) \tag{A.19}$$

The inverse of the solar radiation effect on the stomatal resistance f_1 is defined as:

$$f_1(R_s)^{-1} = min\left[1, \frac{b \cdot (1-\varphi)R_s + c}{a \cdot (b \cdot (1-\varphi)R_s + 1)}\right] \tag{A.20}$$

where a, b and c are empirical parameters, dependent on the vegetation type. f_1 is increasing with solar radiation, thus implying a higher stomatal resistance of the vegetation that is exposed to solar radiation. The inverse of the soil moisture saturation function f_2, which characterizes the stomatal resistance dependence on the average root water storage $\overline{\theta}$, is a piecewise function of three different regimes (Eq. A.21). The first, permanent wilting point regime corresponds with the state of very scarce moisture in the soil θ_{pwp}. In that state, the plants completely close the stomata, therefore $r_c \to \infty$ and plants do not allow any transpiration. The second regime refers to the state of a saturated soil θ_{sat}. Lastly, the inverse moisture saturation function in the intermediate regime is just an interpolation between the other "extremal" regimes.

$$f_2(\bar{\theta})^{-1} = \begin{cases} 0 & ; \bar{\theta} < \theta_{pwp} \\ \frac{\bar{\theta}-\theta_{pwp}}{\theta_{sat}-\theta_{pwp}}; & \theta_{pwp} \leq \theta \leq \theta_{sat} \\ 1 & ; \bar{\theta} > \theta_{sat} \end{cases} \tag{A.21}$$

The average root water $\overline{\theta}$ is a sum of the soil moisture storage multiplied by the root fraction in each of the three soil layers:

$$\bar{\theta} = \sum root_i \cdot \theta_i \tag{A.22}$$

Finally, the stomatal resistance is also dependent on atmospheric humidity deficit, a measure of moisture in the air at the canopy $D_a = e_{sat}(1 - r_h)$. The dependence is exponential (Eq. A.23), meaning a higher stomatal resistance at greater humidity deficit.

In that way the plants restrict water loss under dry ambient conditions (Farquhar et al., 1980). The exponential parameter g_d depends on the vegetation type and equals $0.03\,hPa^{-1}$ in our model.

$$f_3(D_a)^{-1} = \exp(-g_d \cdot D_a) \tag{A.23}$$

Appendix B

Future Recommendations

Some recommendations for framework improvements were already presented in the implications and limitations sections. Amongst other recommendations, we have proposed an inclusion of the horizontal heat and moisture advection, an elimination of the greenhouse radiation in the EBL, an introduction of the atmospheric longwave release into space and an explicit modelling of the surface friction dissipation. These are all limitations that should have been resolved in order to apply the framework in the more complex models. We propose two structural improvements of the framework for future work. Firstly, we build on the critique of the current water cycle representation in the model, thus presenting a design of an explicit water cycle implementation in the model. This is followed by an illustration of an improved vertical resolution of the model.

B.1 The EBL with Water Cycle

We begin the water cycle extension by introducing an additional moisture reservoir in the atmosphere Θ_{EBL}, which represents the moisture storage in the atmosphere. The EBL moisture storage term is a function of moisture input from the surface latent heat flux and moisture output by precipitation $\lambda Prec$, which is assumed to take place entirely in the EBL (Koenings et al., 2012) (Eq. B.1). Horizontal moisture transport in not included in this partial extension of the water cycle.

$$\Theta_{EBL} = \lambda E - \lambda Prec \tag{B.1}$$

Implementation of the EBL moisture storage also affects the energy balance equation of the sensible heat storage. The latent heat is released upon condensation in the EBL, thus warming up the EBL (Eq. B.2).

$$Ha = H + D - P + \lambda Prec - J_{out} \tag{B.2}$$

Other terms in the EBL heat storage equation remain the same as in our framework (Eq. 3.2), except for the greenhouse radiation in the EBL, which is now removed from the

expression. The proposed water cycle also implies a change in the nature of the outgoing heat flux J_{out}. While the outgoing heat flux in the current framework represents both sensible and latent heat transport in the TOA reservoir, the J_{out} term in the proposed extension transfers only the remaining sensible heat flux from the atmospheric heat engine. This is undoubtedly a physically more consistent representation of the vertical heat transport in the system. Finally, we should note that this extension does not provide a complete representation of the water cycle. First of all, by excluding the horizontal moisture transport we only capture the local water cycle, which can be an adequate concept only for the some systems. The proposal also lacks implementation of the precipitation trigger mechanism. In other words, while we have added the precipitation in the system, we still miss the physical processes that cause precipitation at first place. A simple first-order representation of the precipitation mechanism could be implemented, by prescribing the total moisture carrying capacity of the EBL Θ_{max}, which would depend on the boundary layer temperature $< \theta_{BL} >$. When the moisture in the system exceeds the maximum capacity, the wet condensation is triggered. Such a simple approach naturally disregards a generally complex nature of the physics of precipitation, which also depends for example on the amount of cloud condensation nuclei and the dynamic stability of the atmosphere (Holton, p.302, 1973). The water cycle extension scheme is presented in the right panel of Fig. B.1.

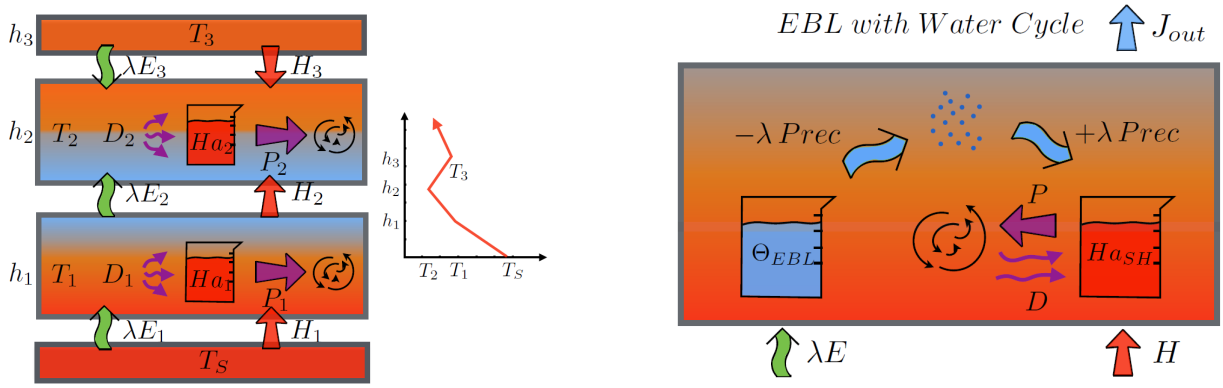

Figure B.1: Recommended improvements in the framework. The left panel illustrates the MPP framework with multiple vertically coupled heat storage reservoirs. Vertical temperature profile in the right hand side of the left panel indicates a possibility to apply the MPP framework to the temperature inversion conditions. The heat storage of an individual reservoir is a function of the dissipation and power generation within the reservoir and the net difference between the heat fluxes at the top and the bottom of the reservoir. e.g.: $Ha_1 = D_1 - P_1 + \lambda E_1 + H_1 - (-H_2 - \lambda E_2)$). Thickness of the reservoirs determines the vertical resolution of the framework. The right panel demonstrates the EBL water cycle extension. The left side of the illustration depicts the storage and release of moisture in the EBL Θ_{EBL}, while the right side portrays the heat storage and release in the EBL.

B.2 The Multiple Heat Storage Extension

A major deficiency of our model, which was observed throughout the results analysis is a coarse vertical resolution of the framework. Such a resolution implicitly leads to the uniform modelling of the vertical turbulent heat transport. Moreover, it also limits the framework's applicability to the convective boundary layer conditions. We could improve the precision and general applicability of the model by partitioning a single EBL reservoir into several vertically coupled heat storage reservoirs (left panel of the Fig. B.1), each at its own respective temperature that is determined by the net exchange of the turbulent fluxes in the system and the balance between dissipation and power generation (Eq. N.5). It is assumed that each reservoir exchanges heat accordingly with the MPP limit. This extension requires different parameterizations of the turbulent heat fluxes, especially for the latent heat flux because we cannot assume the air to be saturated at the top of each reservoir, as we have done in the single EBL (Eq. 2.28). The partitioning of the EBL into several reservoirs requires a use of parameterizations where the sensible heat flux is proportional to the temperature difference between the two reservoirs, and where the latent heat flux is proportional to the difference in the specific humidity q of the reservoirs (Eqs. B.3 and B.4)

$$H_1 = \rho c_p w_1 (T_1 - T_2) \tag{B.3}$$

$$\lambda E_1 = \lambda \rho w_1 (q_1 - q_2) \tag{B.4}$$

The reservoir heat storage Ha_1 in the proposed framework is then calculated as a difference between the turbulent heat fluxes at the bottom and the turbulent heat fluxes at the top of the respective reservoir, in addition to the difference between the dissipation and power generation within the reservoir.

$$Ha_1 = D_1 - P_1 + \lambda E_1 + H_1 - (-H_2 - \lambda E_2)) \tag{B.5}$$

Besides the turbulent fluxes, the partitioning also leads to an improved resolution of the convective motions. As a consequence of the partitioning, a single atmospheric heat engine is partitioned into a multitude of vertically coupled heat engines with different vertical exchange velocities for each reservoir w. The suggested extensions affect the calculation of the entropy production and consequently also the derivation of the respective optimum fluxes at the MPP limit. The proposed design would therefore require solving of a far more extensive and presumably also more complex system of equations than in the implemented framework. Concrete derivation steps would therefore require an extensive theoretical research and are for that reason alone beyond the scope of this thesis study.

Appendix C

List of Variables and Parameters

Symbol	Variable	Units	(Mean) values in the model
α	Surface albedo	/	0.93 (Betts and Ball, 1997)
Ha_{SH}	Sensible heat storage	$\frac{W}{m^2}$	/
Ha_{LH}	Latent heat storage	$\frac{W}{m^2}$	/
Q_{SH}	Internal energy	$\frac{J}{m^2}$	/
Q_{LH}	Latent heat	$\frac{J}{m^2}$	/
g	Gravitation	$\frac{m}{s^2}$	9.8
e	Water vapor pressure	Pa	/
$L_{\downarrow}$	Incoming longwave radiation	$\frac{W}{m^2}$	375.6
Λ	Climate sensitivity	$\frac{K}{W\,m^{-2}}$	0.21

Table C.1: Overview of variables and parameters introduced in the methodology chapter.

Symbol	Variable	Units	(Mean) values in the model
R_s	Total absorbed solar radiation	$\frac{W}{m^2}$	269.6
φR_s	R_s absorbed in TOA	/	0.26 (Ramanathan and Vogelmann, 1997)
$R_{L,surf}$	Surface outgoing longwave	$\frac{W}{m^2}$	510.3
$R_{L,atm}$	TOA outgoing longwave	$\frac{W}{m^2}$	439.2
τ	Optical depth	/	2.036
H	Surface sensible heat flux	$\frac{W}{m^2}$	77.1
λE	Surface latent heat flux	$\frac{W}{m^2}$	110.7
Q_g	Soil heat flux	$\frac{W}{m^2}$	10.7
J_{out}	Outgoing convective heat flux	$\frac{W}{m^2}$	??
D	Surface friction dissipation	$\frac{W}{m^2}$	$D = P$
P	Power generation	$\frac{W}{m^2}$	39.1
H_a	EBL heat storage	$\frac{W}{m^2}$	90.0
S_b	EBL entropy	$\frac{W}{K}$	/
T_S	Surface temperature	K	309.3
T_A	TOA temperature	K	265.3
c_p	Specific heat at constant pressure	$\frac{W}{kg \cdot K}$	1004 (Holton, 1973)
R_{dry}	Gas constant for dry air	$\frac{J}{kgK}$	287 (Holton, 1973)
p	Pressure	$\frac{N}{m^2}$	~ 1000
ρ	Air density	$\frac{kg}{m^3}$	~ 1.2
ref	Arbitrary reference state		/
$< \theta_b >$	EBL bulk potential temperature	K	/
h	EBL height	m	~ 4600
J	$H + \lambda E$	$\frac{W}{m^2}$	187.8
σ	Stephan-Boltzman constant	$\frac{W}{m^2 K^4}$	$5.67 \cdot 10^{-8}$
$R_{L,0}$	Radiation constant	$\frac{W}{m^2}$	71.1
R_{net}	Net Radiation at the surface	$\frac{W}{m^2}$	71.1
kr	Linearized radiative exchange	$\frac{W}{m^2 K}$	5.66

Table C.2: Overview of variables and parameters introduced in the modelling framework chapter.

Symbol	Variable	Units	(Mean) values in the model
r_{aV} & r_{aH}	Aerodynamic resistances	/	/
w	Vertical exchange velocity	$\frac{m}{s}$	$3.0 \cdot 10^{-3}$
T_{TBL}	Top of the EBL temperature	K	289.5
λ	Specific latent heat	$\frac{J}{kg}$	$2.5 \cdot 10^{5}$
f_w	Water availability	/	0.98
$q(T)$	Specific humidity	$\frac{g}{kg}$	/
s	Saturation vapor pressure curve	$\frac{Pa}{K}$	195.8
γ	Psychrometric constant	$\frac{Pa}{K}$	65 (Kleidon and Renner, 2013)

Table C.3: Overview of variables and parameters related to the turbulent heat fluxes parameterizations.

Symbol	Variable	Units	(Mean) values in the model
θ	Degree of saturation	/	$0.1 - 0.45$
Th	Throughfall	$\frac{mm}{s}$	/
W	Moisture content	mm	~ 11
W_{max}	Maximum moisture storage	mm	/
F_g	Groundwater flow	$\frac{mm}{s}$	$-2.6 \cdot 10^{-6}$
ρ_w	Water density	$\frac{kg}{m^3}$	1000
ψ	Hydraulic pressure head	m	/
$K(\theta)$	Hydraulic conductivity	$\frac{m}{s}$	$34.6 \cdot 10^{-6}$ (Clapp and Hornberger, 1978)
$q_{sat}(T)$	Saturated specific humidity	$\frac{g}{kg}$	2.2
r_h	Relative humidity	/	$0 - 1$
R_v	Gas constant for vapor	$\frac{J}{kg \cdot K}$	462 (Holton, 1973)
$e_{sat}(T)$	Saturation vapor pressure	Pa	$611\,at\,0\,°C$ (Kleidon and Renner, 2013)
$root$	Root fraction	/	$0 - 1$
β	/	/	4.9 (Clapp and Hornberger, 1978)

Table C.4: Overview of variables and parameters introduced in the soil part of the appendix.

Symbol	Variable	Value/Units	(Mean) values in the model
ρ_{dry}	Soil dry density	$\frac{kg}{m^3}$	1600 (De Vries, 1975)
θ_{sat}	Moisture saturation value	$\frac{m^3}{m^3}$	/
W_{max}	Maximum moisture storage	mm	/
c_o	Heat capacity of organic matter	$\frac{J}{kg \cdot K}$	1920 (De Vries, 1975)
c_q	Heat capacity of minerals	$\frac{J}{kg \cdot K}$	840 (De Vries, 1975)
c_w	Water heat capacity	$\frac{J}{kg \cdot K}$	4182 (De Vries, 1975)
q	Mineral fraction	/	5% (Greve et al., 1998)
K_e	Kersten's number	/	/
$k_{s,sat}$	Conductivity of saturated soil	$\frac{W}{m \cdot K}$	/
$k_{s,dry}$	Conductivity of dry soil	$\frac{W}{m \cdot K}$	/
$k_{s,solid}$	Effective conductivity of solids	$\frac{W}{m \cdot K}$	/
k_w	Conductivity of water	$\frac{W}{m \cdot K}$	/
k_o	Conductivity of organic materials	2.0 $\frac{W}{m \cdot K}$	2.0 (Farouki, 1986)
k_q	Conductivity of mineral materials	7.7 $\frac{W}{m \cdot K}$	7.7 (Farouki, 1986)
r_{min}	Minimum stomatal resistance	$\frac{s}{m}$	250
D_a	Humidity deficit	$[Pa]$	/
a	/	/	0.81
b	/	$\frac{m^2}{W}$	0.004
c	/	/	0.05
g_d	/	hPa^{-1}	0.03

Table C.5: Overview of variables and parameters introduced in appendix A.

Symbol	Variable	Units	(Mean) values in the model
r_c	Stomatal resistance	$\frac{s}{m}$	471
E_v	Dry canopy evapotranspiration	$\frac{mm}{s}$	77.5
E_0	Bare soil evaporation	$\frac{mm}{s}$	33.2
m	Maximum canopy water storage	mm	12
LAI	Leaf area index	/	6
$Prec$	Precipitation intensity	$\frac{mm}{s}$	$3.1 \cdot 10^{-5}$
C_{veg}	Vegetation cover	/	0.7
θ_{cap}	Field capacity	$\frac{m^3}{m^3}$	0.4
D_a	Humidity deficit	Pa	/
θ_{pwp}	Permanent wilting point	$\frac{m^3}{m^3}$	0.12

Table C.6: Overview of variables and parameters introduced in the vegetation part of the appendix.

Symbol	Variable	Units	(Mean) values in the model
w_*	Convective scale velocity	$\frac{m}{s}$	0.52
F_{drag}	Aerodynamic friction force	N	/
C_d	Drag coefficient	/	/
Θ_{EBL}	EBL moisture storage	$\frac{W}{m^2}$	/

Table C.7: Overview of variables and parameters introduced in the appendix B and the results and discussion chapters.

References

[1] Andrews, T., Forster, P. M., & Gregory, J. M. (2009). A surface energy perspective on climate change. *Journal of Climate,* 22(10), 2557–2570. http://dx.doi.org/10.1175/2008JCLI2759.1

[2] Betts, A. K., & Ball, J. H. (1997). Albedo over the boreal forest. *Journal of Geophysical Research*, 102(D24), 28901–28909. http://dx.doi.org/10.1029/96JD03876

[3] Betts, A. K., & Ridgway, W. (1989). Climatic equilibrium of the atmospheric convective boundary layer over a tropical ocean. *Journal of the Atmospheric Sciences*, 46(17), 2621–2641.

[4] Boer, G. J. (1993). Climate change and the regulation of the surface moisture and energy budgets. *Climate Dynamics*, 8(5), 225–239. http://dx.doi.org/10.1007/BF00198617

[5] Clapp, R. B., & Hornberger, G. M. (1978). Empirical equations for some soil hydraulic properties. *Water Resources Research*, 14(4), 601–604. http://dx.doi.org/10.1029/WR014i004p00601

[6] Collins, M., R., Knutti, J., Arblaster, J.-L., Dufresne, T. Fichefet, P. Friedlingstein, X. Gao, W.J. Gutowski, T. Johns, G., & Krinner, M. Shongwe, C. Tebaldi, A. J. W. and M. W. (2013). 2013: Long-term climate change: projections, commitments and irreversibility. In T. F. Stocker, D. Qin, G.-K. Plattner, M. Tignor, S. K. Allen, J. Boschung, ... P. M. Midgley (Eds.), *Climate Change 2013: The Physical Science Basis. Contribution of Working Group I to the Fifth Assessment Report of the Intergovernmental Panel on Climate Change* (pp. 1031–1106). United Kingdom and New York, NY, USA.: Cambridge University Press.

[7] De Vries, D. A. (1975). Heat and mass transfer in the biosphere. In *Heat transfer in soils* (pp. 5–28). Scripta.

[8] ECMWF. (2013). IFS Documentation - Cy40r1. Operational implementation 22 November 2013. Part IV: Physical processes. Retrieved December 1, 2014, from http://www.ecmwf.int/sites/default/files/IFS_CY40R1_Part4.pdf

[9] European Supersites for Atmospheric Aerosol Research. (n.d.). Description of the SMEAR II station. Retrieved November 29, 2014, from http://www.eusaar.net/upload/SMEAR2.pdf

[10] Farouki, O. T. (1986). *Thermal properties of soils. Volume 11 of Series on Rock and Soil Mechanics Series.* Trans Tech Publications, Limited.

[11] Farquhar, G. D., von Caemmerer, S., & Berry, J. A. (1980). A biochemical model of photosynthetic CO2 assimilation in leaves of C3 species. *Planta*, 149(1), 78–90. http://dx.doi.org/10.1007/BF00386231

[12] Garratt, J. R. (1977). Review of drag coefficients over oceans and continents. *Monthly Weather Review*, 105(7), 915–929. http://dx.doi.org/10.1175/1520-0493(1977)105<0915:RODCOO>2.0.CO;2

[13] Garratt, J. R. (1994). *The atmospheric boundary layer*. Cambridge University Press.

[14] Ghuman, B. S., & Jalota, S. K. (2006). Heat capacity of soil. In R. Lal (Ed.), *Encyclopedia of soil science* (Vol. 2) (pp. 811–813). CRC Press.

[15] Goody, R. (2007). Maximum entropy production in climate theory. *Journal of the Atmospheric Sciences*, 64(7), 2735–2739. http://dx.doi.org/10.1175/JAS3967.1

[16] Grassl, H. (1981). The climate at maximum entropy production by meridional atmospheric and oceanic heat fluxes. *Quarterly Journal of the Royal Meteorological Society*, 5(1981), 153–166. http://doi.org/10.1002/qj.49710745110

[17] Greve, M. H., Helweg, A., Yli-Halla, M., Eklo, O. M., Nyborg, A. A., Solbakken, E., ... Stenström, J. (1998). *Nordic reference soils*. (E. Tiberg, Ed.). Nordic Council of Ministers.

[18] Grimmond, C. S. B., & Oke, T. R. (1995). Comparison of heat fluxes from summertime observations in the suburbs of four North American cities. *Journal of Applied Meteorology*, 34(4), 873–889. http://dx.doi.org/10.1175/1520-0450(1995)034<0873:COHFFS>2.0.CO;2

[19] Gutowski, W. J., Gutzler, D. S., & Wang, W. C. (1991). Surface energy balances of three general circulation models: Implications for simulating regional climate change. *Journal of Climate*, 4(2), 121–134. http://dx.doi.org/10.1175/1520-0442(1991)004<0121:SEBOTG>2.0.CO;2

[20] Hauf, T., & Höller, H. (1987). Entropy and potential temperature. *Journal of the Atmospheric Sciences*, 44(20), 2887–2901. http://dx.doi.org/10.1175/1520-0469(1987)044<2887:EAPT>2.0.CO;2

[21] Held, I. M., & Soden, B. J. (2000). Water vapor feedback and global warming. *Annual Review of Energy and the Environment*, 25(1), 441–475. http://dx.doi.org/10.1146/annurev.energy.25.1.441

[22] Held, I. M., & Soden, B. J. (2006). Robust responses of the hydrological cycle to global warming. *Journal of Climate*, 19(21), 5686–5699. http://dx.doi.org/10.1175/JCLI3990.1

[23] Henderson-Sellers, A., & Wilson, M. F. (1983). Surface albedo data for climatic modeling. *Reviews of Geophysics*, 21(8), 1743–1778. http://dx.doi.org/10.1029/RG021i008p01743

[24] Holton, J. R. (1973). An Introduction to Dynamic Meteorology. *American Journal of Physics*. http://dx.doi.org/10.1119/1.1987371

[25] Ilvesniemi, H., Pumpanen, J., Duursma, R., Hari, P., Keronen, P., Kolari, P., ... Vesala, T. (2010). Water balance of a boreal Scots pine forest. *Boreal Environment Research*, 15(4), 375–396.

[26] Inamdar, A. K., & Ramanathan, V. (1998). Tropical and global scale interactions among water vapor, atmospheric greenhouse effect, and surface temperature. *Journal of Geophysical Research*, 103(D24), 32177–32194. http://dx.doi.org/10.1029/1998jd900007

[27] IPCC. (2001). Climate change 2001: The scientific basis. (J. T. Houghton, D. J. Y. Ding, M. Griggs, P. J. Noguer, X. van der Linden, K. Dai, ... C. A. Johnson, Eds.) *Contribution of Working Group I to the Third Assessment Report of the Intergovernmental Panel on Climate Change* (Vol. 881). Cambridge: Cambridge University Press.

[28] Jarvis, P. G. (1976). The interpretation of the variations in leaf water potential and stomatal conductance found in canopies in the field. *Philosophical Transactions of the Royal Society B: Biological Sciences*, 273(927), 593–610. http://dx.doi.org/10.1098/rstb.1976.0035

[29] Kleidon, A. (2003). The atmospheric circulation and states of maximum entropy production. *Geophysical Research Letters*, 30(23), 1–4. http://dx.doi.org/10.1029/2003GL018363

[30] Kleidon, A. (2010). Life, hierarchy, and the thermodynamic machinery of planet Earth. *Physics of Life Reviews*, 7(4), 424–460. http://dx.doi.org/10.1016/j.plrev.2010.10.002

[31] Kleidon, A. (2011). How does the earth system generate and maintain thermodynamic disequilibrium and what does it imply for the future of the planet?

Philosophical Transactions of the Royal Society of London, 370(1962), 1012–1040. http://dx.doi.org/10.1098/rsta.2011.0316

[32] Kleidon, A. (2015). *MPP limit in a radiative heat engine. Unpublished manuscript.* Jena.

[33] Kleidon, A., Fraedrich, K., Kirk, E., & Lunkeit, F. (2006). Maximum entropy production and the strength of boundary layer exchange in an atmospheric general circulation model. *Geophysical Research Letters*, 33(6), 2–5. http://dx.doi.org/10.1029/2005GL025373

[34] Kleidon, A., & Renner, M. (2013). Thermodynamic limits of hydrologic cycling within the Earth system: concepts, estimates and implications. *Hydrology and Earth System Sciences*, 17(7), 2873–2892. http://dx.doi.org/10.5194/hess-17-2873-2013

[35] Kleidon, A., & Renner, M. (2014). *Limits of land-atmosphere exchange. Unpublished manuscript.* Jena.

[36] Kleidon, A., Renner, M., & Porada, P. (2014). Estimates of the climatological land surface energy and water balance derived from maximum convective power. *Hydrology and Earth System Sciences*, 18(6), 2201–2218. http://dx.doi.org/10.5194/hess-18-2201-2014

[37] Konings, A. G., Feng, X., Molini, A., Manzoni, S., Vico, G., & Porporato, A. (2012). Thermodynamics of an idealized hydrologic cycle. *Water Resources Research*, 48(5). http://dx.doi.org/10.1029/2011WR011264

[38] Lacis, A. A., & Hansen, J. (1974). A parameterization for the absorption of solar radiation in the Earth's atmosphere. *Journal of the Atmospheric Sciences*, 31(1), 118–133. http://dx.doi.org/10.1175/1520-0469(1974)031<0118:APFTAO>2.0.CO;2

[39] Lorenz, R. D., Lunine, J. I., Withers, P. G., & McKay, C. P. (2001). Titan, Mars and Earth: Entropy production by latitudinal heat transport. *Geophysical Research Letters*, 28(3), 415–418. http://dx.doi.org/10.1029/2000GL012336

[40] Lovelock, J. E. (1975). Thermodynamics and the recognition of alien biospheres. *Proceedings of the Royal Society of London. Series B, Biological Sciences*, 189(1095), 167–181.

[41] Manabe, S. (1969). Climate and the ocean circulation 1. The atmospheric circulation and the hydrology of the Earth's surface. *Monthly Weather Review*, 97(11), 739–774. http://dx.doi.org/10.1175/1520-0493(1969)097<0739:CATOC>2.3.CO;2

[42] Moss, R. H., Edmonds, J. A., Hibbard, K. A., Manning, M. R., Rose, S. K., van Vuuren, D. P., ... Wilbanks, T. J. (2010). The next generation of scenarios for climate change research and assessment. *Nature*, 463(7282), 747–756. http://dx.doi.org/10.1038/nature08823

[43] Myhre, G., Highwood, E. J., Shine, K. P., & Stordal, F. (1998). New estimates of radiative forcing due to well mixed greenhouse gases. *Geophysical Research Letters*, 25(14), 2715–2718. http://dx.doi.org/10.1029/98GL01908

[44] Myhre, G., Shindell, D., Bréon, F.-M., Collins, W., Fuglestvedt, J., Huang, J., ... Zhan, H. (2013). 2013: Anthropogenic and natural radiative forcing. In T. F. Stocker, D. Qin, G.-K. Plattner, M. Tignor, S. K. Allen, J. Boschung, ... P. M. Midgley (Eds.), *Climate Change 2013: The Physical Science Basis. Contribution of Working Group I to the Fifth Assessment Report of the Intergovernmental Panel on Climate Change* (pp. 659–740). United Kingdom and New York, NY, USA.: Cambridge University Press.

[45] Nakajima, S., Hayashi, Y.-Y., & Abe, Y. (1992). A study on the "runaway greenhouse effect" with a one-dimensional radiative–convective equilibrium model. *Journal of the Atmospheric Sciences*, 49(23), 2256–2266. http://dx.doi.org/10.1175/1520-0469(1992)049<2256:ASOTGE>2.0.CO;2

[46] NCDC. (2015). Local climatological data for Barstow, California. Retrieved March 6, 2015, from http://www.ncdc.noaa.gov/cdo-web/datasets

[47] Ouwersloot, H. G., Vilà-Guerau De Arellano, J., Nàlscher, a. C., Krol, M. C., Ganzeveld, L. N., Breitenberger, C., ... Lelieveld, J. (2012). Characterization of a boreal convective boundary layer and its impact on atmospheric chemistry during HUMPPA-COPEC-2010. *Atmospheric Chemistry and Physics*, 12(19), 9335–9353. http://dx.doi.org/10.5194/acp-12-9335-2012

[48] Ozawa, H., Ohmura, A., Lorenz, R. D., & Pujol, T. (2003). The second law of thermodynamics and the global climate system: A review of the maximum entropy production principle. *Reviews of Geophysics*, 41(4). http://dx.doi.org/10.1029/2002RG000113

[49] Paltridge, G. W. (1979). Climate and thermodynamic systems of maximum dissipation. *Nature*, 279(5714), 630–631. http://dx.doi.org/10.1038/279630a0

[50] Ramanathan, V., & Vogelmann, A. M. (1997). Greenhouse effect, atmospheric solar absorption and the Earth's radiation budget: From the Arrhenius-Langley era to the 1990s. *Ambio*, 26(1), 38–46.

[51] Schmiedl, T., & Seifert, U. (2007). Efficiency at maximum power: An analytically solvable model for stochastic heat engines. *A Letters Journal Exploring the Frountiers of Physics*, 81(2), 1–6. http://dx.doi.org/10.1209/0295-5075/81/20003

[52] Staley, D. O., & Jurica, G. M. (1972). Effective atmospheric emissivity under clear skies. *Journal of Applied Meteorology*, 11(2), 349–356. http://dx.doi.org/10.1175/1520-0450(1972)011<0349:EAEUCS>2.0.CO;2

[53] Stull, R. B. (1988). *An introduction to boundary layer meteorology* (Vol. 13). Springer Netherland. http://doi.org/10.1007/978-94-009-3027-8

[54] Suni, T., Rinne, J., Reissell, A., Altimir, N., Keronen, P., Rannik, U., ... Vesala, T. (2003). Long-term measurements of surface fluxes above a Scots pine forest in Hyytiala, southern Finland, 1996-2001. *Boreal Environment Research*, 8(4), 287–301.

[55] Trenberth, K. E., Fasullo, J. T., & Kiehl, J. (2009). Earth's global energy budget. *Bulletin of the American Meteorological Society*, 90(3), 311–323. http://dx.doi.org/10.1175/2008BAMS2634.1